STUDIES OF COLLECTIVE SPONTANEOUS EMISSION

STEFAN MOSSOR RATHMANN

M.Sc. Dissertation

University of Copenhagen

14. October 2016

Supervisor: Jan W. Thomsen

ABSTRACT

The frequency stability of current state-of-the-art atomic clock lasers [3] are limited by thermal fluctuations in the mirrors of the passive reference cavities used for frequency stabilization [4]. This work describes the possibility of reaching stability levels below the limits set by the thermal fluctuations, by exploiting collective emission of a cold ensemble of Strontium atoms coupled to a cavity. Thermal fluctuations in the passive reference cavity mirrors can in principle be ignored when utilizing collective emission as an alternative method to achieve laser stabilization.

This work reports an observation of collective emission in a proof-of-principle atom-cavity system. By initially phase locking the dipoles of the cooled atomic ensemble, cavity enhanced collective emission is achieved in a linewidth regime where thermal fluctuations of the cavity mirrors do not dominate the combined atom-cavity linewidth. The achieved atom-cavity linewidth is instead dominated by the linewidth of the collective emission. By utilizing the $^1S_0 \leftrightarrow {}^3P_1$ transition of ^{88}Sr with a linewidth of 7.5 kHz, a theoretical lower limit of an achievable collective emission linewidth is $\sim$ mHz.

This work describes the cooling of the atoms into the mK range, where velocity induced decoherence is diminished. Decoherence was furthermore diminished by implementing a mechanical light shutter, cancelling remnant cooling light which caused decoherence by interacting with the atomic ensemble. An optical cavity placed around the atoms, was implemented to increase the effective length of the atom-light interaction. An injection-locked pulse-laser initially inverted the population of the atomic ensemble and collective emission is reported in the strongly coupled atom-cavity mode. By comparing our experimental observations to theoretical descriptions of collective emission and a numerical simulation, a discussion of the observed spontaneous emission is given. Continuous collective emission is required in order to surpass current state-of-the-art passive reference cavities stabilization techniques. However our set-up operates in a in a cyclic manner. Preliminary studies of quasi-continuous emission were carried out and consideration of future work necessary for achieving continuous collective emission is described.

ACKNOWLEDGEMENTS

This dissertation presents the result of the work done and the knowledge gained during my period as a M.Sc student.

I would first and foremost like to thank Jan W. Thomsen. Jan is a inspiring supervisor as well as a great educator. As a supervisor, Jan serves as a great motivation in pushing the capabilities of both my experimental and theoretical work forward. From an educational perspective, Jan's communication skills and his ability to keep his students 'in-the-loop', is an admirable feature and shows his willingness to take his students seriously.

Secondly, I would like to express my gratefulness towards the three PhD students: Bjarke Takashi Røjle Christensen, Stefan Alaric Schaffer and Martin Romme Henriksen. Their willingness to explain concepts and incorporate me into the work done in the Coldatoms group at the Niels Bohr Institute is deeply appreciated.

During my M.Sc. program I received a grant of 30.000 kr from the Siemens foundation. I would therefore like to thank them for believing in my work, and for providing the capital, thereby contributing to a further development of the experimental set-up at the Coldatoms group at the Niels Bohr Institute.

I would also like to thank PhD student and brother, Nicholas Mossor Rathmann for motivating me through years of studies and helping me with homework -and Matlab problems.

I would furthermore like to thank my mother Dorte Dyveke Rathmann, for her willingness to provide financial support during my M.Sc program insuring food on my table. Her continued interest in my studies through out the years kept me motivated and happy.

Finally, I would like to thank my good friend Sigurd Dan Gregers Mejlstroem who always shared his apartments with me. During my many visits a great number of talks of interesting theoretical physics were shared, expanding both his and my concept of reality.

CONTENTS

1 INTRODUCTION AND MOTIVATION 1
1.1 Passive stabilization of atomic clocks . . . 2
1.2 Outline of the Thesis . . . 6
2 ULTRA-STABLE LASERS 7
2.1 Active frequency standards . . . 8
2.2 Good -and bad cavity regimes . . . 8
2.3 Cooperativity . . . 10
2.4 Active light source . . . 11
3 ATOM-LIGHT INTERACTIONS 13
3.1 ^{88}Sr and the electronic level schematics . . . 13
3.2 Relevant laser systems . . . 16
3.2.1 The 689 nm laser . . . 19
3.2.2 Pulse-laser set-up . . . 23
3.2.3 The 461 nm laser . . . 27
3.2.4 The 679 nm and 707 nm repumping lasers . . . 29
4 EXPERIMENTAL SET-UP AND TECHNIQUES 31
4.1 Cooling and fixating the ^{88}Sr atoms . . . 31
4.1.1 Cooling light . . . 32
4.1.2 2-dimensional optical molasses technique . . . 34
4.1.3 Zeeman slower . . . 34
4.1.4 Magneto-Optical trap and temperature of atoms 37
4.1.5 Optical cavity . . . 42
4.2 Detection of coherent light . . . 45
4.2.1 Mechanical shutter . . . 47
4.3 Combining the Atom-cavity-pulse system . . . 50
5 COLLECTIVE SPONTANEOUS EMISSION 53
5.1 Theoretical outline of Super radiance, Super fluorescence and Amplified spontaneous emission . . . 53
5.1.1 Relevant characteristics . . . 55
5.1.2 Theoretical considerations and the simulation process . . . 57
5.1.3 Simulation results . . . 59
5.2 Conclusion and outlook . . . 72
6 PROSPECTS 75

I APPENDIX 77
A APPENDIX A 78
B APPENDIX B 79
C APPENDIX C 82

BIBLIOGRAPHY 83

LIST OF FIGURES

Figure 1 Schematics of the two reference parts used for a typical atomic clock. 3
Figure 2 Frequency accuracy and precision illustrated by red dots on a dart-board. 3
Figure 3 Plots of three Allan deviations. 5
Figure 4 Illustrations of the two cavity regimes. 9
Figure 5 Illustration of coherent coupling of the atom-cavity system g and the two decay rates (Γ, κ) for the atom and the cavity. 11
Figure 6 Illustration of the electronic energy level scheme of ^{88}Sr 14
Figure 7 Illustration of the three different lineshapes relevant for an ECDL. 18
Figure 8 Illustration of the Littman-Metcalf schematics used for an External Cavity Diode Laser (ECDL). 18
Figure 9 Illustration of the Littrow schematics used for an External Cavity Diode Laser (ECDL). 19
Figure 10 Illustration of the two different schematics used for frequency control in our experiment. 21
Figure 11 Illustration of the spatial overlap of the pulse-laser mode entering at an angle compared to the intra-cavity field mode and the MOT volume. 23
Figure 12 Plot of the linewidth from the injection-locked laser diode. 25
Figure 13 Plot of the laser diodes output power as the diode current is varied. 25
Figure 14 Illustration similar to figure 10, but with an injection locked slave laser using the the 0^{th} order mode of AOM1. 26
Figure 15 Plots of output power of the slave diode when injected (**a)**) and not injected (**b)**) by the frequency stabilized master laser. 26
Figure 16 Illustration of the force of the two counter-propagating lasers as a function of the velocity. 35
Figure 17 Illustration of the schematics of a Zeeman slower. 35
Figure 18 Schematics of a 1-dimensional MOT which show an illustration of the energy level splitting for an atom with a $J = 1$ and $J = 0$ transition, as the magnetic field strength increases. 38
Figure 19 Illustration of a 3-dimensional MOT. 40

Figure 20 **a)** An experimental cycle showing the various steps in obtaining intensity data via fluorescent atoms and **b)** Plot of the relative intensity, as a function of the off-time. 41
Figure 21 Schematics of an empty Fabry-Perot interferometer/cavity. 43
Figure 22 Illustration of the spectral overview of the NICE-OHMS technique. 46
Figure 23 **a)** shows the light intensity decay time of a MOT-arm in the x-axis and **b)** shows the light intensity decay time of the Zeeman-arm in the x′-axis. 48
Figure 24 **a)** shows the effects of a mechanical shutter place in front of a continuous beam and **b)** shows the cooling field mediated from the bow-tie cavity (red) and the shutter arm sequence as a function of time. 49
Figure 25 Experimental set-up for active lasing. 51
Figure 26 Illustration of super radiance (SR), super fluorescence (SF) and amplified spontaneous emission (ASE). 54
Figure 27 **a)** Simulated cavity transmission power and **b)** simulated atomic coherence. 60
Figure 28 **a)** Illustration of the sequence for the relevant lasers in testing the amount of excited atoms. **b)** illustration of the sequence for the relevant lasers for investigating of collective emission flash in this work. 63
Figure 29 Plots of the MOT fluorescence before and after a fraction of the laser cooled ^{88}Sr atoms were excited by a resonant pulse-laser. 63
Figure 30 Plot shows MOT fluorescence reduction normalized to an initial fluorescence level as a function of time in which the cooling lasers where switched off. 64
Figure 31 Transmission signal obtained during the laser pulse sequence shown in figure 28 **b)**. 65
Figure 32 **a)** shows the flash shape dependency on number of atoms and **b)** shows the flash shape peak height dependency on number of atoms and **c)**shows the flash peak delay dependency on number of atoms. 66
Figure 33 **a)** shows the pulse power dependency of the flash peak delay and **b)** shows the pulse power dependency of the flash peak delay. 67

Figure 34 **a)** shows the cavity transmitted flash measured by measuring the non-modulated transmission signal and **b)** shows the cavity transmitted flash measured by using the NICE-OHMS technique. 68
Figure 35 **a)** shows the flash shape for different intra cavity seed powers and **b)** shows the flash shape peak intensity for different intra cavity seed powers. 69
Figure 36 Illustration of the sequence for the relevant lasers for investigating of collective emission of two flashes in this work. 70
Figure 37 Transmission signal following two pulsed-lasers with different intermediate time. 71

LIST OF TABLES

Table 1 Electric dipole selection rules for the LS coupling scheme. 14
Table 2 Relevant linewidths and wavelengths for the atomic transitions of ^{88}Sr. 16

1 INTRODUCTION AND MOTIVATION

Frequency is the quantity that is measurable to the highest level of precision and accuracy. Because of this, a precise and accurate frequency is utilized in a great number of technological applications, as well as references for studies of fundamental physics. By utilizing a precise and accurate frequency, a timekeeping device known as an atomic clock can be constructed. The atomic clocks precision depends on its ability to repeat the exact same oscillation in an internal pendulum, and uses its accuracy to make sure the these repeated oscillations do not drift in time, compared to some true reference value.

The success of precision timekeeping with atomic clocks has led to the redefinition of quantities as the meter, which is no longer defined by a macroscopic stick but, but as the length of the path travelled by light in vacuum during a time interval of 1/299 792 458 of a second. This time-to-length translation is also utilized for a wide range of technological purposes. When measuring the relative time delay between four (or more) satellites, the Global Positioning System (GPS) can translate the time delay into a measurement of distance and thus pin-point a specific location on earth. The atomic clock ensures the precision and accuracy needed for a reliable GPS signal. Further use of the atomic clocks time resolution is found when detecting minute variations in earth's gravitational field, which can provide a real-time detection of tectonic shifts causing earthquakes. Atomic clocks are also utilized for their ability to provide precise and accurate measurement, when searching for drift of fundamental constants. The technological advantages made possible by utilizing atomic clocks, serves as a motivation for me to help the development of a compact system that bring the features of the atomic clock outside the laboratory and into the modern world. In order to realize such a compact system and improve the current state-of-the-art atomic clocks, a greater understanding of the inner components of an atomic clock is pursued. I wish to improve upon the method of precision measurement used in atomic clocks. To understand how improvements on precision measurement in atomic clocks are made, current limitations using a passive reference cavity to stabilizing state-of-the-art clocks, as seen in figure 1, must first be understood. Figure 1 shows a laser, which is stabilized to a passive reference cavity and achieves an absolute accuracy via an atomic reference. Similar for both the prestabilization and the absolute accuracy seen in figure 1 is the need for a reference. However, instead of a passive reference cavity, this dissertation seeks to utilize the atoms as a reference. Therefore the concept of a refer-

ence is treated.

Determining the level of precision and accuracy of atomic clocks is done by comparisons to a reference. When measuring the length of one's index finger, a comparison to another reference finger is needed. Only then can one determine if one's index finger is shorter or longer than the reference finger. The measurement of frequencies is done in a similar manner. Frequency precision can thus only be measured by comparing to another local oscillator with a precise reference frequency. The task is then to find a suitable reference frequency. Using non-quantum objects to define a quantity as the meter becomes a problem when duplication is attempted. A copy of a meter-stick will never be exact, as the number of atoms in the original meter-stick is near impossible to replicate. Thus some deviation in length between the original and duplicated meter-stick is inevitable. This becomes a problem when measurements at the nano-meter scale and below are required. Here problems arise as atoms may be added or subtracted from the meter-stick due to the surrounding environment. While the addition of a few atoms to a given reference may not be of much importance when measuring large objects such as the Eiffel tower within a precision of a meter or so, the addition of a few atoms to a reference is of importance when measuring the Eiffel tower to a precision of the atomic scale. Microscopic atoms thus provide a good alternative as a reference, as quantum mechanics states that two ^{133}Cs atoms are not just similar but identical, if kept under similar controlled environmental perturbations. These quantum references can thus be used anywhere in the universe, providing universally identical references. Using identical universal frequency references such as atoms thus serve as a great tool for a reference. This dissertation thus takes advantages of the quantum nature of atoms for an alternative of the passive reference cavity used for prestabilization as seen in figure 1. In order to explain why an alternative is needed, the current passive reference cavity of an atomic clock is investigated further.

1.1 PASSIVE STABILIZATION OF ATOMIC CLOCKS

Ideally, an atomic clock can produce a measurement that is fully reproducible and represent an exact time value. In other words the ideal atomic clock has no instability and has no inaccuracy. An atomic clock has an internal oscillator which is given in terms of a radiation field, typically originating from a laser. The laser field is stabilized to a well-defined frequency such as an empty reference cavity, thus reducing the frequency linewidth δf. To ensure accuracy, the laser field probes a narrow line atomic transition as reference. An illustration can be seen in figure 1, depicting the two central features of an atomic clock.

In general, atomic clocks can thus be split into two sections: accu-

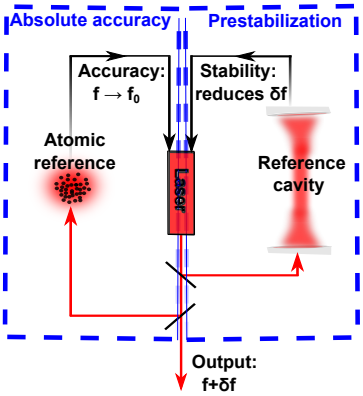

(a)

Figure 1: Schematics of the two reference parts used for a typical atomic clock. A laser is prestabilized to a ultra stable reference cavity using a feedback system, thus reducing the frequency noise δf. The laser is then sent to an ensemble of atoms and via another feedback system the laser frequency f is made to mimic the that of the atoms . This provides an absolute accuracy.

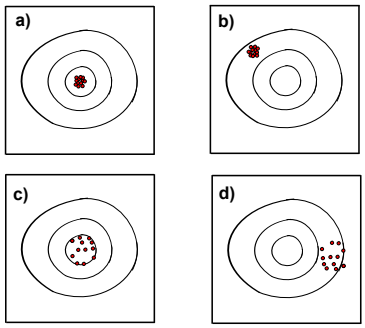

(a)

Figure 2: Frequency accuracy and precision illustrated by red dots on a dart-board. **a)** Accurate and precise. **b)** Inaccurate and precise. **c)** Accurate but not precise. **d)** Inaccurate and not precise

.

racy and stability/precision. In obtaining the accuracy of an atomic clock, a measurement of the deviation of the laser frequency from a reference frequency is performed. The reference frequency is then the atomic transition frequency ν_0. To obtain an accurate atomic clock, the oscillation frequency must be adjusted to match ν_0. The difference between accuracy and precision is not always clear, therefore figure 2 shows a graphical representation of accuracy and precision on a dart-board. Here subfigures a and c both show multiple accurate hits (red dots) on the dart board compared to the center. In terms of atomic clocks, this can be interpreted as an accurate and reproducible frequency compared to a reference frequency. Subfigures b and d on the other hand represent a frequency which reproducibility is inaccu-

rate compare to a reference frequency.

In evaluating the stability of an atomic clock, a measurement of the frequency variation in time is performed. In accounting for the fundamental uncertainties of the non-zero transition linewidth due to the uncertainty principal of quantum mechanics, multiple measurements of the transition frequency are needed. Sub-figure a and b both represent multiple reproducible precise measurements. This is in contrast to subfigures c and d which both represent imprecise measurement, where the frequency in not reproducible. In achieving stability, an empty cavity is often used as a frequency discriminator on its own. Here the fractional frequency instability $\frac{\delta\nu}{\nu}$ can be described in relation to the fractional length instability $\frac{\delta L}{L}$ of the cavity [1]:

$$\frac{\delta\nu}{\nu_0} = -\frac{\delta L}{L}. \tag{1}$$

This relation applies to a passive reference cavity. Thus the fractional frequency stability changes as the fractional length stability changes.

If an oscillator is stabilized to an atomic transition, the so-called Allan deviation is often used to describe the fractional frequency instability. The Allan deviation not only incorporates the relationship between the oscillator frequency and transition frequency (Q-factor or Quality factor), it also considers the Signal-to-Noise-Ratio (SNR) during the frequency measurement and the fraction of the total cycle time in which the average time the atoms are interrogated τ/T_c. The Allan deviation can thus be described by [1]:

$$\sigma(\tau) \propto \frac{1}{Q}\frac{1}{SNR}\sqrt{\frac{T_c}{\tau}} \propto \frac{1}{Q}\frac{1}{\sqrt{N}}\sqrt{\frac{T_c}{\tau}}, \tag{2}$$

where $Q = \nu_0/\Delta\nu$ and SNR is proportional to the square root of the number of atoms $\sqrt{N}$, for a system ultimately limited by the fundamental quantum projection noise. In order to reduce the fractional frequency instability of equation (2), longer average time τ can be implemented, a higher Q-factor can be implemented by choosing a narrow atomic transition and an increase in the sample size (N) can be implemented. A plot of an experimentally obtained Allan deviation from a laser stabilized to a reference cavity, is shown in figure 3. The relation between fractional frequency instability given by the Allan deviation in equation (2) can be seen in this plot. Here, the averaging time is shown to have a clear inverse relation to the fractional frequency instability. Raising the Q-factor is another parameter for lowering the Allan deviation. The microwave radiation used to probe the hyperfine ground state transition of the ^{133}Cs atom , yields a Q-factor of $\sim 2 \times 10^{10}$. However, using an optical radiation with frequencies of $\sim 100 \times 10^{12}$ Hz to probe a narrow transition linewidth $<$ Hz of an optical clock yields a Q-factor of 10^{16}-10^{18}. Thus the ^{133}Cs-clock has a fractional precision level of 10^{-15} [2]. However, state-of-the-art

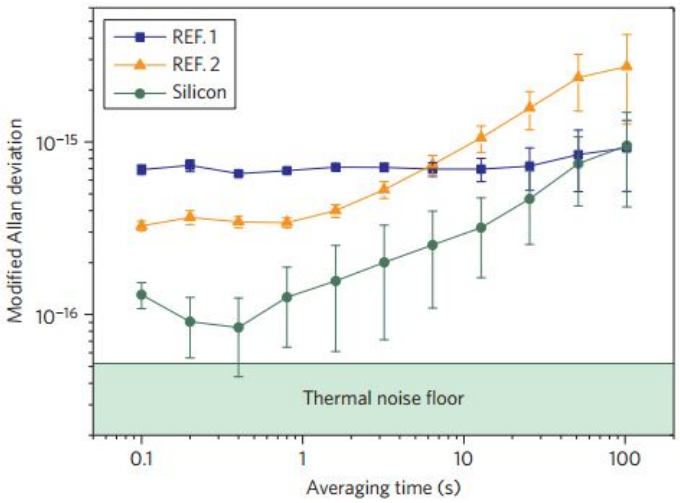

(a)

Figure 3: Plots of three Allan deviations. The data show the average instability of 130 data sets with a duration of 10 min each. Error bars represent the standard deviation of the data averaged for each point. Ref.1 and Ref.2 are conventional cavities, while the third cavity is made of mono-crystalic silicon. The predicted thermal noise floor of modified $\sigma_y \approx 5 \times 10^{-17}$ for the silicon cavity system is indicated by the shaded area. A inverse relation is seen between the averaging time an the fractional frequency instability. A noise floor from the cavity mirrors is expected to set a lower limit for the fractional frequency instability. Taken from [5].

atomic clocks using optical radiation continue to improve the precision beyond that of the ^{133}Cs-clock and fractional precision levels have reached 10^{-18} within a few hours of averaging time [3]. Thus the motivation to proceed with optical atomic clocks, is achieving a greater stability by gaining a higher Q-factor. The last parameter is the sample size N. The number of atoms does not changes or depend on weather a microwave clock or an optical clock is pursued. Thus the number of atoms can be optimized independently of the chosen type of atomic clock.

Different limitation are present in stability of passive reference cavities. In current state-of-the-art atomic clocks, the limitation for lowering the fractional frequency instability to below 10^{-18} is set by Brownian motion in the cavity martial and in the cavity mirrors [4]. These thermal fluctuations change the fractional length stability as seen in equation (1), thus resulting in a increased fractional frequency instability. For an empty cavity consisting of a spacer and mirrors, the thermal fluctuation spectrum can be described by the thermal dissipation theorem. Mirror fluctuations power spectrum G_{mirror} shows a signal power intensity in the frequency domain. The main contrib-

utor of thermal fluctuations can be attributed the cavity mirrors, due to thermal fluctuations and can be describe by [4]:

$$G_{mirror} \propto \frac{4k_B T}{\omega}, \tag{3}$$

where k_B is the Maxwell-Boltzmann constant, T is the cavity mirror temperature and ω is the angular frequency. Using the relation $G_{mirror} \sim \sigma_x^2$, where σ_x^2 is the square of the fluctuations of cavity mirror position, the cavity mirror fluctuation can be described by its dependence of its temperature:

$$\sigma_x \propto \sqrt{T}. \tag{4}$$

Thus in order to obtain higher fractional frequency stabilities using passive reference cavities limited by the thermal noise floor as seen in figure 3, the temperature must be lowered further.

This dissertation will seek a method to suppress the thermal noise on passive reference cavity mirrors, by reducing the importance of the passive reference cavity, thus leading the way to an ultra-stable laser.

1.2 OUTLINE OF THE THESIS

By utilizing an atom-cavity system in a regime where the linewidth of the collective emission of an atomic ensemble dominates the combined atom-cavity linewidth, an alternative approach that suppresses the thermal noise limit of passive reference cavities is given. The relationship between the cavity linewidth and the atomic linewidth is discussed and the interplay between the atomic ensemble and the cavity is given in chapter 2. A description of the laser systems used to cool and probe the atoms is given in chapter 3, with a focus on the set-up used for frequency control and the injection-locked pulsed-laser that I build. Chapter 4 describes the cooling of the atoms to the range of millikelvin and a mechanical light shutter that helps to further diminish any decoherence. Also a description of an optical cavity placed around the atoms is given in order to investigate the atom-cavity interaction. Chapter 5 reports a numerical -and experimental approach in achieving collective emission. Finally, chapter 6 motivates future work.

2

ULTRA-STABLE LASERS

Pursuing a method in which to reduce the Brownian motion limitations on the stabilities of current state-of-the-art atomic clocks reference cavities, this section describes the exploitation of a ultra-narrow atomic transition inside a cavity. It is here suggested that utilizing a system in which ultra-narrow transition of the ensemble of atoms determine the stability instead of the passive reference cavity, the thermal noise limitations on the reference cavity mirrors can be suppressed.

Several ideas to suppress the current thermal noise floor have been put forth. One idea is to cool down the optical cavity to cryogenic temperatures ($\leqslant$ 130 K°). Cooling down the cavity spacer and mirrors to cryogenic temperatures will ensure that temperature induced position fluctuations will be minimized. The position fluctuations of the cavity mirrors can be seen in equation 4 to be dependent of the square root of the temperature. Reports of cryogenic cooling of a cavity to 124 K° has been realized by [**5**]. Here a linewidth of 40 mHz was achieved. However, as mentioned earlier, the motivation in the dissertation is to realize a compact system. By using cryogenic cooling to lower the fractional frequency instability, adds to the complexity of the system. Therefore this idea is not utilized in this dissertation.

The idea pursued in this dissertation is to utilized the radiation emitted from a large ensemble of narrow transition linewidth atoms placed inside a cavity. The classical technique of using a empty optical cavity is combined with the quantum nature of the atoms. In contrast to the passive reference cavity approach, the cavity is not a frequency discriminator in our set-up. Instead the optical cavity is constructed such that its linewidth κ is much larger than the narrow transition probing linewidth Γ of the quantum emitters, thus entering the so-called bad cavity regime. In this regime the cavity does not serve as a frequency discriminator, but is primarily exploited for enhancing the atom-light interaction by increasing the effective length were atom-light interaction may take place. The atoms are then utilized for their emission with a natural ultra-narrow linewidth. The narrow transition linewidth of the atoms will then dominate linewidth of the combined emitted atom-cavity system, thereby reducing the importance of the cavity linewidth. This dissertation will thus seek to utilize so-called active frequency standards were radiation is emitted directly from the ensemble of atoms with a given collective linewidth. Reports of obtaining linewidths in the mHz range using active frequency standards in the bad cavity regime have been reported by

[6]. This dissertation thus strives to investigate the possibility of using an active frequency standard in order to experimentally realize an atom-cavity system that can suppress the importance of the traditional passive reference cavity system as a means of stabilization and thereby reducing the effects of the noise limit set by the Brownian motion i cavity mirrors.

2.1 ACTIVE FREQUENCY STANDARDS

At least two different types of techniques can be used towards stabilization, when using an active light source in the bad cavity regime. The first type is a feedback system were the laser is stabilized using the atomic phase induced dispersion signal. Recent reports [7], [8] at the Coldatoms group at Nils Bohr Institute have shown a proof-of-principle method for laser stabilization, using cooled atoms with a ultra narrow transition linewidth inside an vacuum sealed optical cavity. The atom induced phase dispersion signal is used as an error feedback signal, insuring a frequency stable output signal. The second type is a system using an active light source where the ensemble of atoms collectively emit coherent radiation of spectrally purity into the cavity. The first method is not pursued further in this dissertation as this work had already been realized by the time I entered the Coldatoms group at Nils Bohr Institute. Instead the second approach, which was in progress when I started my project, was pursued and is described in section 2.4. However, first an understanding of how to reduce the effects of Brownian motion in the cavity mirror by letting the atomic linewidth dominate is given in section 2.2. Afterwards an investigation of the regime in which collective emission is realized and how it is utilized, is given in section 2.3.

2.2 GOOD -AND BAD CAVITY REGIMES

Distinguishing between so-called good -and bad cavity regimes is crucial to the work done here. As mentioned before, distinguishing between the two different regimes is done by considering the relationship between the atomic linewidth profile Γ and an optical cavity linewidth κ. These two linewidth may be related to each other in two different ways as seen in figure 4.

The first way, $\kappa \ll \Gamma$, is the so-called good cavity regime where the cavity linewidth is much smaller that the atomic linewidth. Using [9], an expression for the general expected linewidth is given by:

$$\Delta\nu_{general} = \frac{h\nu}{4\pi}\frac{\kappa^2}{P_{out}}\left(\frac{\Gamma}{\kappa+\Gamma}\right)^2, \tag{5}$$

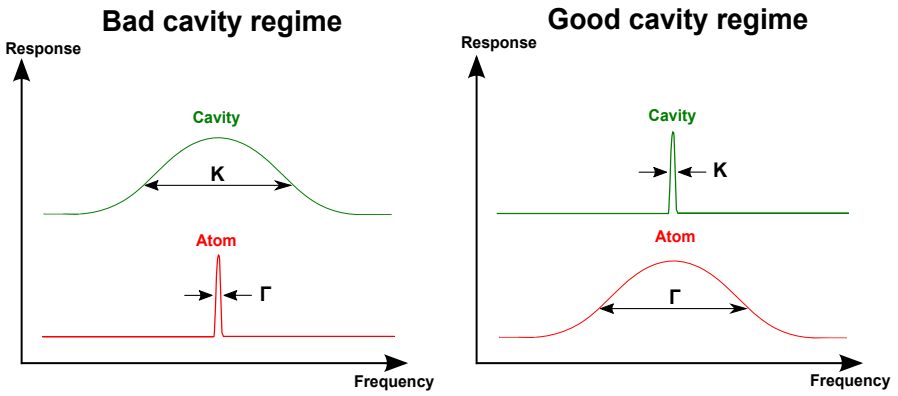

(a) (b)

Figure 4: Illustrations of the two cavity regimes. The comparisons of the cavity linewidth κ and the atomic linewidth Γ. **a)** depicts the good cavity regime in which $\kappa \ll \Gamma$ and **b)** depicts the bad cavity regime in which $\Gamma \ll \kappa$.

where P_{out} is the output power. In the good cavity regime ($\kappa \ll \Gamma$), equation (5) reduces to the Schawlow-townes limit linewidth:

$$\Delta\nu_{good} = \frac{h\nu}{4\pi}\frac{\kappa^2}{P_{out}}, \tag{6}$$

where only phase noise of spontaneous emission limits the lower bound of the achievable linewidth. Thus by building a cavity with a narrow linewidth and simultaneously operating at high output powers, a narrow linewidth in the good cavity regime is possible, according to equation (6). However, equation (5) does not take into account the fluctuations in the cavity length, often due to thermal perturbations. These changes in the cavity length lead to different resonance conditions and thus alters the cavity resonance frequency. Thus thermal noise in the cavity mirrors sets the limit for frequency stabilization.

In an attempt to suppress this problem the bad cavity regime ($\kappa \gg \Gamma$) is employed instead. In this regime, equation (5) reduces to:

$$\Delta\nu_{bad} = \frac{h\nu}{4\pi}\frac{\Gamma^2}{P_{out}}, \tag{7}$$

where the linewidth limit is dominated by the width of the atomic linewidth profile. The independence of κ makes the bad cavity regime much less sensitive the changes in the cavity length an thus much less sensitive to fluctuations in the position of the cavity mirrors. However, the combined atom-cavity linewidth is not considered independent of the cavity linewidth. The atom-cavity systems combined average lasing frequency is given by **[8]** $\nu_{avg} = (\Gamma\nu_c + \kappa\nu_a)/(\Gamma + \kappa)$, where the linewidths for our system are $\nu_a \sim$ kHz and $\nu_c \sim$ MHz. This description is used when the atomic resonant frequency ν_a is not identical

to the cavity resonant frequency ν_c. Thus if the good cavity regime is employed, fluctuations in the cavity length will lead to changes in the cavity resonance frequency ν_c, resulting in fluctuations in ν_{avg}. This effect is known as cavity pulling and a parameter (P) describing the system's sensitivity to cavity pulling is given by [8]:

$$P = \frac{d\nu_{avg}}{d\nu_c} = \frac{\Gamma}{\Gamma + \kappa}. \tag{8}$$

For the good cavity regime, equation (8) reveals that $P \approx 1$, resulting in a system very sensitive to cavity pulling. For the bad cavity regime, equation (8) reveals that $P \ll 1$, resulting in a system that is insensitive to cavity pulling. By using the bad cavity regime, the obtained linewidth is thus primarily sensitive to the atomic transition linewidth and not the cavity resonant linewidth. This dissertation therefore utilizes the bad-cavity regime where an active light source with spectrally pure radiation dominates the combined linewidth. The ensemble of atoms must however emit light as a collective, if the narrow linewidth of a single atom is to be replicated by the ensemble. In order for the ensemble to emit collectively, the coupling between the atoms and cavity must be greater than any dissipation terms from both the atoms and cavity. The parameter relating atom-cavity coupling and dissipation terms is the so-called cooperativity.

2.3 COOPERATIVITY

Essential to obtaining the desired collective emission, is the parameter called cooperativity. The single atom cooperativity C_0 is defined as $C_0 = 4g^2/\Gamma\kappa$, where g is the coupling constant between the atom and the cavity, and Γ, κ are the dissipation terms for a single atom and the cavity, respectively. C_0 can be interpreted as a measure of how strong the coherent atom-cavity coupling is for a single atom inside the cavity mode. However, in the case of an ensemble of atoms, it is often convenient to define the collective cooperativity: $C_N = C_0 N_{cav}$. Here N_{cav} is the total number of atoms within the cavity mode. The appropriate interpretation of C_N is a measure of how strongly all the intra-cavity atoms are coupled to the cavity mode. Another way of interpreting the collective cooperativity is a ratio between the rate of coherent scattering into the cavity mode and the rate of dissipation processes out of the cavity mode:

$$C_N = C_0 N_{cav} = \frac{4g^2}{\Gamma\kappa} N_{cav} = \frac{\text{Coherent coupling}}{\text{dissipation}}. \tag{9}$$

Thus the process of coherent coupling is given by the coupling constant squared g^2 and the two dissipation processes are described by the atomic spontaneous decay Γ rate and the cavity decay rate κ, as seen in figure 5.

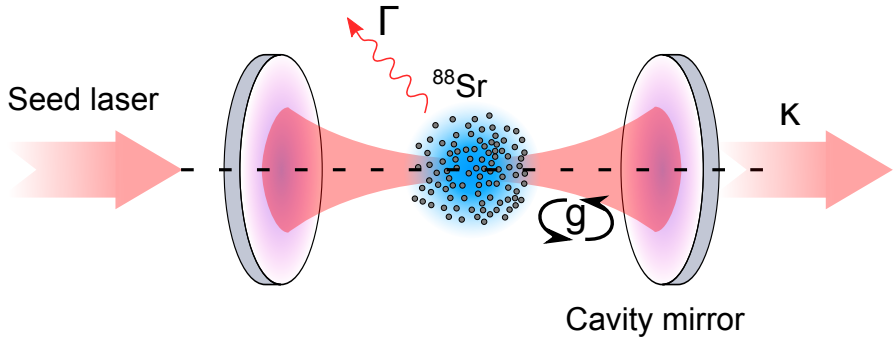

(a)

Figure 5: *Illustration of coherent coupling of the atom-cavity system* g *and the two decay rates* (Γ, κ) *for the atom and the cavity, respectively.*

Coherent collective emission will then build up inside the cavity if coherent scattering is larger than any dissipation effects ($C_N > 1$). The upper bounds on C_N is set by the number of atoms in the cavity mode and C_0 inverse dependency of the cavity linewidth. The cavity linewidth must not be too small nor too large, as a large cavity linewidth would give rise to an undesired low value of C_N whiles a small cavity linewidth would violate the bad cavity regime. Furthermore, the linewidth of the coherent light is not expected to inherit the natural linewidth Γ of the atomic transition. Instead in the limit of $C_N > 1$, the single atom cooperativity will be dominant and a theoretical minimum value for the transition linewidth will be given as $\Gamma_{min} = C_0\Gamma$ [**6**]. Exploiting a narrow transition linewidth of kHz and a low single atom cooperativity $C_0 \approx 10^{-4}$ in the limit of $C_N > 1$, Γ is expected to be reduced from kHz to mHz. This prediction is tested in section 5.

By utilizing the bad cavity regime and the collective cooperativity in the limit of $C_N > 1$, a description of an active light source approach to achieve laser stabilization is now given.

2.4 ACTIVE LIGHT SOURCE

Entering the regime of $C_N > 1$, the ensemble of atoms are expected to act collectively and emit coherent radiation. The atoms in the bad cavity regime will act as a frequency discriminator compared to the pre-stabilized light and the atoms will in principle determine both precision and accuracy of the outgoing field. The combined atom-cavity system in the bad cavity regime, will emit outgoing radiation with a linewidth dominated by the atomic transition, according to equation (7). As described in section 2.2, the effective linewidth could potentially be much smaller than the atomic probing transition. This

would result in spectrally pure radiation. As the active light approach demands the bad cavity regime, the cavity puling effect describe in section 2.2 can be seen to be of little importance, as $P \ll 1$. Thus an active light source may suppress the noise limit seen in state-of-the-art passive reference cavity approaches and provide a ultra-stable laser.

The experimental set-up used in this work is of a cyclic nature. Thus collective emission of spectral purity is expected to manifest itself in short, coherent flashes. In order to measure the spectral purity of the emission radiation a continuous level of collective emission is desired. This is not possible within the experimental set-up used for this dissertation. Firstly an incoherent pumping of the excited radiation level is required using a 3 (or more)-level atomic scheme. If using a 2-level atomic scheme a steady state flow of new atoms is required to make sure the outgoing linewidth does not inherit any characteristics of the excitation laser. This dissertation will show a proof-of-concept, using a cyclic experimental measurement scheme and 2-level coherent excitation laser. However, future experimental set-up's that will realize continuous measurements are already under construction and its prospects will be described further in section 6.

In order to perform a cyclic measurement of the coherent emission from an ensemble of atoms, different atom-light interactions are needed. The following section will thus describe the atom used in the atomic ensemble and the laser systems used to interact with the different transitions in the atom.

3

ATOM-LIGHT INTERACTIONS

In the previous section, a motivation for using optical frequencies was given in order to achieve a large so-called Q-factor and thus lowering the fractional frequency instability. In this section, the choice of 88-Strontium (^{88}Sr) as the atom used in our system, is motivated by its electronic level schematics. In addition to having an optical probing transition with a narrow linewidth, the ^{88}Sr atom is also susceptible to manipulation in velocity-space and in position-space using a so-called cooling-transition. This section thus investigates the relevant ^{88}Sr transitions by considering the electronic level schematics. Furthermore, an explanation of the lasers used for interacting with the relevant ^{88}Sr transitions are given by explaining the stability manipulation and frequency control of the lasers.

3.1 ^{88}Sr AND THE ELECTRONIC LEVEL SCHEMATICS

Strontium is an alkaline earth metal, placed in the second main group in the periodic table. Natural strontium consist of different isotopes, but the most common isotope is the bosonic ^{88}Sr, which is used in this work.

Investigating ^{88}Sr, the electron configuration is given by: $(1s)^2(2s)^2(2p)^6(3s)^2(3p)^6(3d)^{10}(4s)^2(4p)^6(5s)^2$ revealing two valence electrons in the 5s-shell. The two valence electrons both have a spin component(s_1, s_2) and both are equal to 1/2. In the ground state of ^{88}Sr, the total spin ($S = s_1 + s_2$) is zero, as s_1 and s_2 are aligned in an anti-parallel configuration. However, in the excited state the two spin components can choose to align parallel or anti-parallel in respect to each other, resulting in a total spin of either $S = 1$ or $S = 0$, respectively. Another relevant atomic quantization is the total orbital angular momentum ($L = \sqrt{l(l+1)}\hbar$), where l is the azimuthal quantum number for an atomic orbital. The relevant orbital angular momentums for ^{88}Sr are $L = 0, 1, 2$ which can be rewritten as S,P and D, respectively. Knowing that the total angular momentum J can be written by the sum of the total spin and the total orbital angular momentum ($\vec{J} = \vec{S} + \vec{L}$), the quantized values can all be gathered in the Russell-Saunders notation: $^{2S+1}L_J$. This Russell-Saunders notation can be used in the so-called LS-coupling regime of weak spin-orbit coupling where the energy of the residual electrostatic interaction between the electrons is much bigger than the energy of the spin-orbit interaction. The Russell-Saunders notation will be used to describe the electronic level scheme.

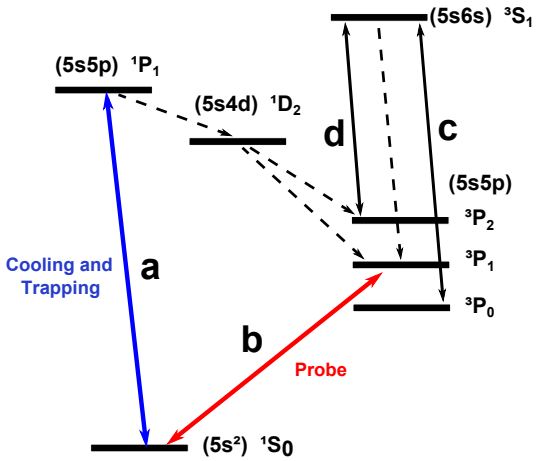

(a)

Figure 6: *Illustration of the electronic energy level scheme of* ^{88}Sr. *Arrows indicate allowed transitions. Full lines indicate transitions driven by lasers and dotted lines indicate decay channels. The cooling transition is used to cool and trap the atoms and is shown in blue, whiles the red line is used for probing the atoms. Furthermore the atom emission is expected to appear at this transition. Relevant linewidth for all laser transitions (**a**,**b**,**c** and **d**) are given in table 2 .*

When considering the LS-coupling scheme, the electric dipole selection rules must also be included. The electric dipole selection rules determine which transition are allowed, by invoking general rules that electric dipoles transitions must obey. Using [**10**], different electric dipole selection rules dictate which electronic transitions are allowed and are presented in table 1.

Table 1: *Electric dipole selection rules for the LS coupling scheme [**10**]. Transition rules for relevant quantum numbers are given. Rule 3 essentially puts a restriction on the parity of absorbed and emitted photons, between an excited state (e) and the ground state (g).*

1) $\Delta J = 0, \pm 1$	$(J = 0 \leftrightarrow J' = 0)$
2) $\Delta M_J = 0, \pm 1$	$(M_J = 0 \leftrightarrow M_{J'} = 0 \text{ if } \Delta J = 0)$
3) $(-1)^{l_e} = \pi_P (-1)^{l_g}$	No parity changes
4) $\Delta l = 0, \pm 1$	
5) $\Delta L = 0, \pm 1$	$(L = 0 \leftrightarrow L' = 0)$
6) $\Delta S = 0$	

Now the electric dipole selection rules of table 1, can be applied to the transitions of the ^{88}Sr atom. Thus the electronic level scheme for ^{88}Sr is shown in figure 6.

Using table 1, the $^1S_0 \leftrightarrow {}^1P_1$ transition can be seen to be a strongly dipole-allowed transition. The $^1S_0 \leftrightarrow {}^1P_1$ transition can be accessed

by using light with wavelength $\lambda = 461\,nm$ and has a transition linewidth of $\Gamma/2\pi = 32\,MHz$. This transition is a rather broad transition, meaning that the decay time of the excited stay is relatively short ($\tau = 5.22\,ns$). As the $^1S_0 \leftrightarrow {}^1P_1$ transition has a short decay time it is ideal for cooling as the transition can be driven at a very high rate. A high excitation rate is useful if many photon-atom interactions are desired over a short span of time. Thus the atoms can absorb the momentum of photons at a high rate, changing the atomic momentum in the progress. If the photon momentum is absorbed from the right direction, the atom will loss velocity and is thus 'cooled'. Thus the high probing rate of the $^1S_0 \leftrightarrow {}^1P_1$ transition is ideal for for cooling the ^{88}Sr atoms and later confining and trapping them.

Another central transition line is the dipole-forbidden $^1S_0 \leftrightarrow {}^3P_1$ probing transition. Using table 1, this transition is seen to be dipole forbidden due to the spin-flip involved and thus has a relatively long decay time $\tau = 22\,\mu s$, compared to the $^1S_0 \leftrightarrow {}^1P_1$ transition. The linewidth is $\Gamma/2\pi = 7.5\,kHz$ and is considered narrow compared to the broad $^1S_0 \leftrightarrow {}^1P_1$ linewidth. The other levels in the triplet P-state are furthermore spin-forbidden, when decaying to the $^1S_0$ ground state. The $^1S_0 \leftrightarrow {}^3P_2$ and $^1S_0 \leftrightarrow {}^3P_0$ therefore both have a linewidth of sub hertz. Whiles a sub hertz linewidth is desirable in our system, to drive the $^1S_0 \leftrightarrow {}^3P_2$ and the $^1S_0 \leftrightarrow {}^3P_0$ transitions would put large requirements on a probing lasers. These large requirements on a probing lasers is not desirable for the work done in this dissertation, as a proof-of-concept is sufficient here.

In principle describing these three levels ($^1S_0$,$^1P_1$ and $^3P_1$) and their transitions are sufficient to understand how the cooling and probing of the ^{88}Sr is executed for our system. However, these levels are not entirely decoupled, as can be seen in figure 6. The $^1P_1$ state can also decay to the $^3P_1$ and $^3P_2$ via the $^1D_2$ state. The atoms in the $^3P_1$ and $^3P_2$ state are long lived as their decay to the $^1S_0$ state is both dipole-forbidden and spin-forbidden. Here 'long lived' refers to a time scale that is larger than the relevant time scale of for this experiment. The atoms in the long lived state are thus considered 'dark' as they do not participated with any dynamics within our systems, for all relevant time scales. However, in order to maximize the number of available atoms for the probing transition, these dark atoms must decay to the ground state on a time scale smaller than that their natural decay time. In order to reach reduce the number of dark atoms, the electron must get to the $^3P_1$ state with faster decay time $\tau = 22\,\mu s$. If the $^1D_2$ level decays to the $^3P_2$ state, a resonant laser will re-excite it to the $^3S_1$ level with a fast decay rate. From here the atom may decay to either one of the triplet P-states. However a similar laser ensures that a decay to the $^3P_0$ level will re-excite the atom back to the $^3S_1$ level. Thus eventually the $^3S_1$ level will decay to the $^3P_1$ level and back down to the ground state. The two different resonant lasers driv-

ing the $^3S_1 \leftrightarrow {}^3P_2$ transition and $^3S_0 \leftrightarrow {}^3P_0$ transitions are known as repumping lasers and ensure that no atoms are left dark to the probe laser or to the cooling laser. The relevant transitions probed by above mentioned lasers are shown in table 2.

Table 2: *Relevant linewidths and wavelengths for the atomic transitions of* ^{88}Sr*, indicated by a,b,c and d in figure 6.*

Relevant transitions	Wavelength (λ)	Linewidth ($\gamma/2\pi$)	Decay time (τ)
a) $^1S_0 \leftrightarrow {}^1P_1$	461 nm	32 MHz	5 ns
b) $^1S_0 \leftrightarrow {}^3P_1$	689 nm	7.5 kHz	22 µs
c) $^3P_0 \leftrightarrow {}^3S_1$	679 nm	1.4 MHz	112 ns
d) $^3P_2 \leftrightarrow {}^3S_1$	707 nm	6.4 MHz	24 ns

In conclusion, four laser systems are used, corresponding to the relevant transition in table 2: A cooling laser with $\lambda = 461$ nm, a probing laser system at $\lambda = 689$ nm for interrogation of the atoms and two repumping laser with $\lambda = 679$ nm and $\lambda = 707$ nm, minimizing the number of dark atoms. These four lasers are central to the work perform in this dissertation. Therefore a detailed examination of the construction of the different laser system is given.

3.2 RELEVANT LASER SYSTEMS

Different lasers are used to interact with the mentioned relevant atomic transitions, as seen in table 2. Here a description of the four relevant semiconductor lasers, all based on laser diodes are given. In order to manipulate the linewidth and frequency of the laser diodes to meet the wanted requirements of interacting with a relevant atomic transition, the laser diodes are incorporated into a set-up called a 'Extended Cavity Diode Lasers' (ECDL). First, the ECDL scheme will be explained, as it is central to all the lasers used in this work. Afterwards focus will swift to the $\lambda = 689$ nm laser. Here, an explanation of the set-up used for frequency control is given and an explanation of an injection-locked laser scheme is given. Then a brief explanation of the $\lambda = 461$ nm frequency doubled cooling laser set-up is given. Finally, a breif explanation of the two $\lambda = 679$ nm -and $\lambda = 707$ nm repumping lasers is given.

3.2.0.1 *External Cavity Diode Laser*

Central to all laser systems used in this work, is the semi-conducting diode laser with an external cavity surrounding it. This set-up is know as a External Cavity Diode Laser (ECDL). The diode laser consists of a spectrally broad gain-medium which is contained by two reflecting surfaces acting as an internal cavity. The internal cavity acts

to some extend as a frequency discriminator, as it only allows wavelengths that fulfil the resonant condition for standing wavelengths:

$$\lambda_m = \frac{2nL}{m}, \tag{10}$$

where n is the refractive index of the cavity material, L is the internal cavity length and m is the mode number of the internal cavity. The spectral linewidth of the allowed modes of the internal cavity that fulfil equation (10), can be described by $\delta\nu \propto \frac{1-R}{\sqrt{R}}$, which is valid for $R > 0.5$ where R is the light intensity reflectivity from a single internal cavity surface. However, the diode lasers do not meet the requirements of emission with a spectrally narrow linewidth. Therefore an external cavity is implemented, by extending the internal cavity with a mirror. By implementing an external cavity, further restrictions of allowed modes are set. The result is a emission linewidth which is more narrow than without an external cavity. In this way, a desired spectral linewidth of the emission can be obtained. An illustration of the different linewidths present in an ECDL are shown in figure 7. The figure shows how the external cavity restricts the modes allowed, resulting in a further narrowing of the linewidth, compared to the internal cavity.

The ECDL will typically lase at a frequency ν_0 and mode corresponding to the overlap of the three gain spectra, as illustrated in figure 7. By adjusting the diode temperature and current the internal cavity length can be changed, granting some degree of control of the allowed internal cavity modes. The external cavity can also be controlled to favour certain cavity modes by adjusting the angle of a inserted diffractive grating and or by adjusting the cavity length. Adjusting these parameters allows for a certain frequency to be favourable. The end result is a desired frequency ν_0 with a spectral linewidth of a few MHz.

Two types of ECDL configurations are used in this work, the Littman-Metcalf configuration which is used for the $\lambda = 679\,nm$ and the $\lambda = 707\,nm$ laser, and the Littrow configuration which is used for the $\lambda = 689\,nm$ and the $\lambda = 461\,nm$ laser. The two types of ECDL configurations are thus described in the following.

The Littman-Metcalf configuration can be seen in figure 8. The Littman-Metcalf configuration takes advantages of a diffractive grating which scatters the 0^{th} order light and the -1^{st} order light at different angles. The 0^{th} order light is used as the laser output, whiles the -1^{st} order light is retroreflected off a mirror and back into the cavity via the diffractive grating. In the Littman-Metcalf configuration the grating is fixated while the mirror angle is adjustable. The advantage of the Littman-Metcalf configuration is that the output beam direction is not affected by changes in the mirror angle. Using the internal cavity surface as a second mirror, creates an external cavity with a large length, thus resulting in a set of spectrally narrow

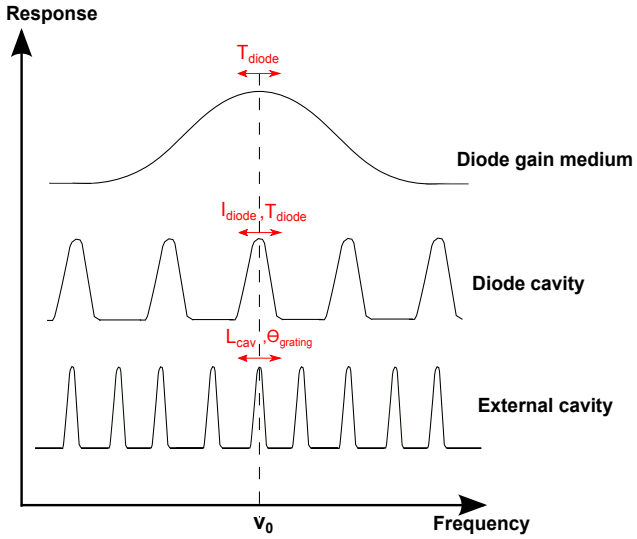

(a)

Figure 7: *Illustration of the three different lineshapes relevant for an ECDL (Not to scale). The diode gain lineshape can be move around the center frequency μ_0 by tuning the temperature of the diode T_{diode}. The internal diode cavity lineshape can be moved around the center frequency μ_0 by tuning the current given to the diode I_{diode} as well as the temperature of the diode T_{diode}. Lastly, the external cavity lineshape can be moved around the center frequency μ_0 by tuning the length of the cavity L_{Cav} and by adjusting the angle of the grating $\theta_{grating}$ with respect to the diode field. All lineshapes must overlap in order to achieve the wanted laser emission linewidth.*

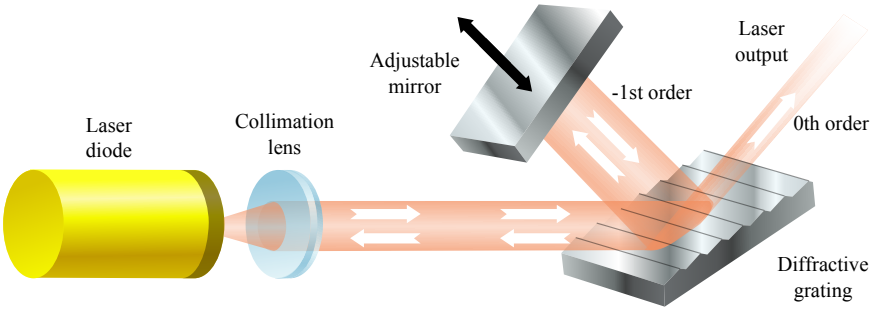

(a)

Figure 8: *Illustration of the Littman-Metcalf schematics used for an External Cavity Diode Laser (ECDL). The light exiting the diode is collimated and then split on a grating. The -1^{st} order mode is reflected off a adjustable mirror and sent back into the diode, The 0^{th} order mode is coupled out of the ECDL and used for a specific purpose. By adjusting the mirror of the external cavity, the total cavity length can be adjusted independently of the grating position. Figure adapted from [7].*

linewidth. The spacing between allowed modes can be describe by the Free Spectral Range (FSR) of the external cavity and is given by:

$$FSR = \frac{c}{2nL}, \tag{11}$$

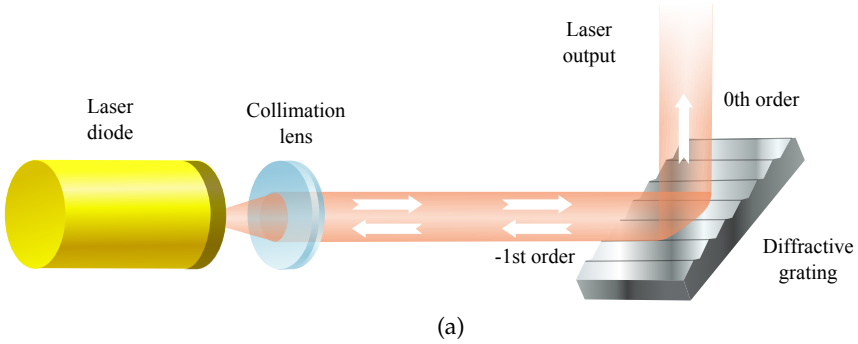

Figure 9: *Illustration of the Littrow schematics used for an External Cavity Diode Laser (ECDL). The light exiting the diode is collimated and then split on a grating. The -1^{st} order mode is reflected off the grating and sent back into the diode, The 0^{th} order mode is coupled out of the ECDL and used for a specific purpose. By adjusting the grating position, the total cavity length can be adjusted. Figure adapted from [7].*

where c is the speed of light in vacuum. Using the FSR that incorporates the diffractive grating, an expression for the external cavity linewidth is then given by:

$$\delta\nu = \frac{FSR}{\mathcal{F}}, \tag{12}$$

where $\mathcal{F}$ is the cavity finesse and is interpreted as the average number of retro-reflections of a photon in a cavity times π. Equation (11) and (12) thus state that a linewidth narrowing using an external cavity is possible by increasing the length (L).

In order to further stabilize the cavity length, temperature stabilization of the laser diode is also employed, but will not be mentioned in details in this dissertation.

The Littrow configuration can be seen in figure 9. The Littrow configuration also uses a diffractive grating but unlike the Littman-Metcalf configuration, has no external mirror. The diffractive grating again splits the collimated light into a 0^{th} order light and the -1^{st} order light, at different angles. The -1^{st} order light is then directed back into the diode and forms an external cavity, using the rear end surface of the diode as a second mirror. In the Littrow configuration the diffractive grating is adjustable and can be fine tuned using fine-pitch screw. This ensures the wanted wavelength can be selected.

3.2.1 *The 689 nm laser*

Based on a ECDL configuration, a laser system was set up to probe the $^1S_0 \leftrightarrow {}^3P_1$ transition. As this transition can be used for stabilization of an atomic clock, this laser will here forth be referred to as the 'clock laser'. The clock laser is based on an Littrow-ECDL configuration producing optical radiation with a frequency linewidth

in the order of a few MHz. The Littrow-ECDL configuration frequency linewidth is therefore further reduced, by an external cavity, to $\leqslant \Gamma/2\pi = 7.5\,\mathrm{kHz}$ to match the atomic linewidth of the ${}^1S_0 \leftrightarrow {}^3P_1$ transition. In order to so, an external cavity was build. Exposing the cavity to radiation with a linewidth of MHz and exploiting a so-called Pound-Drever-Hall feedback loop, the laser diode current could be controlled in order to mode match the high finesse cavity ($F \approx 8000$). A high finesse correlates to a very narrow resonance condition translating into the emission of radiation with a kHz linewidth, as can be seen in equation (12). This dissertation does not seek to further explain the set-up and techniques used to achieve a spectral linewidth narrower than the natural linewidth of ${}^1S_0 \leftrightarrow {}^3P_1$ transition for the 689 nm laser, as my work was limited to frequency control rather than the frequency stabilization of the clock laser. For a more detailed explanation of the clock laser stabilization, the reader is referred to [8]. However, a detailed explanation of the frequency control of the clock laser is given in this dissertation.

Due to the inadequate accuracy of a man-made cavity, the central frequency may lie far from the ${}^1S_0 \leftrightarrow {}^3P_1$ transition frequency of the atoms. In our set-up the laser frequency ω_l was detuned 37.00 MHz from the resonant ${}^1S_0 \leftrightarrow {}^3P_1$ transition with a resonant frequency ω_0. Thus before the radiation with frequency ω_l could be used to probe the ${}^1S_0 \leftrightarrow {}^3P_1$ transition of the ${}^{88}Sr$ atoms, it was sent through several Acoustic Optical Modulators (AOM), enabling frequency control. Two different frequencies manipulations were desired in our systems, both can be seen in figure 10 and both will now be described and motivated.

The first set-up for frequency manipulation, already in place as I joined the Cold atoms group at the Nils Bohr Institute, consists of two double pass AOM's. The initial frequency of the clock laser (ω_l) propagates through the first AOM (AOM1) with a modulation frequency of $\omega_1 = 345.56\,\mathrm{MHz}$. Selecting the light -1^{st} order to propagate back through the same AOM results in a total change in frequency corresponding to twice that of ω_1. Afterwards, the light propagates through a second AOM (AOM2) with a modulation frequency of $\omega_2 = 327.06\,\mathrm{MHz}$. However, this time selecting the $+1^{st}$ order to propagate back through the same second AOM, resulsts in a further frequency change corresponding to twice that of ω_2. Thus the total frequency change of the clock laser can be described by:

$$\begin{aligned} \omega_l &\Rightarrow \omega_0 + 2\pi \cdot (37.00\,\mathrm{MHz} - 2 \cdot 345.56\,\mathrm{MHz} + 2 \cdot 327.06\,\mathrm{MHz}) \\ &= \omega_0. \end{aligned} \tag{13}$$

Thus the clock laser frequency (ω_l) is on resonance with the ${}^1S_0 \leftrightarrow {}^3P_1$ transition frequency (ω_0). The second set-up for frequency manipulation, which I set up, also consists of two AOM's. In this

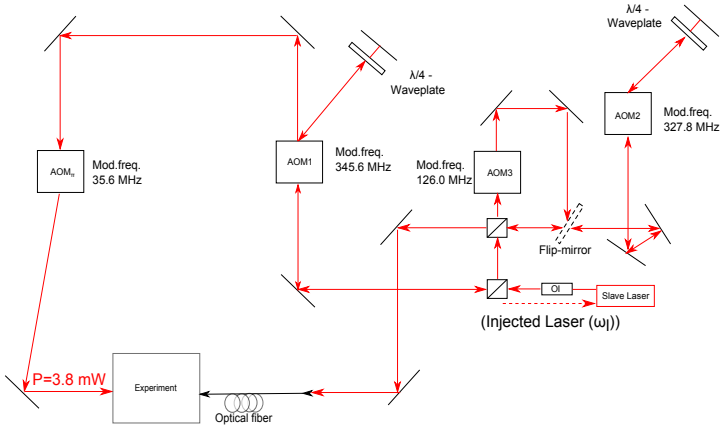

(a)

Figure 10: *Illustration of the two different schematics used for frequency control in our experiment. When manipulating the initial frequency ω_l, the initial light was sent into one of two paths. Following the path into one of two Acoustic optical modulator (AOM) configurations, the light sent into the optical cavity is either on resonance with the atomic transition ω_0 or moved one Free spectral Range (FSR) away from resonance to $\omega_0 + \mathrm{FSR}$. The 0^{th} order mode from AOM1 is frequency modulated by AOM_π and the resonant light then enters the experiment at an angle compared to the light entering the optical cavity. The power level of the light reaching the cavity is* $\mathrm{P} = 3.8\,\mathrm{m}W$

set-up, the goal is to manipulate ω_l in such a way, that the laser frequency can be shifted exactly one FSR away from the resonance frequency (ω_0). In order to do so, the light is again first led through AOM1, with a modulation frequency of $\omega_1 = 345.6\,\mathrm{MHz}$. Again, selection the light -1^{st} order to propagate back through the same AOM, resulting in a frequency change of the light corresponding to twice that of ω_1. However, a new AOM (AOM3) is inserted and used and the light then makes a single pass through AOM3 with a modulation frequency of $\omega_3 = 127.02\,\mathrm{MHz}$. The light from the -1^{st} order is then selected, corresponding to a frequency of ω_3. Thus the total frequency change of the clock laser is be described by:

$$\begin{aligned}\omega_l &\Rightarrow \omega_0 + 2\pi \cdot (37.00\,\mathrm{MHz} - 2 \cdot 345.56\,\mathrm{MHz} - 127.02\,\mathrm{MHz}) \\ &= \omega_0 + \mathrm{FSR}.\end{aligned} \tag{14}$$

Here the Free Spectral Range of the cavity is 781.14 MHz.

Although the modulation frequency and amplitude of AOM3 are kept constant, AOM2's modulation frequency and AOM1's amplitude are controlled by a computer. By modulating the frequency of AOM2 in small discrete steps the atomic response is monitored to find the exact resonance between the light and the atoms. The amplitude modulation of AOM1 is also controlled by a computer, in order to maintain a constant output power. The amplitude modulation is

done to counteract thermal perturbations of the optical fiber (as seen in figure 10), that otherwise will result in intensity fluctuations of the frequency manipulated light. As the laser beam travels through the two set-ups, it loses power at every surface it meets. To achieve sufficiently high power at the experiment stage, the initial power output of the $\lambda = 689\,nm$ ECDL is not sufficient. Higher power levels can be achieved by injection-looking a slave-diode laser to the $\lambda = 689\,nm$ ECDL laser, making the $\lambda = 689\,nm$ ECDL laser a so-called master laser. The method of injection locking will be treated in section 3.2.2.

The original $\lambda = 689\,nm$ ECDL linewidth has thus been manipulated in order to achieve a linewidth similar to that of the ${}^1S_0 \leftrightarrow {}^3P_1$ transition linewidth (7.5 kHz) and by frequency control, the frequency in the first set-up, is shifted to match that of the resonant transition ${}^1S_0 \leftrightarrow {}^3P_1$ transition or in the second set-up, is shifted by one FSR with respect to the cavity. After the frequency control, the light is coupled into the cavity by an optical fiber. However, a fraction of the cavity coupled light leaks out of the cavity mirror and is recorded. Using a feedback system controlling a piezo-element, the cavity length can be stabilized to match the resonance condition of the manipulated light of both ω_0 and $\omega_0 + FSR$. If the light entering the cavity has a frequency of $\omega_l = \omega_0$, the atoms can be expected to interact with the cavity coupled light. However if the light entering the cavity has a frequency of $\omega_l = \omega_0 + FSR$, an Electrical Optical Modulator (EOM) is applied to the light field, before coupling with the cavity. The EOM is modulated with a frequency of exactly one FSR of the cavity, thereby creating two frequency components (sidebands) around the initial frequency component (carrier), with an equal but opposite amplitude proportional to the modulation amplitude. Thus applying an EOM to the light entering the cavity, results in one of the sidebands being resonant with the ${}^1S_0 \leftrightarrow {}^3P_1$ transition. The power level of the sidebands can then be altered by tuning the modulation amplitude of the EOM. This method is later referred to as sideband probing. When using the second set-up, allowing for sideband probing, the cavity is kept stabilized to the resonant carrier with a large amplitude, located one FSR away from the ${}^1S_0 \leftrightarrow {}^3P_1$ transition. Thus the sideband, resonant with the ${}^1S_0 \leftrightarrow {}^3P_1$ transition, can then potentially be removed without disturbing the cavity stabilization scheme. Keeping the cavity length stabilized, ensured that radiation from the ${}^1S_0 \leftrightarrow {}^3P_1$ will still be resonant with the cavity. This will be crucial, when detecting collective emission without a continuous intra-cavity field resonant with the ${}^1S_0 \leftrightarrow {}^3P_1$ transition.

The $\lambda = 689\,nm$ ECDL light with the kHz linewidth with frequency ω_l, is further more used for a pulse-laser set-up. In our experiment, the purpose of a pulse-laser set-up, is to deliver a coherent radiation pulse, resonant to the ${}^1S_0 \leftrightarrow {}^3P_1$ transition, resulting in a coherent excitation to from the ground state to the ${}^3P_1$ state. If the atom coop-

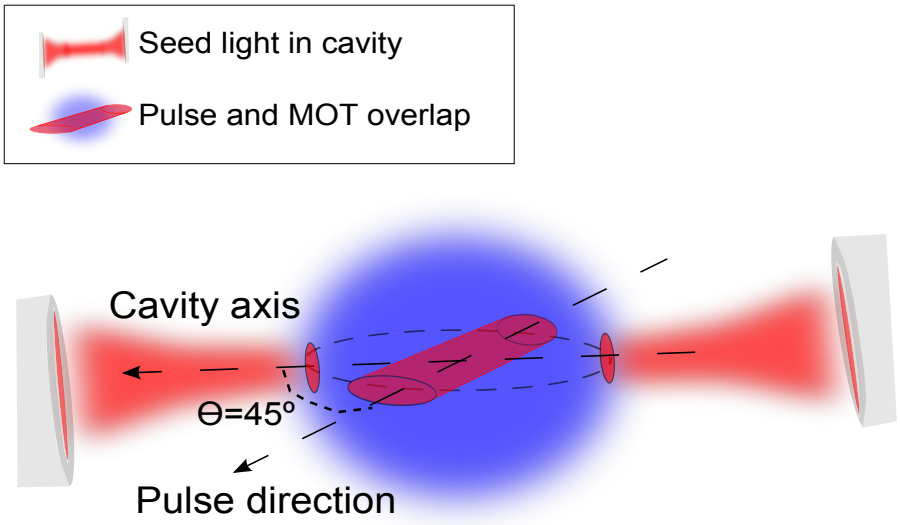

(a)

Figure 11: *Illustration of the spatial overlap of the pulse-laser mode entering at an angle compared to the intra-cavity field mode and the MOT volume (Not to scale).*

erativity is larger then the atom-cavity dissipation processes, a collective emission of the atom ensemble may be detected, as described in section 2.3. Therefore, the set-up of such a pulse laser is treated.

3.2.2 *Pulse-laser set-up*

The pulse-laser is central to achieving collective emission. The pulse-laser emits so-called π-pulse of radiation that excites the atoms coherently from the ground state to the excited $^3P_1$ state. The construction of the pulse laser and the considerations in doing so, are now treated.

As seen in figure 10, the 0^{th} order light exiting AOM1 was sent through AOM_π with an applied modulation frequency of 37.00 MHz. The resonant -1^{st} order light was then led into the cavity x-y-plane at an 45° angle with respect to the cavity axis as seen in figure 11. Furthermore a pulse-generator is connected the AOM_π. Thus only a pulse of the -1^{st} order resonant light with a set duration t_π, will be led into the cavity x-y-plane at an angle, instead of a continuous beam. The polarization of the pulse-laser light is also investigated and is treated in section 5.1.3. As the light passes through AOM_π, the pulsed laser light achieves a maximum power of $P = 3.8\,mW$. Other set parameters of the pulsed laser light is the area (A) of the applied pulse. The area of the applied pulse is measured using a CCD-camera. Taking beam divergence of the pulsed laser leaving AOM_π into account, the FWHM of the intensity profile is then measured, which results in $A = 1.19\,mm^2$. Given a saturation intensity $I_0 = 3\,\mu W/cm^2$,

a theoretical optimal pulse duration can be found when fulfilling the relation between the π-pulse power and pulse duration:

$$P = \frac{2I_0\pi^2 A}{\Gamma^2 t_\pi^2}. \tag{15}$$

The pulse duration t_π is thus calculated and set to $1.8\,\mu s$. However, equation 15 does not take atomic decoherence into account. An experimentally obtained optimum is thus found to be $2\,\mu s$. These parameters are used to obtain the experimental results presented in section 5.1.3. However, higher power levels were later wanted. In order to achieve greater power levels, I build an injection-locked laser which would mimic characteristics of a already existing laser beam but would provide greater power levels.

Exploiting a well known phenomena of oscillating systems, two oscillators can come to oscillate with identical frequency, by coupling via a mediating light field. In this case the relatively weak laser with a insufficient power level (master laser) is sent into a already lasing slave laser. In this system the master laser is shone into the slave laser diode with a bandwidth including which includes the wanted lasing frequency. The incoming master laser is furthermore beam shaped to match to spatial dimension of the slave lasers beam. It is now expected that the master lasers frequency will be amplified by the gain medium of the slave laser. If the amplified master intensity is larger than the natural modes of the slave laser intensity, the master laser will dominate the slave lasers emission. This emission will then inherit the master lasers frequency. The difference between the linewidth and maximum gain lasing wavelength, of the slave-diode which is not injection-locked and the slave-diode which is injection-locked, can be seen in figure 12. Here the dominating wavelength can be seen to move several nanometers. The dominant wavelength will lase with a given power level, determined by the slave diode. The slave-diode laser will only lase at a threshold current, which shown in figure 13. The achievable power level is limited by the maximum output power of the slave laser diode ($\sim 30\,mW$).

Thus the injection-locking scheme is inserted into the existing scheme and can be visualized in figure 14. In figure 14 the master laser light with $P = 2.7\,mW$ is injected into the slave laser diode through a series of wave-plates and lenses. In order to couple correctly the optical isolator (or Faraday isolator), the master laser beam must be sent through a $\lambda/2$-plate to match the polarization axis of the polarization beam splitters inside the optical isolator. Furthermore the spatial dimensions of the beam must not exceed the in-coupling hole of the isolator. The master light leaving the isolator is sent through a $\lambda/2$-plate and then again spatially manipulated in order to match the preferred intrinsic elliptical mode of the slave laser diode. The output elliptical light from the slave laser diode now passes through the same lenses, creating a circular Gaussian beam. Passing through

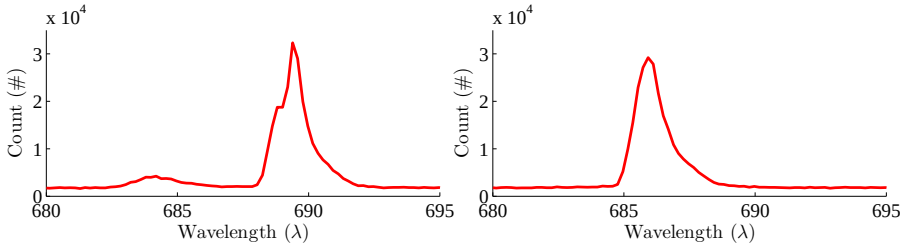

Figure 12: ***a)*** *Plot of the linewidth from the injection-locked laser diode. The first-axis shows the given wavelength and the second-axis shows the photon number count. The diode is injection locked by a laser with a desirable linewidth and central frequency. Thus an optimal injected slave laser inherent these properties. The linewidth is thus smaller compared to the non injection-locked diode and the center frequency is moved to the desired wavelength* $\lambda = 689\,\mathrm{nm}$. ***b)*** *Plot of the linewidth from the non-injection-locked laser diode. The first-axis shows the given wavelength and the second-axis shows the photon number count. The non-injection-locked diode is left to laser and is dominated by the internal gain medium with a broad linewidth. The dominate gain mode radiates at a wavelength* $\lambda = 686\,\mathrm{nm}$.

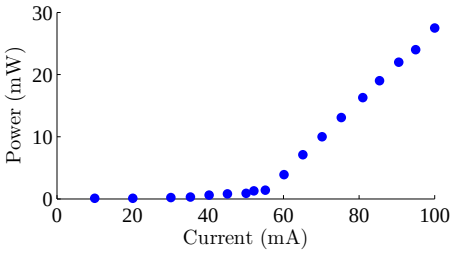

Figure 13: *Plot of the laser diodes output power as the diode current is varied. The diode laser is not injection-locked and will at threshold current of* $I_{diode} = 54\,\mathrm{mA}$ *start to lase. The injection-locked laser is expected to have a lower lasing threshold current as extra energy is provided through the master-lasers injection field.*

the $\lambda/2$-plate once more insures that output light from the slave laser matches the conditions that allows the light to pass through optical isolator, thus deviating from the incoming light of the master laser. This light is now sent through AOM_π in the same manner as previously described, but now with a power level of $P = 19.7\,mW$.

In order to ensure the optimal conditions of inheriting the master laser frequency, the internal cavity length of the slave laser diode can be manipulated to optimize conditions for the wanted frequency and suppress the natural frequencies of the slave laser diode. The internal cavity length is manipulated by controlling the temperature of the slave laser diode. Thus the amplification of the injected master laser

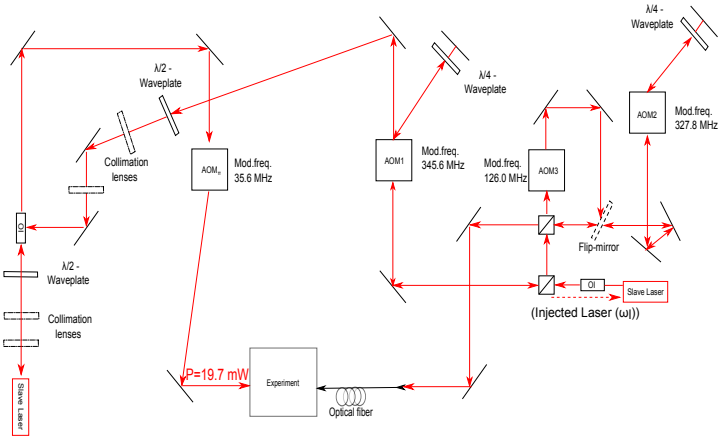

(a)

Figure 14: *Illustration similar to figure 10, but with an injection locked slave laser using the the* 0^{th} *order mode of AOM1. To obtain high transmission efficiency through the optical isolator (OI), the beam is collimated and given the correct polarization. Before reaching the slave laser diode the light is again shaped of rotated to meet the diodes internal cavity conditions. As the light leaves the diode, it is once more sent through collimation lenses and further rotated to fulfil the conditions of direct transmission through the OI. The light is frequency manipulated through* AOM_π *to match the atoms resonance condition, however with a power of* $\mathrm{P} = 19.7\,\mathrm{mW}$ *compared to figure 10.*

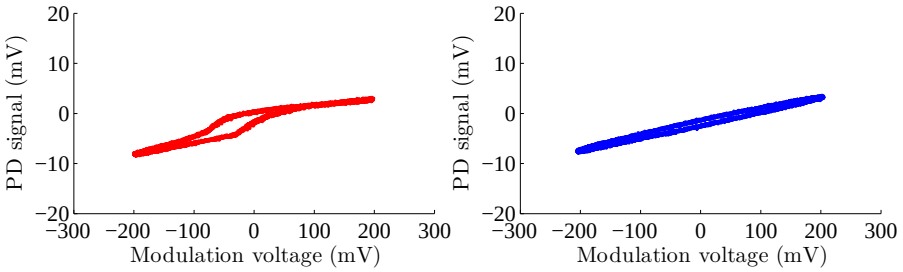

(a) (b)

Figure 15: *Plots of output power of the slave diode when injected (**a**)) and not injected (**b**)) by the frequency stabilized master laser. The first-axis show the output power and the second-axis axis show this modulation signal. The slave diode current was periodically modulated by an external modulation signal in order to detect output power stability levels. Hysteresis is observed during modulation of the injected laser, however the slave laser output was stable roughly over the entire flat plateau, when the laser current was kept constant. The slave laser was optimized with the parameters:* $\mathrm{I} = 86.67\,\mathrm{mA}$ *and* $\mathrm{T} = 25\,\mathrm{C}°$.

dominates the slave laser emission for a span of the slave diode current. Figure 15 shows transmitted slave laser output power when the slave laser current is modulated. A difference in the modulated power

level is observed between the injection-locked slave laser and the non-injection-locked slave laser. For the injection-locked power output, a flat plateau is observed which indicates that the gain medium of the slave laser is dominated by the master laser for the current span applied to the slave diode. A wide plateau is here desired which results in a stable lasing mode. In order to optimized the plateau a good overlap between the modes of the master -and slave laser is desired and optimal values for the current and temperature is needed. For an output power of $P = 19.7\,mW$ the optimal current and temperature are $I = 86.67\,mA$ and $T = 25\,^{\circ}C$.

In order to ensure an optimal overlap between the intra-cavity field, pulse-laser and the atoms, the atoms most be fixated to a optimal desired position. To understand how the atoms position are manipulated, an understanding of the $461\,nm$ laser used to access the ${}^1S_0 \leftrightarrow {}^1P_1$ cooling transition is given.

3.2.3 *The 461 nm laser*

In order to probe the atoms as described above, the atoms must first be cooled and trapped. Whiles the techniques used for cooling and trapping is described later in section 4, the $461\,nm$ laser used in this technique is described now.

When cooling and trapping the atoms is desired, the ${}^1S_0 \leftrightarrow {}^1P_1$ transition can be used, as seen in figure 6. Therefore, a laser emitting the resonant radiation of $\lambda = 461\,nm$ must be produced. In contrast to the other lasers mentioned in this work, the $\lambda = 461\,nm$ laser diode does not contain the desired frequency in the linewidth of the laser-diode of the ECDL, as lasing diodes with this frequency have only just become commercially available. In the light of this, this Master student was granted 30.000 DKK, as seen in appendix A, by the Siemens foundation in order to buy a blue diode, containing the $\lambda = 461\,nm$ in it's linewidth, with associated current -and temperature controls. However, the granted blue diode was is not was not implemented in any work associated with this dissertation. Instead the granted blue diode was injection-locked and used for power amplification in a second Strontium experiment at the Cold atoms group at the Nils Bohr Institute. The second experiment will be mentioned in section 6. However, in this work the desired frequency is obtain by frequency doubling of near infrared laser-diode with a center frequency of $\lambda = 922\,nm$. Only a brief mentioning of the frequency doubling technique will be given, as my work did not include the inner workings of the $\lambda = 461\,nm$ laser. For a thorough description of inner works of the $\lambda = 461\,nm$ laser used in this work, the reader is referred to [8].

Following [7], the general set-up consists of the $\lambda = 922\,nm$ diode in the Littrow ECDL configuration. The generated light is sent through

a Master Oscillator Power Amplifier (MOPA) which increases the power from $P = 17\,mW$ to $P = 800\,mW$. The power amplified light then enters a bow-tie cavity with a $LINiO_3$ crystal inside, producing the desired frequency doubled light of $\lambda = 461\,nm$.

The frequency doubling occurs as result of the light interacting with a material in a non-linear manner, taking advantages of the material's finite second-order non-linear susceptibility χ^2. The polarization (P(t)) of a material is given by the dipole moment per unit volume. Thus the motivation for using a MOPA, increasing the applied E-field (E(t)), is given. Also the bow-tie cavity will decrease the waist size of the light thus focusing the applied E-field into an even smaller volume of the $LINiO_3$ crystal. The polarization can be described by:

$$P(t) = \epsilon_0[\chi^{(1)}E(t) + \chi^{(2)}E^2(t) + \chi^{(3)}E^3(t) + ..], \tag{16}$$

where ϵ_0 is free space permittivity. In equation (16) the polarization is seen to scale as the n^{th} order power of the E-field.

Describing the inner dynamics of the crystals $\chi^{(2)}$, which lead to frequency doubling via three-wave mixing is required. Here two degenerated incident fields add up and excite the atoms in the crystal lattice, which then decays to a single output field with double frequency. Given a monochromatic incident field $E(t) = Ae^{-i\omega t} + c.c$ interacting with $\chi^{(2)}$ in the crystal, leads to a second-order polarization:

$$P^{(2)} = \epsilon_0\chi^{(2)}E^2(t) = 2\epsilon_0\chi^{(2)}AA^* + (\epsilon_0\chi^{(2)}A^2e^{-i2\omega t} + c.c). \tag{17}$$

As there is no time-dependent parameter in the first term in equation (17), it can simply be interpreted as a static field in the crystal. However the second term in equation (17) does have a time dependency. This term oscillates at 2ω and can be interpreted as a coherent light at twice the frequency of the incident field.

This process of frequency doubling however has a rather low efficiency. The external bow-tie cavity thus increase the efficiency of the conversion process by reflecting and keeping the infrared radiation inside the cavity, thus amplifying the infrared intra-cavity field by increasing the number of infrared photon interactions with the crystal. The cavity results in an intra-cavity power amplification of $P_{cavity} \propto \mathcal{F}P_{in}$, where $\mathcal{F}$ is the finesse and can be interpreted as the number of round trips the photon takes before leaving the cavity. The cavity mirrors are coated in such a manner, that whiles most of the infrared light is reflected and thereby staying inside the cavity, the majority of the frequency doubled blue light will be transmitted. The frequency doubling using a bow-tie cavity set-up has an output power of $\sim P_{out} = 70\,mW$, resulting in an efficiency of $\eta = 10\%$. As the frequency is doubled, so is the linewidth of the incident field. However the cooling transition is rather broad an thus the linewidth

doubling is not a problem.

As the $^1S_0$ state is not entirely decoupled from the triplet P-state, a scheme must be implemented to ensure the further decay to the ground state. This scheme is now treated.

3.2.4 *The 679 nm and 707 nm repumping lasers*

During the cooling process, the $^1S_0 \leftrightarrow {}^1P_1$ transition is exploited. Decay from the $^1P_1$ level to the long lived $^3P_2$ state can cause a decrease in the available number of atoms in the ground state. Therefore two so-called repumping lasers are implemented to ensure that the $^3P_2$ and $^3P_0$ states, can decay to the ground state via the $^3P_1$ level.

The two repumping laser are constructed using the Littman-Metcalf configuration, which are mounted on a monolitic mount. The monolitic mount is then temperature stabilized and the whole construction is then place in a metal box, to insure as little disturbance to the system as possible. Thus it was possible to adjust the lasing frequency to match the transition of the $^3S_1 \leftrightarrow {}^3P_2$ and $^3S_1 \leftrightarrow {}^3P_0$ repumping transitions. Implementing these two laser resulted in an 10 times increase of atoms in the ground state.

Focus will now be shifted towards utilizing the 461 nm laser. Here the experimental set-up and techniques used for cooling and trapping the atoms will be discussed.

4

EXPERIMENTAL SET-UP AND TECHNIQUES

A detailed explanation of the different stages of cooling and fixating the atoms is given. As the atoms are fixated, their temperature is determined and is related to atomic decoherence. Other sources of atomic decoherence is then treated. Here, a mechanical light shutter is implemented to reduce decoherence originating from remnant cooling light and the results are reported. Then the atom-cavity emission, hinted in section 3.2.1, is described and the relationship between the emission and the induced atomic phase is given. Having shown the how the atomic phase is related to the atom-cavity emission, a technique for signs of coherent emission is then implemented and investigated. Lastly, an experimental overview of the atom-cavity-laser set-up is given.

4.1 COOLING AND FIXATING THE ^{88}Sr ATOMS

An overview of the different stages that the ^{88}Sr atoms go through in our experiment, is now given. At first the ^{88}Sr atoms, being in a solid sate, are warmed up in an oven creating a gas state. The atoms then diffuse through a hole in the oven, creating a thermal beam with an initial velocity of 515 m/s. However, in order to take advantages of the narrow transitions of the $^1S_0 \leftrightarrow {}^3P_1$ transition, the atoms must be cooled down to a few millikelvin, thereby reducing the Doppler broadening of the transition which otherwise would result in a large decoherence. The cooling of the atoms can be achieved by exposing them to the two dimensional optical molasses lasers, insuring a velocity-compressed beam with only one dominating velocity component, thus primarily propagating in a desired direction. The radiation form the 461 nm laser is shone in the opposite direction of the atoms propagation direction resulting, thus exploiting the momentum that the photons carry. In order to make the thermal atomic beam resonant with the 461 nm laser light, a so-called Zeeman slower perturbs the atoms with a position dependent magnetic field, bringing the atoms into resonance. The atomic beam leaving the Zeeman slower now travels at an average speed of ~ 30 m/s in the desired direction. Lastly, the atoms are caught in a so-called Magneto-Optical Trap (MOT). The MOT reduces the atoms velocity to an average of ~ 1 m/s, corresponding to a temperature of only a few millikelvin. By using this cooling and fixating set-up the Doppler broadening is reduced and thus the decoherence is diminished.

Central to our cooling and fixating of the ^{88}Sr atoms, is the 461 nm laser beam (or cooling light). This is therefore described further

4.1.1 *Cooling light*

At first, natural Strontium is inserted into the oven, in its initial solid state form. After a vacuum has been created inside the oven, it is then heated from room temperature to a temperature of $T = 520\,C°$. The increase in temperature, results in an evaporation of the ^{88}Sr and thus a thermal cloud of ^{88}Sr is created. A beam of thermal atoms now diffuse from a 1.2 mm hole embedded into the oven. Due to the finite temperature of the thermal atomic cloud, the atoms diffusing from the oven hole have an average initial velocity, in the direction of the propagation axis (x'-axis). Here x' indicates an axis which lies at an 45° angel between the x-axis and y-axis, as shown in figure 19. The initial average velocity can be calculated using the kinetic theory of gasses:

$$\langle v_{x'} \rangle = \sqrt{\frac{9\pi}{8}} \sqrt{\frac{k_B T}{M}}. \tag{18}$$

When Boltzmann's constant (k_B), the atomic weight ($M = 88\,u$) of ^{88}Sr and the temperature (T) are inserted into equation (18), it reveals that $\langle v_{x'} \rangle = 515\,m/s$. In order to avoid Doppler broadening of the $^1S_0 \leftrightarrow {}^3P_1$ transition linewidth, the atomic beam must be slowed. To do so, a 461 nm laser beam of photons propagates in the opposite direction of that of the atoms (negative x'-direction), exploiting that the a single photon in the beam carries momentum $p = \hbar k$, where the wavenumber (k) is given by $k = \frac{2\pi}{\lambda}$. Thus the atoms absorb the photons' momentum, and by conservation of momentum, loss momentum in their direction of propagation. Following [7], the length required to bring the atoms to a full stop using the momentum of the cooling light is pursued.

A two-level atom, with a ground state $|g\rangle$ and an excited state $|e\rangle$ is considered. An atom carrying momentum ($p_{atom} = M\langle v_{x'} \rangle$) is initially in a ground state. The atom then absorbs a photon with momentum ($p = \hbar k$). According to conservation of momentum, the atom then has $p = p_{atom} - p_{photon}$. However, as $p_{photon} \ll p_{atom}$, a large number (~ 5000) of photons are needed in order to cancel out the initial momentum of the atom. To utilize the absorption of a large number of photons, a broad atomic transition with a fast decay rate is ideal. Using a broad transition line with a fast decay rate, will optimize the number of absorbed photons per second.
After absorbing a photon the atom, now in an excited state, spontaneously emits a photon. The spontaneously emitted photon is emitted in an arbitrary direction in the the 3-dimensional space, resulting in a change of the atoms momentum in an undesired direction. However,

the direction change arising from the spontaneously emitted photons, average to zero. Thus, only the momentum of the absorbed photons originating from the cooling light contribute, when averaging over the relevant time-of-flight time-scale. The result is a net scattering force acting on the atoms in the negative x'-direction [**10**]:

$$F_0 = \hbar k \gamma \rho_{ee} = \frac{\frac{1}{2}\hbar k \frac{I}{I_{sat}} \Gamma}{1 + \frac{I}{I_{sat}} + (\frac{2\delta}{\gamma})^2}, \tag{19}$$

where ρ_{ee} is the so-called probability density matrix element, the saturated intensity is $I_{sat} = \frac{\pi h c}{3}\frac{\gamma}{\lambda^3}$ and $\delta = \omega_l - \omega_a$ is the detuning of the laser with respect to the atomic transition. The $^1S_0 \rightarrow ^1P_1$ transition used to slow the atoms can be seen in figure 6 and has the decay rate $\Gamma/2\pi = 32\,\mathrm{MHz}$.

In order to translate the force from equation (19) into a stopping length, the case of zero detuning and high intensity ($I > I_{sat}$) is considered. The maximal force that can be obtained is thus $F_0^{max} = \frac{1}{2}\hbar k \Gamma$, leading to a maximal acceleration [**10**]:

$$a_{max} = \frac{F_0^{max}}{M} = \frac{\hbar k}{M}\frac{\gamma}{2}. \tag{20}$$

Here the recoil velocity can be identified as $v_r = \frac{\hbar k}{M} = 9.8 \times 10^{-3}\ \mathrm{m/s}$, and can be thought of as the atom at zero velocity absorbing a single photon. This translates into a minimum stopping length of [**10**]:

$$L_{min} = \frac{\langle v_{x'} \rangle^2}{2 a_{max}}. \tag{21}$$

Inserting the relevant values into equation (21) reveals a minimum stopping length $L_{min} = 0.13\,\mathrm{m}$. However, stopping the atoms with the maximum force results in an unstable slowing process. Therefore a rule of thumb is exert only half the maximum scattering force on the atoms $\frac{1}{2}F_0^{max}$, resulting in a stopping length twice as large.

The premise for stopping a maximal number of atoms, is requiring the atoms to move in a one dimensional beam with a velocity component primarily in the x'-direction and a minimal velocity component in the two transverse directions. However, large transverse velocity components may be present, resulting in a reduced number of atoms. Therefore a so-called optical molasses technique is used to diminish transverse velocity components is provided in the following section 4.1.2. As the atoms in this experiments already have a sufficiently low transverse velocity components, this technique is not implemented at the oven hole. A brief description of this technique is however presented now as the technique provides inside into the wanted atomic compression in velocity space and is used for implementing the MOT.

4.1.2 *2-dimensional optical molasses technique*

As the atoms diffuse from the oven hole as mentioned above, the atoms will have a primary velocity component $v_{x'}$, but may also have significant transverse Maxwell-Boltzmann distributed velocity component ($v_{z'}$,$v_{y'}$). The result of this is an undesirable deviation from the x'-axis, creating a cone-like shape of atoms diffusing from the oven hole as a function of the travelling time. As the atoms velocity components are diminished in the x'-axis the transverse velocity components become very significant for a later position dependent fixation. To reduce the transverse velocity components, the atoms can be met by two counter-propagating beams in each transverse direction, just as the atoms have diffused from the oven hole. In each transverse dimension, the counter-propagating beams will exert a total force F_{OM} on the atoms, given by [**11**]:

$$F_{OM} = -\alpha v = \hbar k \frac{\Gamma}{2} \frac{I}{I_0} \left(\frac{1}{1 + \left(\frac{2(\delta - kv)}{\Gamma} \right)^2} - \frac{1}{1 + \left(\frac{2(\delta + kv)}{\Gamma} \right)^2} \right). \tag{22}$$

Here α is the damping coefficient of the velocity (v), Γ is the resonance probing transition and δ is the detuning compared to the resonance probing transition. This equation holds true when the intensity is much smaller than the saturation intensity ($I \ll I_0$), thus avoiding saturation broadening from the counter-propagating beam. In the case where the atom has no transverse velocity component (and therefore no additional frequency component), the two terms in the parentheses in equation (22) exactly cancel each other. The result is a net force equal to zero, as can be seen in figure 16. However, if an atom does have a transverse velocity component, it will interact and be slowed by the laser beam radiating in the opposite propagation direction, compared the atoms transverse velocity component. The damping is proportional to the slope of the force curve at zero velocity.
Thus, optical molasses technique may reduces unwanted velocity components of the atoms and thus maximizes the atom density in the wanted velocity-space. However, to maximize the atom density in position-space, other techniques must be implemented as well.

4.1.3 *Zeeman slower*

Having maximized the atomic density into a 1-dimensional beam in velocity-space, the atoms are ready for cooling in the x'-direction before reaching the MOT. This is done with a so-called Zeeman slower which is depicted in figure 17. Due to the finite velocity ($v_{x'}$) of

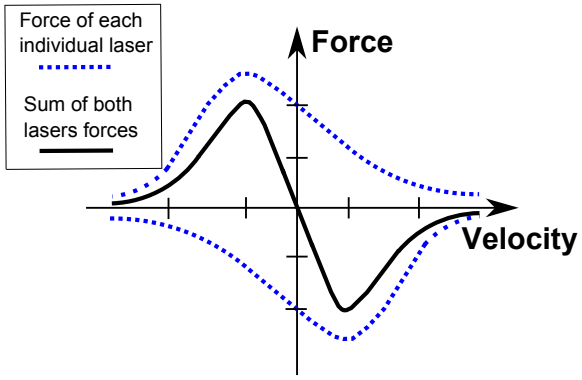

Figure 16: *Illustration of the force of the two counter-propagating lasers as a function of the velocity. The dotted blue lines represent the force of each laser in 1 dimension. The full black line is the force sum of both lasers in one dimension. The force-damping term α in equation 22 is proportional to the slope at $v = 0$.*

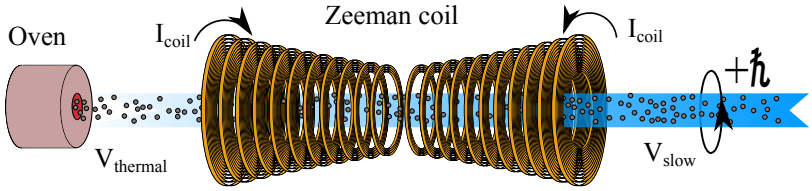

Figure 17: *Illustration of the schematics of a Zeeman slower. As atoms effuse from the oven hole, a beam of thermal hot atoms move with a large velocity $v_{thermal}$ propagating down through the Zeeman slower coils. The two halves of the coils have current running through them in opposite directions, which results in a field change from negative to positive. By implementing such a magnetic field configuration, all the atoms in a initial velocity distribution are brought into resonance at some point along the Zeeman slower axis. Atoms with an initial high velocity are brought into resonance early whereas atoms with initial low velocity are brought into resonance later, due to the gradually decline magnetic field strength. The Zeeman slower is constructed in such away that the atoms will have a non-zero velocity v_{slow} when exiting. The cooling light is tuned to be in resonance with the atoms at the halfway point where the current is reversed. Due to the same halfway reversal the magnetic field perturbation dictates that resonance with the atoms only be possible when using positive circular polarized light $\hbar$. Figure is adapted from [**20**].*

the atoms, the laboratory frame of reference resonant transition frequency (ω_0) is Doppler shifted by [**10**]:

$$\omega_D = \omega_0 - kv = \omega_0 \left(1 - \frac{v}{c}\right). \tag{23}$$

It is seen by examining equation (23), that the Doppler shift dependent on the atom velocity. The velocity of an ensemble of atoms in a single dimension, is described by the 1-dimensional Maxwell-Boltzmann distribution. However, a thermal beam diffused from an

oven hole will in general have a higher flux of atoms with a large velocity component in the propagation direction (x′-direction). A good description of the 1-dimensional velocity distribution is given by [**10**]:

$$f_{thermal}(v_{x'}) = \frac{v_{x'}^3}{2\tilde{v}^4} exp\left(-\frac{v_{x'}^2}{2\tilde{v}^2}\right), \tag{24}$$

where $\tilde{v} = \sqrt{\frac{3k_B T}{M}}$ is the most probable velocity, and $v_{x'}$ is the velocity of an atom moving in the x′-direction. However, the velocity of a atom changes as the atom interacts with the cooling light and thus so does the Doppler frequency shift.

In the case where no magnetic field perturbs the atoms ($B = 0$), the slowing of the atoms will be left to the force of the counter-propagating cooling beam. The velocity dependent force is given by [**12**]:

$$F = F_0 - \beta v_{x'}, \tag{25}$$

where β is the damping-coefficient of the velocity dependent term. The force is linearly proportional to the velocity and if the velocity-independent term ($F_0 = 0$) is neglected, the atoms would come to a full stop. However, if the velocity-independent term is not neglected ($F_0 \neq 0$) the atoms would still experience a force acting on them as they have come to a full stop and thus would begin to move in the negative x′-direction. This is undesirable.

As a position sensitive magnetic field ($B(x')$) perturbs the atoms, the result is a position dependent Zeeman shift of the atomic cooling transition, that cancels the atoms' Doppler shift, thus bringing the atoms into resonance with the cooling laser. In order for the cooling laser frequency (ω_l) to stay in resonance with the moving atoms with velocity v_x', the atomic resonance in the laboratory frame (ω_0) should be perturb by the position dependent magnetic field and follow the relation [**10**]:

$$\omega_0 + \frac{\mu_B B(x')}{\hbar} = \omega_l + kv, \tag{26}$$

where μ_B is the atomic magnetic moment. A desirable magnetic field profile can be obtained by applying a uniform magnetic field gradient along the x′-axis [**10**]:

$$B(x') = B_0\left(1 - \frac{x'}{x_0'}\right)^{1/2} + B_{bias}, \tag{27}$$

for $0 \leqslant x' \leqslant x_0'$. Here x_0' is the length of the coil and $B_0 = \frac{\hbar v_0}{\lambda \mu_B}$. If $\mu_B B_{bias} \simeq \hbar\omega - \hbar\omega_0$ and $\omega = \omega_0$ the atoms will come to a full stop at the end of the coils. It is instead beneficial to leave the atoms with a small velocity so that they can moved into the region of the MOT where the measurements of the atoms are performed. A configuration where the magnetic field drops to zero and is then reversed is

favourable as it gives the same decrease in velocity for a given change in B_0. Furthermore as this magnetic field configuration requires a smaller field magnitude, less current turns are needed and as the coils have current running in opposite directions compared to one another, the two fields tend produces less field at $x' > x'_0$. Also, this configuration creates a sharp cut-off in field magnitude. This sharp cut-off help the atoms leave the Zeeman slower cleanly, as the atoms see a sudden increase in detuning of the cooling light, which cuts the radiation force applied to them. Thus the atoms leave the Zeeman slower with a final velocity $v_f \approx 30\,m/s$. This technique insures that any atom with a velocity in between the initial -and final velocity will interact with the cooling laser at some position along the Zeeman slower and will thus be slowed.

The Zeeman effect caused by the applied magnetic field to the atoms, perturb them and results in Zeeman shift in energy [**10**]:

$$\Delta E_{ZE} = M_J g_J \mu_B B(x'). \tag{28}$$

Here the g-factor of the total angular momentum is $g_J = \frac{3}{2} + \frac{S(S+1)-L(L+1)}{2J(J+1)}$. For the $^1S_0 \rightarrow {}^1P_1$ transition in the $^{2S+1}L_{S+J}$ notation, it can be seen that as $\vec{S} = 0$ and $\vec{L} = \vec{J}$ revealing $g_J = 1$. For the ground state $^1S_0$, the projection of the total angular momentum $\vec{J}$, is seen to be $M_J = 0$. Inserting $M_J = 0$ into equation (28), shows no Zeeman energy shift. However, when considering the excited state $^1P_1$, $M_J = 0, \pm 1$. For $M_J = 0$, equation (28) again shows an unshifted level. For $M_J = \pm 1$, equation (28) shows a energy splitting, shifted by $\pm E_{ZE}$ compared to $M_J = 0$ of the excited state. The three levels of M_J correspond to different spin-orientations with respect to the quantization-axis (z-direction) given by the applied magnetic field. These levels can be talked to with different polarisations of the light. However, as the magnetic field is switch halfway through the Zeeman slower, resonance is only possible for positive circular polarized light, $(+\hbar)$, interacting with excited state. Thus by looking at figure 17, the cooling light will have a circular polarization corresponding to $^+\sigma$ for the left-most half of the Zeeman-slower, and $^-\sigma$ for the right-most half of the Zeeman slower.

The atoms are thus cooled enough to be compressed and fixated in at specific and desired position. This is done by applying a MOT.

4.1.4 *Magneto-Optical trap and temperature of atoms*

The MOT is created by combining the 3-dimensional optical molasses technique with a specific magnetic field configuration. Using the optical molasses technique ensures a velocity dependent restoring force, whiles combining it with a magnetic field ensures that the restoring force becomes position dependent as well. This method is used to cool the atoms into the milliekelvin regime and thereby minimizing

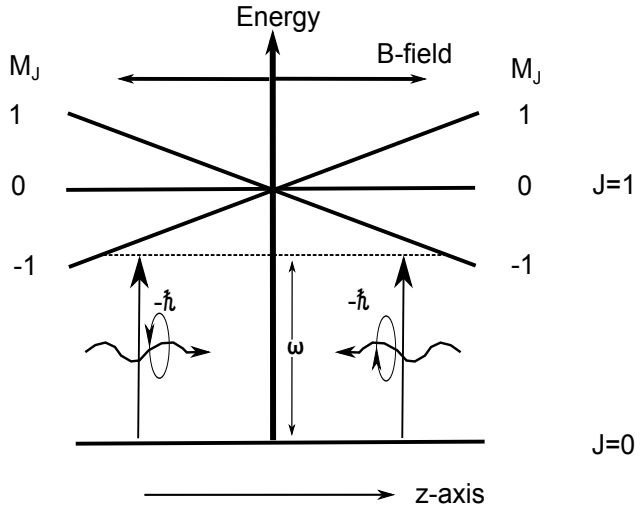

(a)

Figure 18: *Schematics of a 1-dimensional MOT which show an illustration of the energy level splitting for an atom with a* $J = 1$ *and* $J = 0$ *transition, as the magnetic field strength increases. As the atoms move away from* $z = 0$ *the magnetic field increases the Zeeman energy splitting, making the atoms resonant with the detuned cooling light. Electronic spin pointing in the same direction as the magnetic field will have a larger energy than opposite spin. Two counter-propagating cooling beams irradiate the atoms, with a negative circular polarization* $-\hbar$ *in order to access the* $M_J = -1$ *level.*

the effects of Doppler broadening on ${}^1S_0 \leftrightarrow {}^3P_1$ transition linewidth.

The magnetic field is produced by two coaxial coils in a anti-Helmholtz configuration, above one another in respect to the z-axis. By running current through the coils in counter-propagating directions, a field is creates which points out of the center of the coils in the z-direction, whiles simultaneously creating a uniform inward pointing field in the x-y-plane. As the field strength increases, so does the energy splitting of the ${}^1P_1$ state as was described in equation (28). This is easily visualized for the 1-dimensional case, as seen in figure 18. The atoms are furthermore exposed to radiation, using a 3-dimensional optical molasses technique. The radiation from the 3-dimensional optical molasses lasers are slightly detuned, resulting in a laser frequency slightly below the resonance of the $M_J = 0$ sub-level for the ${}^1P_1$ state. As the atoms move away from the center, the Zeeman effect splits the $M_J = 0$ sub-level, and the $M_J = -1$ sub-level becomes resonance with the slightly detuned cooling light. Thus, even if the atoms are stationary in a region of non-zero B-field, the magnetically induced energy shift results in a non-zero force, forcing the atoms back into the desired position at the MOT center. If the atoms has some finite velocity, they will experience a damping force, described in equation (22) via the lasers of the optical molasses technique. Keeping with the

1-dimensional picture in figure 18, the frequency shift can be incorporated into the description of the scattering force in equation (19) from [**10**]:

$$F_{MOT} = -\alpha v - \frac{\alpha\beta}{k} z. \tag{29}$$

This leads to a restoring force with an additional term $\frac{\alpha\beta}{k} z$ acting as a spring constant, with $\beta = \frac{g_J \mu_B}{\hbar} \frac{dB}{dz}$. As the atomic $^1P_1$ energy level is split, the cooling light must also have a specific polarisation in order to access the different sub-energy levels of J. In the case of $z > 0$, the lowest laying energy level is $M_J = -1$. As the cooling light frequency is slightly detuned, this is the desired level to access. This transition requires a light with σ^-, achieved with handedness $-\hbar$, to be excited. In the case of $x, y > 0$, the lowest laying energy level is $M_J = -1$. This transition requires a light with σ^-, achieved with handedness $+\hbar$, to be excited. In this manner, an atomic cloud can be form, as both the atomic density in position -and velocity space can be controlled. Combing all the above features, result in figure 19.

After the atoms have been confined, their temperature is measured. Atoms with high temperature have a larger Doppler broadening which translate in to atomic decoherence. The lower limit temperature of Doppler cooled atoms (T_D) follows [**10**]:

$$T_D = \frac{\hbar\Gamma}{2k_B}. \tag{30}$$

Here the cooling transition linewidth (Γ) dictates the lower limit of the temperature. In principle, by implementing a MOT using laser probing a narrow linewidth, compared to the broad cooling linewidth 32 MHz, a further cooling of the atoms could be achieved. This is however not implemented in the work of this dissertation. T_D merely gives a lower limit of the atoms temperature using optical molasses. To find the true temperature of the atoms would reveal the level of decoherence originating from the Doppler broadening. As I was co-supervisor on a project group in the Cold-atoms group at the Nils Bohr Institute, a numerical simulation predicting the atom temperature was developed in cooperation with the authors of paper [**13**]. The simulation is based on measuring the fluorescence emitted by irradiated atoms. It is thought that by turning off the MOT the atoms will diffuse away from the center of the trap, escaping at a rate dependent on the atoms temperature. As the atoms' propagate away from the center of the trap, the fluorescence levels are expected to be reduced just as the MOT is switched on again. Thus by comparing the numerical simulation to actual measurements of reduced fluorescence, an average temperature of the atoms can be given.

The simulation initially considers at a group of atoms caught in a MOT. The density of atoms are normally distributed in the 3-dimensional

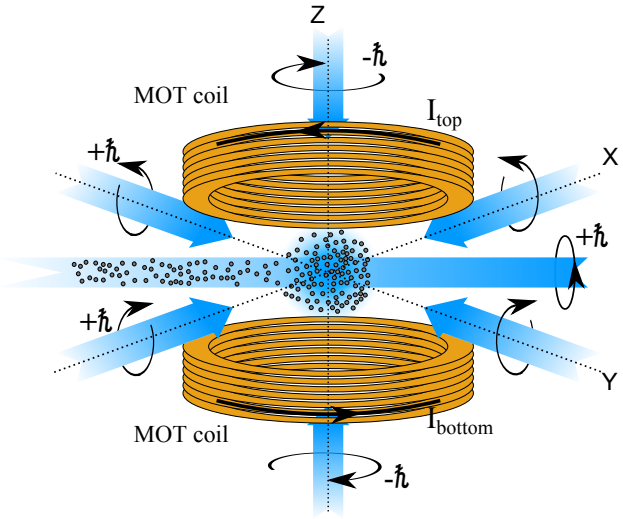

(a)

Figure 19: *Illustration of a 3-dimensional MOT. The 3-dimensional MOT is a combination of a 3-dimensional optical molasses technique with a specific magnetic field configuration. 3 pairs of counter-propagating beam irradiate and cool the atoms in each of the three directions (x,y,z). The two coils with current running through them in opposite directions, creates a magnetic field in opposite direction. The constructed magnetic field has field lines exiting at the center of each coil in the z-axis , whiles simultaneously creating a uniform inwards pointing field in the x-y-plane. At the center of between the coils, the magnetic field is zero. A the atoms move away from the center, the magnetic field configuration shifts the $M_J = -1$ to lower energies in all directions, thus bringing the atoms into resonance with the cooling lasers. The handedness of the relevant cooling beams are depicted in the figure and all are chosen so that all the beams have σ^- polarization. Figure is adapted from [**20**].*

space, with a common standard deviation, σ_x. The atoms also have an initial velocity distribution in each direction in the 3-dimensional space, obeying a Maxwell-Boltzmann distribution with standard deviation $\sigma_v = \sqrt{\frac{k_B T}{M}}$. Furthermore, the cooling lasers in all three dimensions are said to have an intensity which is also Gaussian distributed with a standard deviation σ_I. For a rigorous explanation of these parameters, the reader is referred Appendix B. Now the correct question to ask is how much the intensity level is reduced compared to the normalized initial intensity level, as a function of duration of cooling light switch-off time. This is a good question to ask, as the intensity of the fluorescent light is proportional to the intensity of the cooling lights. Thus the following relation was developed:

$$\left\langle \frac{I(t)}{I(0)} \right\rangle = \frac{1}{1 + (bt)^2}, \tag{31}$$

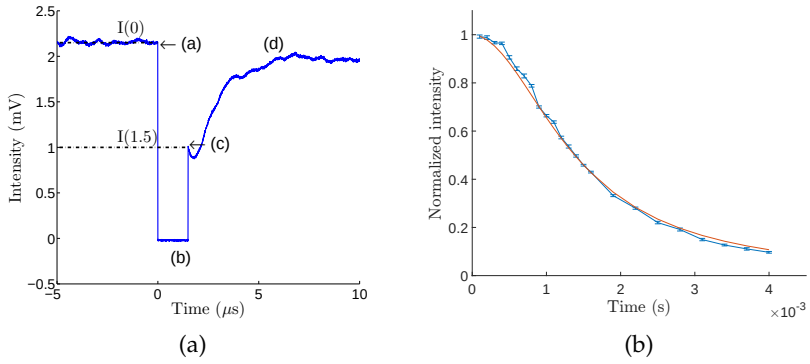

(a) (b)

Figure 20: ***a)*** *An experimental cycle showing the various steps in obtaining intensity data via fluorescent atoms. The figure shows 4 steps. At (a), the lasers are turned off, stopping the fluorescence during the off-time interval (b), shown here for* $\tau_{off} = 1.5\,\mathrm{ms}$. *At (c) the lasers are turned back on, causing the atoms to emit light again. (d) is the start of the recharging period of the atom cloud, which was about 800 ms long in total.* ***b)*** *Plot of the relative intensity, as a function of the off-time. The red curve is a fit the model of equation (31) , with b as a fitting parameter. The fit has a reduced* $\chi^2 = 4.2$.

where $b = \frac{\sigma_v}{\sqrt{\sigma_I^2+\sigma_x^2}}$. Thus if σ_v, σ_x and σ_I are found, one can isolated the temperature, revealing:

$$T = \frac{M}{k_B} b^2(\sigma_I^2 + \sigma_x^2). \tag{32}$$

In order to determine the standard deviation of the light intensity of the 3 dimensional optical molasses lasers, one of the lasers were aimed at a CCD-camera which was linked to a computer, revealing $\sigma_I = 1.83\,\mathrm{mm} \pm 0.03\,\mathrm{mm}$. The accuracy of this parameter is very important (as will be see later on), as it enter in equation (32) quadratically.

To obtain measurements, the following experimental procedure was done. First a pulse-generator was initially set to provide an overall sequence time duration of 800 ms, followed by a varying pulse duration (0.1 ms to 4 ms) in which the cooling lasers were switch off. The pulse-generator was then coupled to an AOM, allowing cooling light to reach the experiment as seen in figure 19. The overall sequence of 800 ms was initially chosen so that a steady state in the MOT fluorescence level could be reached. The discrete durations of the switch-off times were varied and as the cooling lights were switched on again, the immediate intensity level was recorded. The sequence was repeated obtaining data point representing 8 averages, to collect better statistics.

In figure 20 a, the fluorescence response of a typical cycle is shown. Step (a) shows the initial fluorescence level and (b) indicates the off-

time of the cooling lasers. (c) is the measurement of MOT fluorescence level just as the lights are turned back on. The following dip seen at a time-scale of sub-microseconds after (c), indicates that a fraction of the atoms escape the MOT as the restoring force is inadequate to push atoms with a large velocity, back. However, shortly after the MOT fluorescence level rises again due to the arrival of new atoms and the old ones being forced back into the center of the MOT. (d) indicates the start of this process, proceeding until a steady fluorescence level state is obtain once more. Recording (c) for various durations of (b), reveals a correlation between the relative intensity and off-time for the cooling lasers. In figure 20 b, this correlation is seen. Here the blue points indicate reduced normalized intensity data as a function of time and the red line is the fit with fitting parameter b, from equation (31). The fit has a $\chi^2 = 4.2$ which indicates acceptable overlap between data and fit. The temperature (T) from this fit is found to be $T = 16.7\,\mathrm{mK} \pm 0.6\,\mathrm{mK}$. A temperature that high would result in a very large Doppler broadening, creating a large decoherence contribution. A temperature this high would mean that Γ_{decoh} would dominate and would most likely extinguish any collective coherent coupling in the atom-cavity system, as described in section 2.3. Results from section 5 would thus not be possible. Therefore an error is thus most likely suspected as the cause of the high temperature. The temperature dependency of σ_I is, as mentioned previously, quadratic. I suspect a missing factor of 2, here. If true, this would decrease the temperature with a factor of 4, moving the temperature to much more acceptable level which also are consistent with previous estimations of the average temperature of the atoms, in [8].

As the atoms have been cooled and trapped to a specific location with an optimal overlap with the intra-cavity field, the atom-cavity system is now treated.

4.1.5 *Optical cavity*

The atoms trapped by the MOT are fixated to a position in space, that ensures an optimal overlap between the number of atoms that couple to the continuous intra-cavity field. In this work, the optical cavity placed around the atoms, serves not as a frequency discriminator, but as a method to increase the effective light-atom interaction length.

An optical cavity is consists of a spacer and two mirrors. At the end of the spacer, two mirrors at a specific distance opposite to each other are glued on. Cavity resonant radiation is then shone through the cavity mirror, creating a continuous standing field inside the cavity (intra-cavity field). In optical resonators the wavelength is of the order $\sim \mu m$, which is small compared to the resonators length and thus any diffraction effects are negligible. This is an advantage since the cavity need not be confined in all three dimensions, but rather

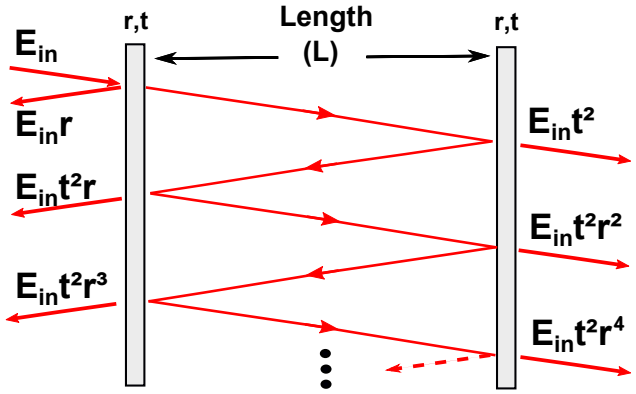

Figure 21: *Schematics of an empty Fabry-Perot interferometer/cavity. A given initial field (E_{in}) enters perpendicular to the cavity mirror. As E_{in} meets the mirror surface, the field will be partly reflected and partly transmitted, the fraction is dependent on the values of r and t. Once inside the cavity, an infinite number of reflective and transmitted terms give rise to a converging power of both intra-cavity field and the outgoing field leaking through the cavity mirror. Due to energy conservation, the output power must be equal to the input power, whereas the intra-cavity field power is significantly increased. The intra-cavity field power level is determined by the reflectivity of the cavity mirror.*

by two reflecting mirrors. Due to the mirrors low transmission and high reflectivity, a photon within the intra-cavity field will take many found trips, before being transmitted. As a small fraction of the cavity field leaks from the mirrors it is collected and used for signal detection. A variety of cavity configurations exist, however the Fabry-pérot interferometer (FPI) is the cavity configuration used for probing the atoms in this experiment and is therefore explained further. This is best done by visualizing the transmitted field, which can be seen in figure 21 and is described by following [1] and [7]. The initial E-field (E_{in}) travels in a parallel direction to the surface of the mirror. The E-field meets the mirror, resulting in a reflected and transmitted E-field, given by $E_{in}r$ and $E_{in}t$, respectively. Here t is the mirrors transmission amplitude coefficient and r is the reflective amplitude coefficient. The transmitted part of the initial wave enters the cavity and meets the atomic ensemble (not illustrated in figure 21) and obtain a phase shift (θ_a) before reaching the second mirror. At the second mirror the field is again partly transmitted and partly reflected. As this process repeats itself, an infinite number of transmitted terms constitute the total transmitted E-field from the second mirror:

$$E_{out} = E_{in} T e^{i(\theta_c+\theta_a)}(1 + Re^{i2(\theta_r+\theta_c+\theta_a)} + R^2 e^{i4(\theta_r+\theta_c+\theta_a)} + ...), \tag{33}$$

where $T = t^2$ and $R = r^2$ are the intensity transmission and reflection coefficients, respectively. θ_r is phase shift obtained by the reflection

off the mirror surface, θ_a is the complex phase obtained from the atomic interaction and θ_c is the phase obtained from the cavity length and materials. Exploiting that the infinite sum of terms in equation (33) converges and can then be rewritten to:

$$E_{out} = E_{in} \frac{T e^{i(\theta_c+\theta_a)}}{1 - R e^{i2(\theta_r+\theta_c+\theta_a)}}. \tag{34}$$

In order to reduce the expression of E_{out} further, a consideration toward the values of differently obtained phases is given. A condition for an intra-cavity field is a standing wave, that undergoes a round trip phase shift corresponding to an integer number of 2π. This condition will only be fulfilled for certain resonance frequencies and certain spatial mode dimensions of the radiation. An optical cavity with fixed dimensions can thus be used as a frequency discriminator. Given a phase shift of $\theta_r = \pi$ from each reflection of a mirror and inserting this $\theta_r = \pi$ into $e^{i2\theta_r}$, equals 1 and can thus be ignored for all further purposes. The phase shift introduced by the cavity length can be described as $\theta_c(\omega) = \frac{\omega}{c} L$, where L is the cavity vacuum length. Combining the phase shifts $\theta_c(\omega)$ and $\theta_a(\omega)$ into $\beta = \theta_c(\omega) + \theta_a(\omega)$, the reduced form of the transmitted field can be written as:

$$E_{out} = E_{in} \frac{T e^{i\beta}}{1 - R e^{2i\beta}}. \tag{35}$$

As only a certain number of resonant frequencies create standing waves in the FPI, the so-called Free Spectral Range (FSR) is discussed. The FSR describes the frequency spacing between two resonance frequencies of the same transverse mode of an optical cavity and is given by [1]:

$$FSR = \frac{c}{2nL}, \tag{36}$$

where c is the speed of light in vacuum, n is refractive index inside the cavity and L is the length of the cavity. Our experimental set-up has FSR = 781.14 MHz, [8]. Another parameter often associated with a cavity is the so-called Finesse. The Finesse is measure of how many round trips a photon in the cavity field makes before leaving the cavity, and is given by [1]:

$$\mathcal{F} = \frac{FSR}{\delta\nu_c}, \tag{37}$$

where $\delta\nu_c$ is the resonance cavity linewidth. Our experimental set-up achieves $\mathcal{F} = 1500 \pm 50$, where $\delta\nu_c = 520$ MHz [8]. Equation (37) thus infers that a high finesse will come at the cost of a narrow resonant cavity linewidth. For a bad-cavity regime ($\Gamma \ll \delta\nu_c$) a narrow resonant cavity linewidth is not desirable. However, if a large light-atom interaction length is wanted, the cavity finesse must not be too small.

Thus a trade-off is often required in order to obtain a sufficient value of both the large cavity linewidth and a large finesse.

As seen in equation (34), the ensemble of atoms induce a phase on the emitted light. Searching for coherence in the emission field, translates into a search of a collective atom induced phase shift. Therefore, a technique for detection of coherent light was implemented in our system.

4.2 DETECTION OF COHERENT LIGHT

Determining the level of coherence in the observed collective flash emission, reported in section 5, is an important feature in distinguishing between different collective emission types. If the atoms' dipole are coupled in the atomic ensemble the atoms may decay as a collective and emit coherent light. To determine if coherent light from the collective atomic ensemble emission is present, a demodulation signal is needed. As previously described in section 4.1.5, it is expected that the cavity field interacting with the atomic ensemble will result in a phase shift in the measured output emission fro the atom-cavity field. Here, an explanation of the method used to obtain the demodulated signal is given following [8]. For a rigorous mathematical explanation, the reader is referred to [7].

To measure the phase shift induced by atomic ensemble, the heterodyne detection technique can be exploited [1]. This technique can be used to measure the relative phase difference between the cavity field interacting with the atomic ensemble and the cavity field not interacting with the atomic ensemble. However, this technique is associated with a large noise in the spectral area. Therefore in an attempt to reduce the noise, frequency modulation is used in the form of the so-called Noise Immune Cavity Enhanced Optical Heterodyne Molecular Spectroscopy (NICE-OHMS) technique. This dissertation will however limit itself to a description of optical heterodyne detection, as this technique is sufficient in describing the obtained coherent light results in section 5.

The initial field entering the cavity is phase modulated with a Electro Optical Modulator with frequency Ω, in order to create sidebands in respect to the initial carrier with frequency ω, amplitude A and initial phase ϕ. This results in a input cavity field with a carrier on resonance with the atomic transition and two sidebands frequency shifted one FSR ($\omega \pm 2\pi\Omega$) away from the carrier, thus still being resonant with the cavity but no longer resonant with the atomic transition. The relation of the different involved spectra are illustrated in figure 22. Thus the noise introduced to both the carrier and the sidebands and can be cancelled out upon detection of a so-called beat-signal, leaving only the atomic induced noise. The output atom-cavity field

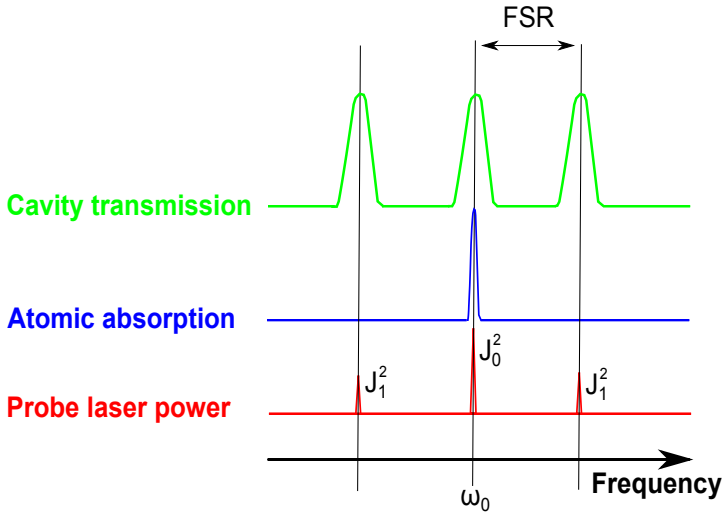

(a)

Figure 22: *Illustration of the spectral overview of the NICE-OHMS technique (Not to scale). Three relevant linewidths are mentioned here. The cavity transmission is shown to have a broad linewidth thus making it insensitive to small variations of the probing laser. The probing laser it passed through an Electrical Optical Modulator (EOM) in order to create small sidebands located one FSR away from the carrier, which is resonant with the atomic transition. The sidebands are resonance with the cavity, but not in resonance with the atomic transition. Thus the sidebands experience all the same noise as the carrier, except the noise originating from the atoms. The noise from the sidebands can then be deducted from the noise on carrier upon detection of the beat-signal.*

is then ready to be demodulated to a DC level. The output atom-cavity field can thus be described by [1]:

$$E_{out} = E_0(j(x)e^{-\alpha}e^{i(\omega t+\phi_a+\phi_c)} + J_1(x)e^{(\omega+\Omega)t+i\phi_c} - J_1(x)e^{(\omega-\Omega)t+i\phi_c}). \tag{38}$$

Here $J_i(x)$ refers to the i'th order regular Bessel function. The Bessel function describe the amount of power originally located in the carrier, transferred to the i'th order sideband when modulated by an EOM with modulation index x. Here only the first two sidebands are included. The first term in equation (39) corresponds to the probe carrier. This term includes the atomic absorption $e^{-\alpha}$ and a phase shift ϕ_a induced by the atomic ensemble. All terms experience a common phase shift of the cavity ϕ_c originating from propagation in an empty optical cavity. After the cavity field has interacted with the atoms, the field leaks out through the cavity mirror and the signal is measured

on a photo-diode. Cancelling the common cavity phase ϕ_c, the measured signal-current of the photo-detector will be proportional to:

$$\begin{aligned} S_{PD} \propto E_0^2(e^{-2\alpha}J_0(x)^2 + 2J_1(x)^2) \\ + J_0(x)J_1(x)e^{-\alpha}(e^{i\phi_a} - e^{-i\phi_a})(e^{i\Omega t} - e^{-i\Omega t}) \\ - J_1(x)^2(e^{2i\Omega t} - e^{-2i\Omega t}). \end{aligned} \tag{39}$$

The first line in equation (40) is a just a static component, the second line has a component oscillating with Ω, whiles the third line has a component oscillating with 2Ω. Using a appropriate bandpass filter in the detection set-up, will eliminate the first and third line in equation (40), thus leaving the second line with the Ω oscillating component. The remaining component is now mixed with a local oscillator with a sinusoidal signal $\sin(\Omega t) = \frac{1}{2}(e^{i\Omega t} - e^{-i\Omega t})$ and is thus demodulated to a DC-signal:

$$S_\Omega \propto 4J_0(x)J_1(x)e^{-\alpha}\sin(\phi_a). \tag{40}$$

For very small collective atomic induced phase shift ($1 \gg \phi_a$), the demodulated signal can be approximated to $S_\Omega \propto \phi_a$. The demodulation technique will provide a DC signal proportional to the phase induced shift of the atoms, thus providing a clear indication of coherent light emission.

Coherent light emission can be only be obtained if all processes contributing to atomic decoherence are diminished. In locating possible sources of atomic decoherence, the cooling laser used for the Zeeman-slower and the cooling lasers used for the MOT, were investigated.

4.2.1 *Mechanical shutter*

An effort to diminish any remnant cooling light contributing to atomic decoherence, was made. Having a finite amount of cooling light reaching the atoms at a post-cooling stage can result in additional atomic decoherence ($\Gamma_{furhter}$), adding to the already exciting decoherence ($\Gamma_{doppler}$) given by the atoms finite velocity. This results in a combined decoherence expression $\Gamma_{decoh}^2 = \Gamma_{doppler}^2 + \Gamma_{furhter}^2$ of the atoms [**12**]. The decoherence $\Gamma_{furhter}$ arises due to the cooling light driving the ${}^1S_0 \leftrightarrow {}^1P_1$ transition whiles simultaneously trying to probe the atoms with the ${}^1S_0 \leftrightarrow {}^3P_1$ transition. These two transitions have different decay times and are completely out of phase with one another. Thus every time the atoms reaches the ground state via the cooling transition, they must become in phase with rest of the atoms being probed by the ${}^1S_0 \leftrightarrow {}^3P_1$ transition, in order to emit light coherently. These out of phase atoms will thus add decoherently whiles trying to become in-phase with the atoms already being probed via the ${}^1S_0 \leftrightarrow {}^3P_1$ transition.

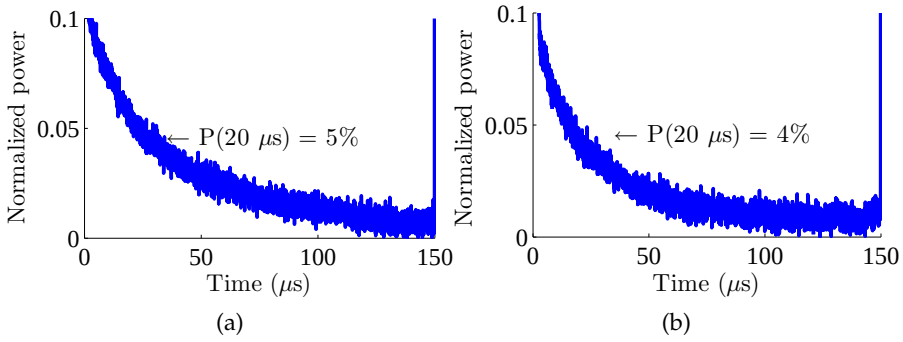

Figure 23: ***a)*** *Plot show the light intensity decay time of a MOT-arm in the x-axis, as the Acoustic Optical Modulator (AOM) controlling the passage of light, is turn off using a TTL-signal. The first-axis shows time after the TTL-signal has reached the AOM. The second-axis show the power level, normalized to the initial power level. After* 20 µs *a remnant power of* 5 % *is still present, corresponding to an remnant intensity of* 0.19 µ*W.* ***b)*** *Plot show the light intensity decay time of the Zeeman-arm in the x'-axis, as the Acoustic Optical Modulator (AOM) controlling the passage of light, is turn off using a TTL-signal. The first-axis shows time after the TTL-signal has reached the AOM. The second-axis show the power level, normalized to the initial power level. After* 20 µs *a remnant power of* 4 % *is still present, corresponding to an remnant intensity of* 0.64 µ*W.*

In order to determine the amount of cooling light power reaching the atoms as the probing transition begins (20 µs after), a photo diode was place in the Zeeman-arm and in a single MOT-arm in the x-axis. A normalized measurement of the remnant power as a function of off-time was then measured and its results are shown in figure 23. The two plots of 23 show the remnant afterglow of the cooling light travelling through an AOM. After 20 µs cooling light can still be detected at atomic ensembles position. The two plots show cooling light of $\sim 5\,\%$ of the initial level for the MOT arm in figure 23 a and $\sim 4\,\%$ of the initial level for the Zeeman arm in figure 23 b, still reaches the atomic ensemble. The initial power-level is given by the amount of power used to cool the atoms and is 3.8 m*W* for the measured MOT arm in the x-axis and 16.1 m*W* for the Zeeman arm. Thus after 20 µs, 0.19 m*W* still reaches the atoms via the MOT arm and 0.64 m*W* still reaches the atoms via the Zeeman arm. The contribution to the total decoherence is not estimated in this dissertation, instead non-zero power level serves as motivation for implementing a remnant cooling light elimination scheme.

To counteract the non-zero power of the cooling lasers reaching the atomic ensemble, a mechanical light shutter was proposed and inserted directly in front off the AOM controlling the shut-time of the cooling lights. The mechanical light shutter would thus stop all

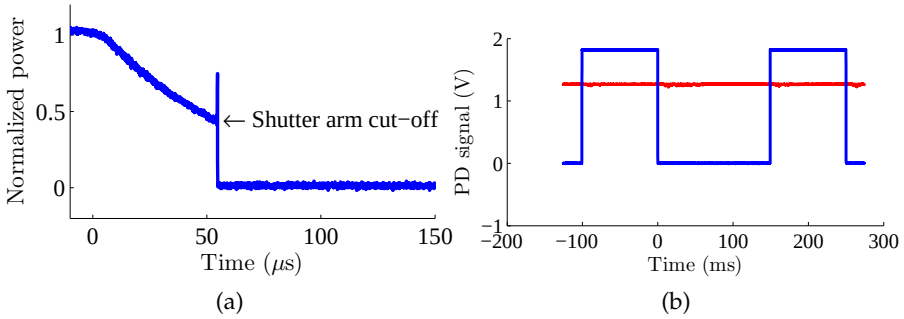

Figure 24: ***a)*** *Plot shows the effects of a mechanical shutter place in front of a continuous beam. From* $t = 0$ *to* $t = 55\,\mu s$ *the shutter arm partly blocks the continuous laser field. At* $t = 55\,\mu s$ *the continuous beam is completely covered by the shutter arm and the intensity falls to zero. Due to vibrations, a optimal positioning between the beam area and shutter arm could not be maintained.* ***b)*** *Plot shows the cooling field mediated from the bow-tie cavity (red) and the shutter arm sequence as a function of time. Due to mechanical vibrations, the bow-tie cavity experienced noise resulting in a periodic intensity dip of* 4 % *compared to the initial intensity level, over a period of* 70 ms.

remnant light, by inserting a mechanical arm in front of the beam. A already build mechanical light shutter was inserted, consisting of a electromagnetic coil exerting a force on an piece of metal with a piece of paper glue to it, acting as the arm. The paper arm was initially chosen due to the relative light weight. Initial measurements on the mechanical shutter were performed in order to determine the shut-time stability. Several measurements where performed and jitter was observed whiles operating the shutter at two different time scales. At $t < 10\,s$ the shutter arm was observed to deviate less than $40\,\mu s$ from the set shut time. At $t > 10\,s$ the shutter am was observed to deviate up to $160\,\mu s$ from the set shut time.

Further measurements on the shutter arm were performed in order to determine the amount of time needed to completely cut off the light. However, due to the lack of stiffness in the paper arm the shut times varied and were very sensitive to vibrations exerted by the movement of the arm cause by the electromagnetic coil. Furthermore, these shutter arm induced vibrations spread via the optical table and into the sensitive bow-tie cavity systems. Whiles shut times on average were $\sim 10\,\mu s$, movement caused by vibrations could result in shut times of $\sim 300\,\mu s$. The bow-tie cavity locked cooling laser mentioned in section 3.2.3, was however disturbed to a point that the cavity stabilizing feedback system keeping that cavity on resonance with the cooling light, could not function.

By implementing a vibrational absorbing mount and reducing noise originating from the shutter, attempts to optimized the shutter arm was made. However, this attempt to optimize was not successful. As

seen in figure 24 a, the result was that the shutter arm blocked part of the light at $t = 0\,\mu s$ to $t = 55\,\mu s$ and then at $t = 55\,\mu s$ finally succeeding in blocking all the light. This can be explained if the laser beam hits the very edge of the paper arm, causing only some partial blocking of the light until $t = 55\,\mu s$. The shut time at $t = 55\,\mu s$ is at $< 1\,\mu s$. If the paper arm was placed in such a manner, that the cooling light hit the paper arm further in, the cut-off time was prolonged to unacceptable time scales. Figure 24 b, shows the reduced noise on the doubling cavity of the cooling laser. Even with the optimized arm, fluctuations in the cavity mirrors can be indirectly observed through the output power fluctuations. The cavity mirror vibrations thus result in a power dip of 4 % over a time period of 70 ms.

Due to the nature of the shutter arms material, further usages of the optimized mechanical shutter still meant a realignment was necessary several times a day. Combined with induced vibrations at the cavity mirrors meant that the shutter arm was deemed unreliable and to unstable. Therefore the shutter arm set-up was not implemented for further use. A simple replacement of the paper arm was not done, as the light weight arm was crucial for the fast low inertia of this mechanical shutter arm. Building a new shutter was thus the only solution. However due to the time consumption of building a new shutter arm, this project was left for future students.

After an attempt to diminish atom decoherence further, measurements of the collective emission was pursued. A brief description of the combined atom-cavity-pulse-laser system is her given in order to visualize the core of the experiment used to obtain collective emission measurement.

4.3 COMBINING THE ATOM-CAVITY-PULSE SYSTEM

After the atoms have been cooled using the Zeeman slower, they are trapped in a MOT. The atoms are trapped in a specific region so that they lie within the optical cavity, with an optimal coupling to the intra-cavity field. A standing field in the optical cavity is then turned on, continuously probing the atoms at the ${}^1S_0 \leftrightarrow {}^1P_1$ transition, thereby acting as a mediating field between the atoms and the cavity mode. Further more the pulse-laser probes the atoms at an 45° angle in the x-y-plane, compared to the standing cavity field. This results in a combined atom-cavity-pulse system which is illustated in figure 25. Thus an investigation of collective spontaneous emissions are presented, that may occur within the boundaries of our system.

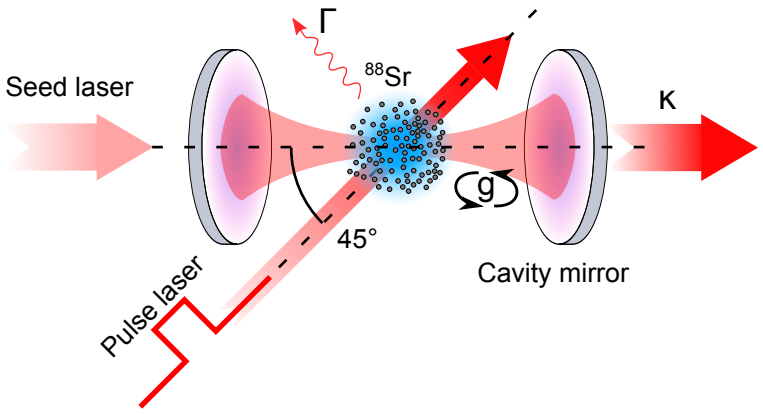

Figure 25: *Experimental set-up for active lasing.* $88^{S}r$ *atoms are trapped in a magneto optical trap (MOT) and cooled to* $T = 5\,mK$. *Atoms may couple via the resonant cavity field enhancing collective effects. An intra-cavity field laser tuned to the* $^1S_0 \leftrightarrow {}^1P_1$ *transition is constantly present and a second laser provides a pulse from the side. Modified from Appendix C.*

5

COLLECTIVE SPONTANEOUS EMISSION

In this section an investigation of collective spontaneous emission in our system is reported. Firstly, theoretical outlinings of Super radiance (SR), Super florescence (SF) and Amplified Spontaneous Emission (ASE) are presented, by defining different time regimes and different characteristics associated with collective emission. Secondly, a report of a numerical approach is given. Here, a simulation describing the time evolution of a system nearly identical to ours is given. Different parameters related to the three collective emission types are considered, indicating which of the three collective emission types that may be detected in our experimental set-up. Lastly, an experimental report is given. Here, the characteristic parameters' experimental dependencies are investigated, thereby distinguishing the three different types of collective emission from one another. Finally, a discussion and a conclusion is given. By comparing the experimentally obtained collective emission signal to the theoretical outlinings and the numerical simulation, a classification of the experimentally obtained collective emission is given.

5.1 THEORETICAL OUTLINE OF SUPER RADIANCE, SUPER FLUORESCENCE AND AMPLIFIED SPONTANEOUS EMISSION

A theoretical outlining of Super radiance (SR), Super florescence (SF) and Amplified Spontaneous Emission (ASE) is now given.

In 1954, Dicke [**14**] first purposed that a sample of two-level atoms prepared in a collective coherent state via an external source, may give cause to an enhanced radiative decay for a microscopic sample of dipoles locked in phase to each other. This process is known as SR. The linewidth of the emitted SR radiation is dominated by the atomic linewidth, in this case the ultra-narrow linewidth $^1S_0 \rightarrow {}^3P_1$ of ^{88}Sr.

Another similar type of collective coherent emission is called SF. Here an external source initially inverts the atomic population which initially consists of uncorrelated dipoles. The dipole phases may synchronize via a mediating field arising from spontaneous emission, resulting in a correlated coherent state. Thus after a characteristic delay time τ_D [**15**], the system builds up coherence [**16**]. After τ_D, the system is similar to SR, as coherent light is collectively emitted. A common feature for SR and SF is the coherent damped oscillation the dipoles experience, after the initial burst of coherent light is emitted. This can be understood by considering an initially inverted population on a Bloch sphere. After a initial burst of coherent light is

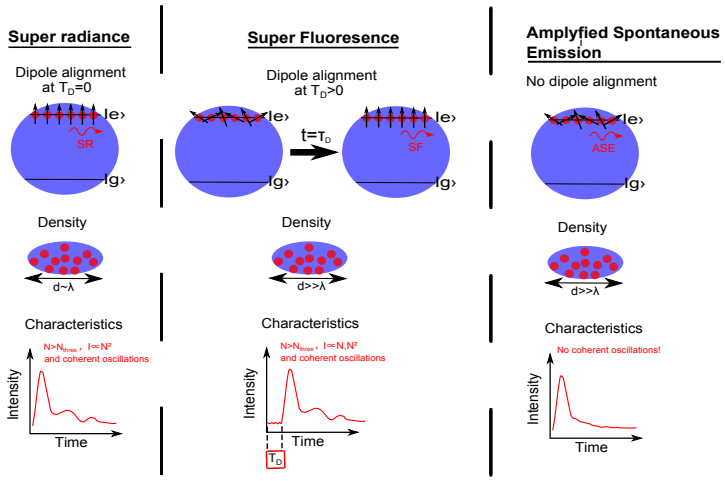

Figure 26: *Illustration of super radiance (SR), super fluorescence (SF) and amplified spontaneous emission (ASE) in a two-level system. At the top of this figure, a depiction of the relative dipole alignment is shown. In the middle, atomic density requirements are shown. At the bottom, the expected transmission signal is shown and relevant characteristic for the different collective emissions are given.*

emitted, the Bloch vector seeks towards and preforms a damp oscillation around the south pole of the Bloch sphere. This is realized as a ringing-effect after the initial collective coherent light has been emitted.

Lastly, amplified incoherent spontaneous radiation can be emitted from the dipoles of the inverted population. Here the amplification of the spontaneous radiation is causes by stimulated emission. Considering the incoherence of the emitted radiation, no ringing effect are expected to follow the initial emitted radiation. Furthermore, as the dipoles do not align, no delay time is expected either. However, some coherence may occur if the maximum gain mode outmatches the decoherent modes arising from spontaneous emission.

The three different regimes are depicted in figure 26. At the top of this figure, the coupling between the dipoles in the excited state are depicted for the three different phenomena. In order to distinguish the three types of collective emission from one another, relevant time scales and light characteristics of each collective emission type must be examined. Here, the relevant characteristics are: the expected flash intensity scaling as a function of the atom number, the presents of coherent oscillations, characteristic times for the system and lower a bound on number of atoms required to participate for collective emission for occur.

5.1.1 *Relevant characteristics*

To distinguish between the different types of collective emission, the flash intensity is investigated. The flash intensity for SR scales as N^2, where N is the number of excited atoms. SF initially, begins as spontaneous emission with intensity proportional N, but as the dipoles phase lock to one another, the intensity rapidly scales as N^2 and becomes analogous to that of the predicted SR intensity. However, it is possible for SF to exist in rather unfavourable conditions where decoherence is larger. In this case, flash intensities have been reported to scale as N [17]. If ASE is the cause of the flash, the intensity scales as N.

Whiles SR can be distinguishes from SF and ASE, by the necessity of an external source mediating a field to ensure coherence, the difference between SF and ASE can not solely be determined by the flash intensity. For this an examination of a coherent light ringing after the initial flash is needed. However as characteristics such as the flash intensity and coherence may be similar in SF and ASE, a further investigation of the characteristic time scales is necessary.

Different time scales are use to characterize the emitted radiation [17]. The radiative coupling time, τ_R, describes the characteristic time scale in which spontaneously emitted photons are coupled into the cavity mode.

$$\tau_R = \frac{1}{C_0 N_{Cav} \Gamma}, \tag{41}$$

here C_0 is the single atom cooperativity mentioned in section 2.3, N_{Cav} is the number of atoms emitting into the cavity mode and Γ is the spontaneous decay rate of the probing transition. The radiative coupling time describes the time over which coherence builds up among the emitters. However decoherence may occur in the form of Doppler broadening or from the presence of an external radiation fields driving a different transition in the atom, as described in section 4.2.1. If decoherence is described by a characteristic time scale T_2, then SF can only exist in the limit where $\tau_R \leqslant T_2$. Inserting this limit into (41), yields a threshold number of atoms necessary, all of which must emit into the cavity mode:

$$N_{threshold} = \frac{1}{C_0 T_2 \Gamma}. \tag{42}$$

Thus the lower limit is proportional to $\frac{1}{T_2} = \Gamma_{decoh}$. When calculating $N_{threshold}$, the value of C_0 must first be calculated. From section 2.3 equation (9), a calculation of $C_0 = 6.4 \times 10^{-4}$ can be obtained for our system, where the natural line width is $\Gamma/2\pi = 7.5\,\text{kHz}$ for the probing transition and the cavity linewidth is $\kappa/2\pi = 520\,\text{MHz}$. The main contribution to Γ_{decoh} is given by the temperature of the atoms.

In order to calculate the Γ_{decoh} the Doppler width must be found. The Doppler width (FWHM) can be described by [**10**]:

$$\delta\nu_D = 2\frac{\nu_0}{c}\sqrt{\frac{2k_B T}{m}\ln 2}. \tag{43}$$

An average temperature between 5 mK and 16 mK of the atoms reveals a Doppler broadening of the atoms of $\Gamma_{decoh}/2\pi = 1.1 \times 10^6$ Hz and $\Gamma_{decoh}/2\pi = 3.8 \times 10^6$ Hz, for 5 mK and 16.7 mK, respectively. Using the experimentally obtained temperatures 5 mK and 16 mK, the calculated threshold number of atoms required to participate with a photon into the cavity field, are $N_{threshold} = 2.3 \times 10^5$ and $N_{threshold} = 7.9 \times 10^5$, respectively.

Another system characteristic time, is the light propagation time:

$$\tau_E = \frac{l}{c}, \tag{44}$$

where l is the length of the medium of emitters and c is the speed of light. It should here be noted that the system that I have work with, has an optical cavity inserted around the emitters, thereby changing the effective light-atom interaction length. To achieve a modified expression of τ_E, the cavity must be taken into account. This modification is however not included in this dissertation.
Relating the propagation time to the radiative coupling time, all emitted photons can stimulated all atoms if $\tau_E < \tau_R$. This pure SF regime manifests itself by showing a flash intensity proportional to N^2. However if $\tau_E > \tau_R$, the emitted photons only stimulate some fraction of the atoms and a pure SF regime is no longer the case. In this case the flash intensity is proportional to N [**17**].

The time delay (τ_D), which is the time in which the dipoles lock in phase to each other and align, is another feature expected only for SF. Theoretical predictions for the time delay have been shown to be proportional to 1/N [**17**], where N is number of emitters. However it should again be noted that this prediction is for a non-cavity case and therefore corrections to this proportionality are most likely needed.

Lastly, initially uncorrelated incoherent emitters may emit a flash with a primarily coherent part [**18**] if the decoherence time is larger than the square root of the product of the radiative time and the delay time $T_2 > \sqrt{\tau_R \tau_D}$. However if the inequality if reversed ($T_2 < \sqrt{\tau_R \tau_D}$), incoherent radiation will dominate. This inequality can be used to distinguish between SF, which is expected to emit a coherent radiative flash, and ASE which is expected to emit a incoherent radiative flash.

Using the characteristic time scales for our experimental set-up reveals $\tau_R \approx 3.3\,ns$ and $\tau_D \approx 500\,ns$ [**8**], reveals $\sqrt{\tau_R \tau_D} \approx 40\,ns$ and $T_2 = 1/\Gamma_{doppler} \approx 260\,ns$, for 5 mK. This is within the regime of SF, but only just as a factor of 7 separates from the transition regime ($T_2 \approx \sqrt{\tau_R \tau_D}$).

The experimental parameters reveal that collective emission in the form of SF, can occur in our system. However, as parts of the theoretical outlining lack the inclusion of an optical cavity in their calculations, a numerical approach is furthermore taken.

In achieving a deeper understanding of collective emission that may appear in our system, a numerical approach is taken. The numerical approach is based on the Jaynes-Cummings model of a atom-cavity interaction, but also includes our systems pulsed laser and a continuous intra-cavity field. A closer theoretical investigation of the equation of motion for the number of photons and the cavity field are found and simulated. This is done to a much greater extend in [**19**], which this dissertation does not aim to fulfil as I primarily dealt with the experimental work reported in chapter 5. Instead, a overview of the theoretical considerations is given in an effort to reach the equations of motion describing the system evolution, thus being able to simulate the equations of motion. The equations of motion are derived from a master equation and a Hamiltonian characterising our system. Using these equations of motion, a numerical simulation predicting collective coherent emission in our system is performed and reported.

5.1.2 *Theoretical considerations and the simulation process*

This section seeks to derive equations of motion for the atoms and the cavity field for our system described in section 4.3. The approach is based on deriving a master equation, containing all system dynamics is given by the time evolution of the density-matrix elements:

$$\dot{\hat{\rho}} = \frac{i}{\hbar}[\hat{H}, \hat{\rho}] + \mathcal{L}_\Gamma[\hat{\rho}] + \mathcal{L}_\kappa[\hat{\rho}]. \tag{45}$$

Here the system dynamics of the atom-cavity interaction, seed laser and the pulsed-laser originate from the system Hamiltonian ($\hat{H}$).The spontaneous atomic decay and the cavity field decay dynamics originate from the Liouvilian terms $\mathcal{L}_\Gamma[\hat{\rho}]$ and $\mathcal{L}_\kappa[\hat{\rho}]$, respectively. The task is now to find relevant expectation values of our system given by using $\dot{O} = Tr\{O\dot{\hat{\rho}}\}$. In simulating our system, the expectation values of interest are the cavity field annihilator operator $a = \langle\hat{a}\rangle$, the atomic population $\sigma_z = \langle\hat{\sigma_z}\rangle$ and atomic coherence $\sigma_- = \langle\hat{\sigma_-}\rangle$. Since our experimental system only measures the intensity of cavity transmitted light, the expectation value of the cavity photon number $n = \langle\hat{a}\rangle = \langle\hat{a}^\dagger\hat{a}\rangle$ is also investigated.

The system Hamiltonian is given by:

$$\hat{H} = \hat{H}_{Cavity} + \hat{H}_{Atom} + \hat{H}_{Interaction} + \hat{H}_{Seed} + \hat{H}_\pi. \tag{46}$$

Here, the three first terms constitute the traditional Jaynes-Cummings Hamiltonian. The Jaynes-Cummings model is a theoretical description of a two-level atom interacting with a intra-cavity field mode,

and is ideal for describing the dynamics of our systems atom-cavity interaction. Inserting the full Hamiltonian into equation (45), calculations of the commutator relation between creation operators ($\hat{a}^\dagger$), annihilation operators ($\hat{a}$) and the system Hamiltonian ($\hat{H}$), the time evolution for the slowly varying field operator ($A = e^{i\omega_c t}a$) and the number of photons (n) are found, where ω_c is the cavity mode frequency. Likewise, calculating commutator relation between creation operators, annihilation operators, atomic population inversion operator ($\sigma_\pm$) and atomic transition operators (σ_z), the time evolution of the slowly varying atomic population inversion operators ($S_z^{(i)} = \sigma_z^{(i)}$) and the slowly varying atomic transition operator ($S_-^{(i)} = e^{i\omega_c t}\sigma_-^{(i)}$) are found. The thorough reader wanting a rigorous examination of the commutation relations, is referred to **[19]**. By including the dissipation terms found by calculating the Liouvilian terms equation (45), the equation of motion for the system are found to be:

$$\dot{A} = -i\sum_{i=1}^{N_a} g^{(i)}S_-^{(i)} - \frac{i}{2}\eta - \frac{\kappa}{2}A, \tag{47}$$

$$\dot{n} = -i\sum_{i=1}^{N_a} g^{(i)}(AS_+^{(i)} - A^\dagger S_-^{(i)}) + \frac{i\eta}{2}(A - A^\dagger) - \kappa n, \tag{48}$$

$$\dot{S}_-^{(i)} = ig^{(i)}AS_z^{(i)} + i\Delta S_-^{(i)} + \frac{i}{2}\Omega S_z^{(i)}e^{i\mathbf{k}\cdot\mathbf{r}^{(i)}} - \frac{\Gamma}{2}S_-^{(i)}, \tag{49}$$

$$\dot{S}_z^{(i)} = 2ig(A^\dagger S_-^{(i)} - AS_+^{(i)}) + i\Omega(e^{-i\mathbf{k}\cdot\mathbf{r}^{(i)}}S_-^{(i)} - e^{i\mathbf{k}\cdot\mathbf{r}^{(i)}}S_+^{(i)}) \tag{50}$$
$$-\Gamma(S_z^{(i)} + 1).$$

Here, N_a is the number of atoms, κ is the cavity decay rate, Γ is the natural decay rate of the atomic transition, Δ is the detuning between the pulse-laser angular frequency (ω_π) and the atom angular frequency (ω_a), Ω is the Rabi frequency, k is the pulsed-lasers wave vector, $r^{(i)}$ is the position of the i^{th} atom and $\eta = \sqrt{\frac{P_{in}\kappa}{E_{photon}}}$ is the classical driving amplitude, with P_{in} being the input power of the cavity and E_{photon} the energy of a photon. $g^i = g_0 \cdot \cos(k_c z)exp\left(\frac{-r^2}{\omega_0}\right)$ denotes the dipole interaction describing the coupling between the atoms and cavity mode, where the wave number of the cavity mode is $k_c = \frac{2\pi}{c\omega_c}$, z and r are the longitudinal and radial positions of the atom and ω_0 is the waist radius of the Gaussian cavity mode. $g_0 = \frac{d}{\hbar}\sqrt{\frac{\hbar\omega_0}{2\varepsilon V}}$ is the vacuum Rabi frequency, where d is the dipole moment and $\sqrt{\frac{\hbar\omega_0}{2\varepsilon V}}$ is the field strength per atoms.

In calculating equations (47) to (50), an 0^{th} order approximation was done by factorizing the expectation values involving two operators $\langle\hat{a}\hat{\sigma}_-^{(i)}\rangle \simeq a \cdot \sigma_-^{(i)}$. A consequence of this is that a perfectly excited atom in a cavity void of photons cannot decay spontaneously into the intra-cavity field mode.

Equation (47) to (50) can be integrated numerically. For a system of N_a atoms the system can be described by using $2N_a + 2$ coupled equations. As the atoms time evolution only couple via the cavity field, the time required to simulate a single time step scales as N_a. However, in our experimental system $N_a = 2 \times 10^7$ atoms, thus a rescaling is required to avoid prolonged simulation time. Therefore the atoms are split into $N_g = 10^4$ velocity groups, where atoms may share the same initial position and velocity coordinates. The initial positions of the atoms are spread out over a much wider area than a wavelength, which as seen in figure 26 is a condition for SF. In order to create conditions that are similar to those of the actual experiment, the simulation is allowed to evolve for 100 µs before the pulse-laser is initiated. The pulse-laser delay is inserted in the simulation in order to create a new steady state of the transmission intensity, arising from the AC-Stark shift created in our experiment by the simultaneous presence of the cooling light and the intra-cavity field. The AC-stark shift is implemented by initially detuning the intra-cavity field so that it is off-resonance with the atoms in the steady state solution.

Simulating equations (47) to (50), will thus give an indication of how our system will evolve. The results of the numerical approach is now reported.

5.1.3 *Simulation results*

The purpose of the simulation results is to substantiate the likelihood of the collective coherent emission being super fluorescence, as indicated in section 5.1.1. Therefore the flash intensity and the threshold number of atoms are not investigated in this simulation. Instead the flash delay time and the presence of atomic coherence are investigated in this simulation. A given flash delay time, would further support the suspicion of an SF-like emission in our system. Indications of a coherent light build up would likewise support this suspicion. For further analysis of simulation results, the reader is referred to [**19**].

A single realization of the evolution of the cavity photon number and the atomic coherence build up of the atom-cavity system is simulated and the results are shown in figure 27. Here the expected evolution of the emission power and atomic coherence is presented. The emission power is calculated from the cavity photon number and the atomic coherence is the magnitude of S_- projected onto the sign of g, resulting in $\mathrm{coherence} = \mid \Sigma_i S_z^{(i)} \cdot \mathrm{sign}(g^{(i)}) \mid$. The parameters used to achieve the numerical simulation results were equal to the experimental parameters in our system. The pulse duration applied to the atoms was set to $\tau_{pulse} = 284\,\mathrm{ns}$. The pulse duration time was first calculated to be optimal at $\tau_{pulse} = 280\,\mathrm{ns}$ and later optimized to $\tau_{pulse} = 284\,\mathrm{ns}$ by an experimental procedure. The pulse duration was calculated by using (15), for the power optimized injection-

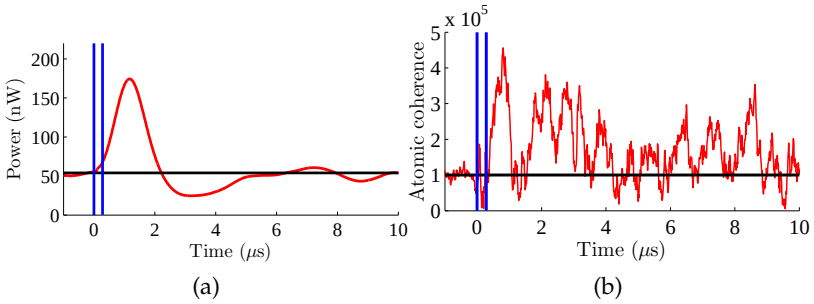

Figure 27: ***a)*** *Simulated transmission power (number of cavity photons) (red) after a pulse-laser (blue) of duration* $\tau_{pulse} = 284\,ns$ *was applied to the atoms. The system was allowed to evolve for* $100\,\mu s$ *before reaching a steady state at* $t = 0\,\mu s$. *The figure was obtained using experimentally found values:* $T = 5\,mK$, $N_a = 2 \times 10^7$ *atoms*, $N_g = 10^4$, $dt = 1\,ns$, $P_{in} = 100\,nW$ *and* $\Omega = 33.2\,MHz$. ***b)*** *Simulated atomic coherence (red) after a pulse-laser (blue) of duration* $\tau_{pulse} = 284\,ns$ *was applied to the atoms. Here coherence is defined as* $|\ \Sigma_i S_z^{(i)} \cdot \mathrm{sign}(g^{(i)})\ |$. *The system was allowed to evolve for* $100\,\mu s$ *before reaching a steady state at* $t = 0\,\mu s$. *The figure was obtained using experimentally found values:* $T = 5\,mK$, $N_a = 2 \times 10^7$ *atoms*, $N_g = 10^4$, $dt = 1\,ns$, $P_{in} = 100\,nW$ *and* $\Omega = 33.2\,MHz$.

locked laser of section 3.2.2. Other experimentally found values are the temperature $T = 5\,mK$, the number of intra-cavity field atoms $N_a = 2 \times 10^7$ atoms, the simulation time-steps $dt = 1\,ns$, the intra-cavity field power $P_{in} = 100\,nW$ and the initially detune cavity field $\Omega = 33.2\,MHz$.

Figure 27 a, shows a flash occurring $1\,\mu s$ after the pulse-laser was applied to the atoms. In order to find the decay time of the flash, a Lorentzian distribution is fitted (not shown here) onto the flash. The fit shows a characteristic decay time of $\sim 3\,\mu s$. The flash decay time is thus much smaller than the natural decay time $\Gamma = 22\,\mu s$ for the $^1S_0 \rightarrow {}^3P_1$ transition, indicating a different cause. The power level of the flash peak reached $140\,nW$ and is a factor of 4-5 larger than what will be presented in the experimental investigation in section 5.1.3. $2\,\mu s$ after the applied pulsed-laser, the power level drops to the initial level of the intra-cavity field, as seen before the pulse-laser is applied. Dampened oscillation around the initial intra-cavity field power level can be seen, hinting some coherence after the initial flash. To verify if the dampened oscillations indeed contain coherent light, a plot of atomic coherence build up is shown in figure 27 b, at the same time as the flash occurs. Here, coherence can clearly been seen building up during the build-up of intra-cavity photons. Even though some level of coherence does seem to coincide with the damped oscillations, the clarity of this is not as convincing.

Thus the numerical approach indicates a SF-like flash occurring

$\sim 1\,\mu s$ after the pulsed-laser is applied. Further more a coherent light build up is indicated as the pulsed-laser is applied to the atoms. Experimental considerations are now given and results of an experimental investigation are reported.

Common for all the collective emission types investigated here, is the need for an excitation of the atomic ensemble. Consider the ensemble in terms of a Bloch sphere, with a Bloch vector indicating a superposition of all the atoms being in the ground state and in an excited state of a two-level atom. An resonant monochromatic π-pulse is needed to invert the population from the ground state (south pole on the Bloch sphere) to an excited state (north pole on the Bloch sphere). For estimating the number of exited atoms in the atomic ensemble, a simple quantified time-dependent excitation population is given by [**10**]:

$$P_e = \sin^2\left(\frac{\Omega_{Rabi}t}{2}\right), \tag{51}$$

where $\Omega_{Rabi} = \Gamma\sqrt{I/2I_0}$ is the Rabi frequency for the resonant monochromatic radiation in regards to the atomic transition. Ω_{Rabi} is given by the transition linewidth (Γ), the saturation intensity (I_0) and the probing intensity (I). However if the applied π-pulse is not resonant with the probing transition, a frequency detuning term (Δ) has to be taken into account. The primary source of detuning in our system is due to the Doppler shift of the atoms. In velocity terms the Doppler shift reveals a detuning term given by $\Delta = kv$, where v is the atomic velocity component in the cavity relevant x-y-plane. Knowing that the atoms' velocities are represented by a Maxwell-Boltzmann distribution ($f(v)$), it is now possible to rewrite the simple time-dependent excitation population, taken the velocity detuning parameter into account:

$$P_{e,doppler} = \int_{-\infty}^{\infty}\left(\frac{\Omega_{Rabi}^2}{\Omega_{Rabi}^2+\Delta^2}\right)\sin^2\left(\frac{\sqrt{\Omega_{Rabi}^2+\Delta^2}t}{2}\right)f(v)dv. \tag{52}$$

The detuning term now introduced in equation (52), appears in the denominator of the fraction in front of $\sin^2$-term. Thus if the Δ takes a non-zero value, the excited population will always be below that of the simple resonant case as seen in equation (51). Executing equation (52) reveals an maximum expected excitation percentages of $P_{e,doppler} \approx 60\,\%$. The saturation effects from the intra-cavity field on the atoms is however not included in the calculation of (52) and its effect on the atoms is not trivial. An atom-cavity interaction is obtained if the atoms are located outside the nodes of the intra-cavity field. Due to the large degree of saturation, the atoms located outside the intra-cavity fields nodes can be thought, in terms of the Bloch sphere, as

having a their dipole vector smeared out across the equator. As a pulse-laser is applied to these atoms outside the nodes of the intra-cavity field, no change in the dipole-vector will occur. However the atoms located within the intra-cavity field mode nodes, will initially not interact with the cavity field and thus be located at the Bloch spheres south pole. These atoms will however be inverted in the case of an applied pulse-laser of the correct duration. Including such a consideration lowers the amount of excited atoms overlapping with the intra-cavity field, compared to the predicted 60 %. The excitation percentages of the atoms in overlap with the cavity mode, is now investigated experimentally.

In the ideal case of equation (51), the ensemble can be completely inverted by the π-pulse when the pulse length fulfils $t_\pi = \pi/\Omega_{Rabi}$. As the experimental set-up allows a more accessible control of the π-pulse length in contrast to the π-pulse probing power, a optimal pulse length can be found by fulfilling:

$$P = \frac{2I_0\pi^2 A}{\Gamma^2 t_\pi^2}. \tag{53}$$

In equation (53), A, is the π-pulse cross section. In the experimental set-up, different variations of the cross-section were inserted in order to find the optimal overlap with the ensemble emitting into the cavity mode. A optimum was found by considering flash maxima with $A = 1.19\,mm^2$. Is should here be noted that all experimental data was obtained using the initial pulse-laser set-up seen in 10. Only later was the power optimized pulse-laser set-up seen in 14, applied to our system. However, other assignments in the laboratory prevented me in retake all the experimentally obtained data again with the injection-locked laser. Therefore the pulse-laser power used to obtain the experimental investigations was $P = 3.8\,mW$. The transition linewidth $\Gamma = 7.5\,kHz$ and saturation intensity $I_0 = 3\,\mu W/cm^2$. Thus the optimal π-pulse length, in the ideal case was $t_\pi = 1.8\,\mu s$. However, due to decoherence in form of finite temperature, Doppler broadening must be taken into account. Therefore an optimal pulse duration time was experimentally found to be $t_\pi = 2\,\mu s$.

In order to investigate the ensemble excitation level predictions of (52) via the total florescences level, the off-time duration of the cooling lasers central to the experiment were manipulated. Firstly, the initially present radiation field of the 461 nm cooling laser, was turned off for a period of 40 μs. Hereby, the emission of the atomic ensemble being cooled by probing the $^1S_0 \rightarrow {}^1P_1$ transition and being probed by the intra-cavity field found a new steady state value. Then, the pulse-laser with various duration lengths was switched on. It was however required that all of pulse-laser duration ended 2 μs before the cooling lasers were turned on again. Also a on-resonance $689\,nm$ cavity-probe laser was left on during the entire sequence. The time-sequence for the combination of the lasers can be visualized in figure

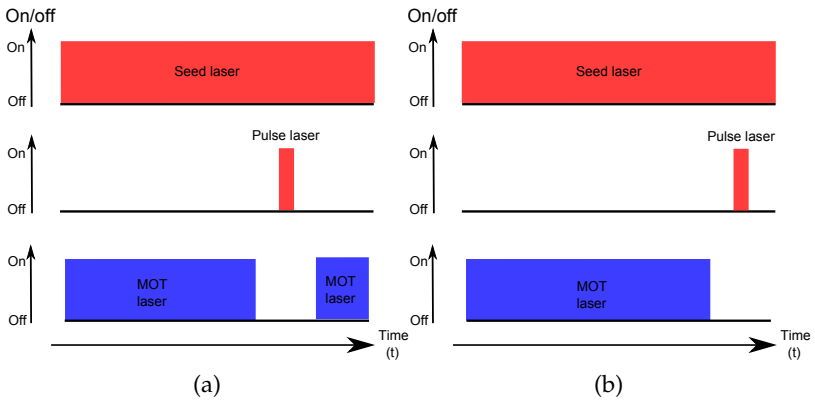

Figure 28: ***a)*** *Illustration of the sequence for the relevant lasers in testing the amount of excited atoms shown in figure 29.* ***b)*** *Illustration of the sequence for the relevant lasers for investigating of collective emission flash in this work.*

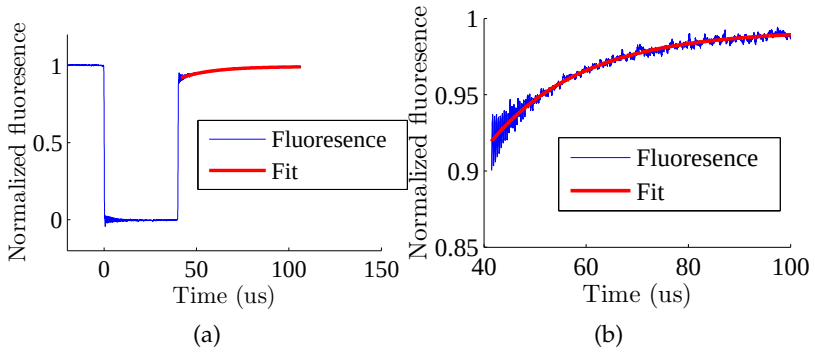

Figure 29: *Plots of the MOT fluorescence before and after a fraction of the laser cooled ^{88}Sr atoms were excited by a resonant pulse-laser. The blue line is the experimental data, while the red line is a theoretical fit. The fluorescence reduction was only around 10 % to 15 %. A zoom of the reduced fluorescence is shown i* ***b)****. The theoretical fit reveals a decay time of ~ 22 µs, corresponding with the natural decay time of the $^1S_0 \leftrightarrow {}^3P_1$ transition.*

28 b.

To identify the number of atoms excited by the pulse-laser, a measurement of the atom fluorescence due to the cooling laser is reported. If the atoms are excited by the pulse-laser, they will not be detect the cooling laser and will therefore not fluoresce as the cooling lights are switched back on. As only a fraction of the atoms (mainly those in overlap with the cavity mode) in the ensemble are inverted due to the pulse-laser, a large background is seen in figure 29 a and in 29 b, as the used photomultiplier detects the fluorescence from the entire ensemble. A plot of the total number of excited atoms in the ensemble

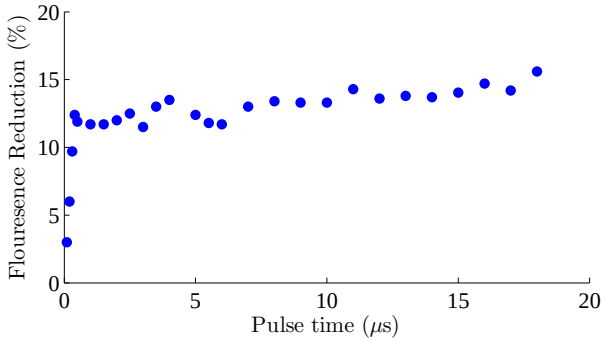

Figure 30: *Plot shows MOT fluorescence reduction normalized to an initial fluorescence level as a function of time in which the cooling lasers where switched off. About three Rabi floppings are expected to be seen, as the Rabi frequency* $\sim 3\,\mathrm{MHz}$ *whiles the decoherence cause by the Doppler swift has a frequency of* $\sim 1\,\mathrm{MHz}$*. As the atoms in the MOT have a average velocity of* $\sim 1\,\mathrm{m/s}$*, the atoms initially located in the intra-cavity fields anti-node, can move to a to the highly saturated node of the intra-cavity field in* $t = 689\,\mathrm{nm}/(1\,\mathrm{m/s}) = 170\,\mathrm{ns}$*. Thus no Rabi floppings are expected at a time larger than* $t = 170\,\mathrm{ns}$ *as the intra-cavity field will saturate the atoms.*

was found as a function of time and is seen in figure 30. A reduction of $\sim 10\%$ is seen, corresponding to an excitation percentages of 10 % of the total number of atoms in the MOT cloud.

By using the experimentally found excitation percentages value of 10 %, the total level of excited atoms within the intra-cavity mode is found. Therefore, the geometry of the overlap between the volume of the pulse-laser cylinder and the volume of the MOT sphere, which can be seen in figure 11, must be calculated. This is done with the assumption that the number of atoms (n) is constant. The fraction of fluorescent atoms are thus calculated:

$$10\% = \eta \frac{\pi 2 R r^2 n}{\frac{4}{3}\pi R^3 n}, \tag{54}$$

which reduces to:

$$10\% = \eta \frac{3}{2}\left(\frac{r}{R}\right)^2. \tag{55}$$

Here η is the fraction of excited emitters in the overlap, r is the minor axis radius of the ellipse and R is the radius of the MOT. Inserting the measure values $r = 0.85\,\mathrm{mm}$ and $R = 2.5\,\mathrm{mm}$ and solving for η reveals $\eta = 75\,\%$. But due to the finite temperature and the detuning limitations of equation (52), the maximum excitation level of the atoms interacting with the pulse-laser was calculated to 60 %. However, this calculation does not account for the presence of a continuous intra-cavity field. Neglecting the reduction originating from the presence of a continuous intra-cavity field, the total level of excited emitters into the cavity mode is estimated to $P_c = 0.60 \cdot 0.75 = 45\%$.

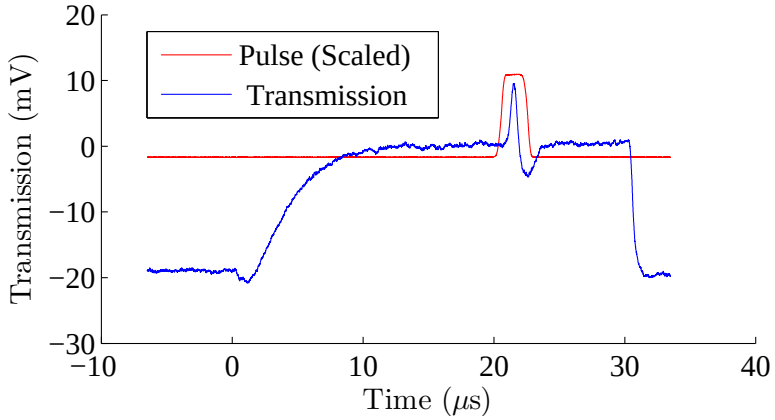

Figure 31: *Transmission signal obtained during the laser pulse sequence shown in figure 28 b). Four different features can be seen. Firstly, the transmission is increased when the cooling lights are turned off. Secondly, after* 20 μs *a pulse laser was turned on for the duration of* 2 μs*, interacting with the atoms and creating a flash. Thirdly, the pulse laser is switched off and a oscillations around the steady state are observed in the first few micro seconds after. Lastly, the cooling lights are switched back and the transmission returns to the original steady state*

Thus an upper bound on the total number of excited atoms emitting into the intra-cavity field is $N_a = N_{cav} \cdot P_c = 9 \times 10^6$ atoms. As $N_a > N_{threshold}$, collective emission in our experiment is possible.

Thus experimental features of our systems collective emission is investigated.

5.1.3.1 *Experimentally obtained features of collective emission*

The atoms in the cavity mode are prepared in excited state in accordance with section 5.1.3. The emission from the atom-cavity system is investigated and features of collective emission are now studied. For our experimental set-up visualized in 4.3, the time sequence of the different lasers is can be visualized in figure 28 a. The transmission field through the cavity mirror was observed during the sequence and is shown in figure 31.

In the detected emission from the atom-cavity system seen in figure 31, four different stages are observed. Firstly, the transmission is increased when the cooling lights are turned off, thus the AC Stark shift initially caused by intra-cavity field and the cooling lights is cancelled. With the AC-stark shift for the atoms cancelled, the absorption spectrum for the intra-cavity laser is also changed, leading to an increased transmission. After 10 μs a new steady state is reached. This time scale is also predicted by considering the inverse Rabi frequency ($\sim 1/100$ kHz) for the $^1S_0 \rightarrow {}^3P_1$ transition. Secondly, after 20 μs the pulse-laser was turned on for the duration of 2 μs. This effects the transmission spectrum by causing a sudden increase in intensity previously referred to as a flash. The flash has a delay of ~ 0.6 μs after

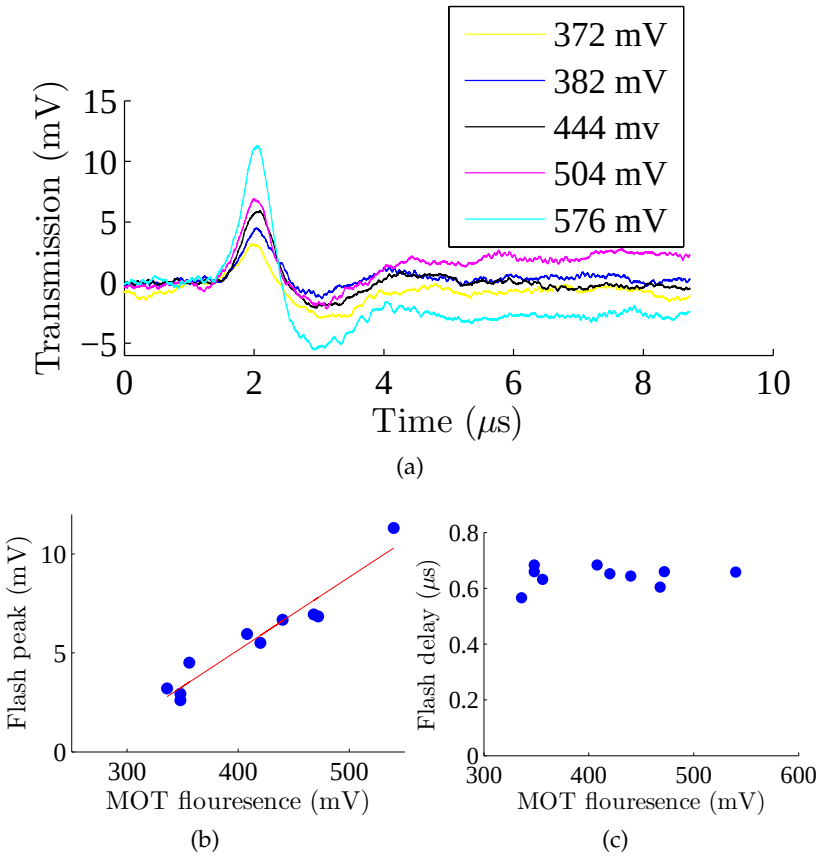

Figure 32: ***a)*** *Flash shape dependency on number of atoms. Here a high number of atoms is represented by a high MOT fluorescences.* ***b)****Flash shape peak height dependency on number of atoms. Blue circles represents experimentally obtained data. The red line is a* 1^{st} *degree polynomial fit. For the* 1^{st} *degree polynomial fit the threshold value (y=o) is found to be* 260 mV *and* $R^2 = 0.93$. ***c)*** *Flash peak delay dependency on number of atoms. Blue circles represents experimentally obtained data.*

the pulse-laser is initiated and has a duration of $\sim 1\,\mu s$. The flash delay time is an indication of a SF-like emission occurring. Furthermore the decay time of the observed flash is shorter than the decay time for the $^1S_0 \rightarrow {}^3P_1$ transition, furthermore indicating some sort of collective processes different from the natural decay of the $^3P_1$ state. Thirdly, after the initial flash oscillations around the new steady state are observed, in the first few microseconds following the flash. These oscillations will be investigated for coherent light later on in this section. Lastly, the cooling lights are switched back on and the atoms are once again subjected to a AC Stark shift, thus the cavity transmission returns to the original steady state.

The characteristic parameters dependencies for the collective emission described in section 5.1.1, were also investigated. In order to characterize the collective emission, the number of atoms, pulse-laser

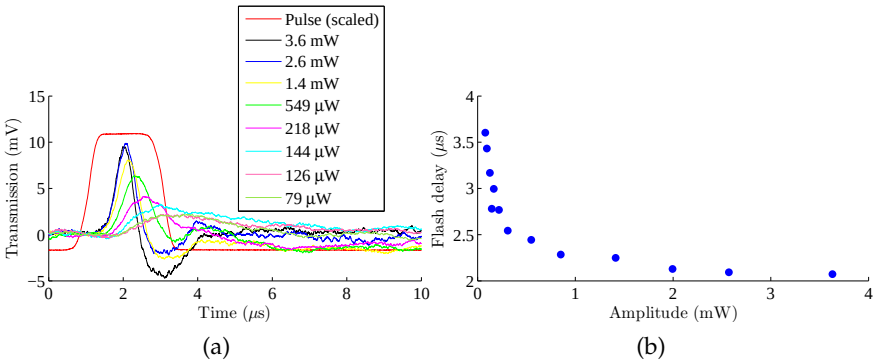

Figure 33: ***a)*** *The pulse power dependency of the flash peak delay. The pulse duration was set to* $2\,\mu s$ *in all cases.* ***b)*** *The pulse power dependency of the flash peak delay. The pulse duration was set to* $2\,\mu s$ *in all cases.*

power and intra-cavity power levels were varied. The lineshape of the flash as a function of number of atoms is seen in figure 32 a. The variation of the number of intra-cavity atoms are represented by the variation of the fluorescence level. The specific number of atoms is not relevant in this plot, as only tendencies are examined. By varying the MOT loading time, the number of atoms entering the MOT could be controlled, thus allowing for a change to the number of atoms in the cavity mode, that participate to the collective emission. The flash peaks show a linear dependency of N_{Cav}, as seen in figure 32 b. This stands in contrast to the case of pure SF, which predicts a flash peak behaviour proportional to N_{Cav}^2, as mentioned earlier. However, arguments were also made for a flash with SF properties but with a flash peak proportional to N_{Cav}, in specific parameter regimes. A linear fit was obtained and predicts a threshold atom number $N_{Cav} = 8.5 \times 10^6$ atoms, corresponding to a MOT fluorescences level of 260 mV. Below this threshold, no flash is expected to appear. This experimentally found threshold value lies above the theoretical predicted threshold value in equation (42) where $N_{threshold} = 2.3 \times 10^5$ atoms, for an average atomic temperature $T = 5\,mK$.

Another property of SF is the theoretically predicted delay time $\tau_D \propto \frac{1}{N_{Cav}}$. However as seen in figure 32 c, an increase in intra cavity atoms do not effect the flash delay. Rather, the flash delay seems to be constant at $\sim 600\,ns$. Thus there is no clear indication of the collective emission being SF or something else. Another interesting feature of the flash delay was found to be the inverse of the pulse power (P_{pulse}). This was not predicted as a parameter within [**15**]. However [**15**] does not includes an optical cavity in their system, which might account for the deviation. As seen in figure 33 b, the flash delay time dependency of the the power of the pulse-laser is given as $\tau_D \propto 1/P_{Pulse}$. As the pulse power is changed, so must the duration

of the pulse, in order to fulfil equation (53). However the pulse duration was kept at a constant 2 μs throughout all power variations. A possible explanation for the flash delay dependency on pulse power, can be thought of in terms of the excited atoms on a Bloch sphere. As equation (53) is not fulfilled, the Bloch vector of the different atoms do not reach as far towards the north pole as those who fulfil equation (53). Thus the atoms need a longer time to become phase-locked before a collective flash can be emitted.

A common feature for all the observed flashes is the coherent ringing, as seen in figure 33 a. The coherence is visualized by damped oscillation around the steady state transmission level. These oscillations appear after the flash and quickly vanish within a few μs. To determine if these oscillations are in fact coherent, the NICE-OHMS technique from section 4.2 is used. As described, the demodulated signal signal will result in a signal proportional to the collective phase induced on the atom-cavity transmission by the atomic ensemble. In order to obtain the demodulated signal, the cavity emission was measured simultaneously using a slow and a fast Avalanche Photodiode (APD), where the emission signal measured by the fast APD was demodulated using a local oscillator. The measured emission of the slow APD and the fast APD with a demodulation signal can be seen in figure 34. It is seen that the flash event appears in both the slow and fast APD, appearing as the direct transmission signal and as a deviation from the steady state of the demodulated signal. This indicates that some fraction of the emitted flash radiation is coherent. However, the emission features seen after the flash in figure 34 b, are not mirrored within the NICE-OHMS transmission signal seen in figure 34 a. This may indicate that another unknown process occurs due to the continuous driving of the atoms from the intra-cavity laser. In achieving this demodulated signal, the frequency of the intra cavity seed laser was shifted one FSR (781.14 MHz) away from resonance. This was done in order to keep the cavity stabilized, but without exposing the atoms to an intra-cavity field. The reason for this manoeuvre, was to investigate the flash dependency of the intra-cavity field. In order to do so, the now shifted intra-cavity probe laser was phase modulated, thus allowing a sideband to be resonant with the atoms. This set-up allows for the cavity to stay stabilized by the carrier frequency and at the same time probe the atoms using the sideband and was also described in section 4.2. By varying the phase modulation amplitude, the resonant sideband power amplitude was varied, as shown in figure 35 a. A linear dependency of the flash peak height and the sideband probe power amplitude is seen in figure 35 b. Thus indicating a critical amplitude for which a flash is present. Also, it can be seen that a flash without a intra-cavity field laser present is not achievable within this set-up. One explanation could be, that a critical level of excitation is not reached with a pulsed laser power of 3.8 μW. Therefore

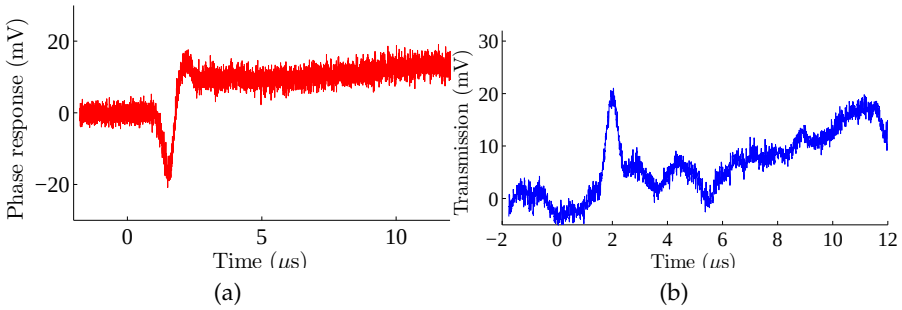

Figure 34: ***a)*** *The cavity transmitted flash measured by measuring the non-modulated transmission. Measurement was performed simultaneously with obtaining* ***b)****. The pulse length was* 20 μs *long and a quasi continuous signal can be seen to appear after the flash.* ***b)*** *The cavity transmitted flash measured by using the NICE-OHMS technique. Measurement was performed simultaneously with obtaining* ***a)****. The pulse length was* 20 μs *long and a quasi continuous signal can be seen to appear after the flash. Whiles the flash incident shown in* ***a)*** *is clearly visible in the form of coherent spike in this plot, it is unclear how to interpret the coherence signal after the initial spike.*

I build a new injection-locked laser capable of increasing the power level with nearly a factor 10, which was described in section 3.2.2.

In striving to achieve flashes without a intra-cavity laser preparing a fraction of the number of atoms, an alternative pulse-laser was inserted. This allowed for pulse-laser power of 19.7 μW and pulse durations of $\tau = 280\,ns$. After months of reproducing the above mentioned results with the injection-locked laser, a effort was made to obtain a flash without a intra-cavity laser present - without success. Determined to achieve a flash without an intra-cavity laser, other parameters in $C_N\Gamma \gg \Gamma_{decoh}$ were considered. In order to diminish the decoherence that the atoms could experience, several solutions were purposed. Not being able to cool the atoms temperature any further I turned to other sources of decoherence. Eventually making sure the atoms were not exposed to any leftover radiation from the cooling lasers, was investigated. Therefore a mechanical light shutter arm was inserted to cancel any remnant cooling light interfering with the atoms at the critical probing stage. Due to the mechanical nature of the shutter arm, the shut-time instability affiliated with synchronizing the shutter arm with the rest of the experimental sequence, was to large and was therefore not pursued any further. The details and results of the mechanical shutter are described in section 4.2.1.

If experimentally obtained flash is to be used as a source of stabilization, the spectral properties of the flash must be investigated further. As the spectral properties of a single flash can not be resolved due to Fourier-limitations, a multiple-flash set-up was proposed. A multi-flash set-up could possibly result in a quasi-continuous trans-

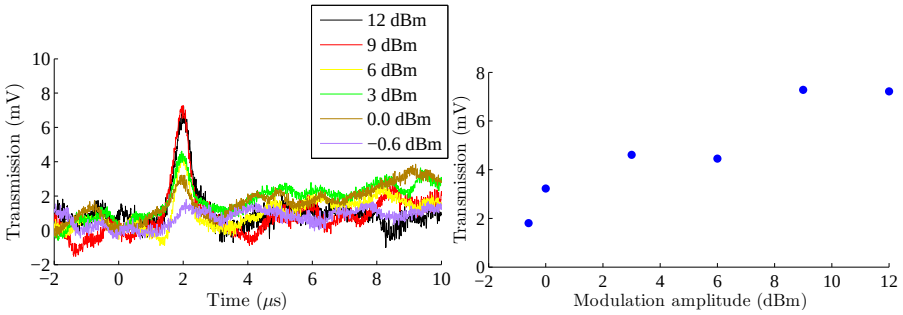

(a) (b)

Figure 35: ***a)*** *Flash shape for different intra cavity seed powers. The probe intra cavity seed frequency was shifted by one FSR, thus the atomic resonance was interrogated by the sideband. The seed power was controlled by adjusting the modulation amplitudes, which represents an amount of optical probe laser power transferred to the resonant sideband.* ***b)*** *Flash shape peak intensity for different intra cavity seed powers.*

mission signal, from which the spectral purity of the collective emission could be measured.

5.1.3.2 *Double pulse*

In order to realize the narrow linewidth of the collective emission for stabilization, a cyclic sequence of collective coherent emission is not sufficient. Instead a continues emission signal is needed. Limited by the experimental set-up of having a discrete atom loading time, this was not achievable within our system. Therefore, in order to investigate the spectral purity of the collective flash, a sequence with multiple flashes was pursued. However, preliminary measurements with two flashes were set up, in order to examine the optimal delay between initiating flashes for reproducing desired intensity level. The sequence of applied lasers to achieve this, is shown in figure 36. Ideally, this would prolong the time in which a flash(es) exist to the microsecond regime, thus undermining the possible Fourier limitation and simultaneously allowing a spectrometer to analyse the spectral properties. This experimental set-up further limits the expected results, in that a continues flow of new atoms are not available as is required when a coherent excitation is performed. This means that over a course of time, the spectral properties of the transmission light will be dominated be the linewidth of pulse-laser and not inherit the narrow linewidth property of the collective emission. Further limitations in our system set-up comes in the declining number of atoms available for probing, as the cooling laser are switched off. Due to technical limitations, the pulse-laser could only be turned on two times within one sequence. A series of measurements were obtained, varying the duration between the two pulse-lasers. The results can be seen in figure 37. A pulse-laser is turned on at $t = 0\,s$, followed by a second

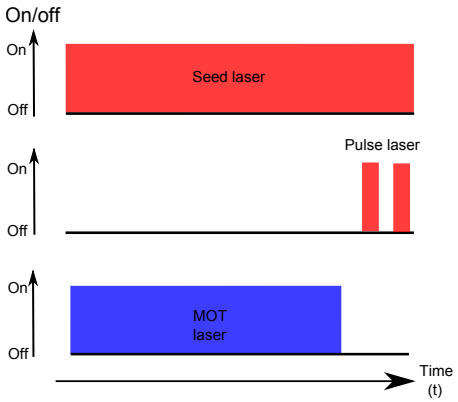

(a)

Figure 36: *Illustration of the sequence for the relevant lasers for investigating of collective emission of two flashes in this work. This sequence used for investigations of collective emission two flashes in this sub-section 5.1.3.2.*

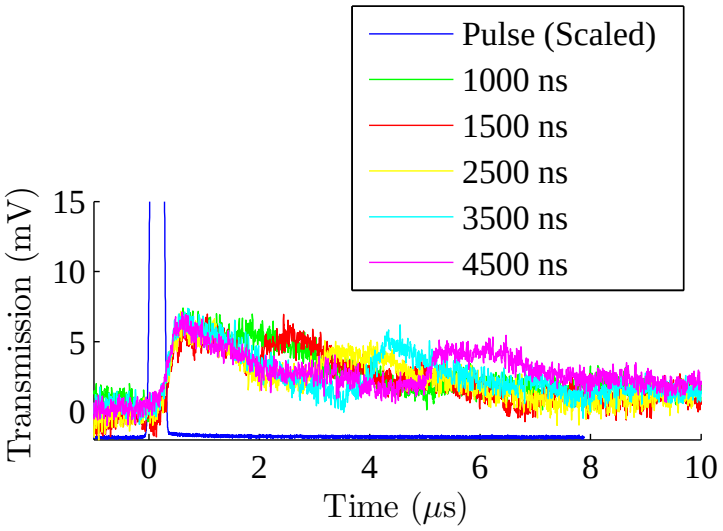

(a)

Figure 37: *Transmission signal following two pulsed-lasers with different intermediate time. A pulse-laser is turned on at* $t = 0\,s$ *(blue), followed by a second pulse-laser (not shown) a certain time after the initial laser. This sequence is done with a intermediating time from* $1\,\mu s$ *to* $4.5\,\mu s$.

pulse from the same pulse-laser, with a certain delay time after the initial pulse. This produces a initial flash originating from the first pulse and a secondary flash originating from the second pulse. It can be seen that the secondary flash roughly reaches the same level of intensity as the initial flash, at delay time of 1 μs to 1.5 μs. However, to correctly determine the hight of the secondary pulse-laser, a fit of the secondary flash is needed. This could reveal a constant secondary flash hight on top of a decaying initial flash. An effort was made to follow this line of thought however, these preliminary measurements were quickly determined too crude and were associated with to large fluctuations. In order to progress, new data must be obtained with data-points representing more averages. Due to lack of time, this is not incorporated into the dissertation but is left for future students.

5.2 CONCLUSION AND OUTLOOK

In this section, a theoretical outline of SR, SF and ASE was presented. Different characteristic time scales were presented an used to predict the behaviour and dependencies of a collective emission bursts. It was predicted from equation (42) that the threshold number of atoms needed for a collective emission flash, was $N_{thres} = 6.3 \times 10^5$ atoms. Using experimentally found values, it was also predicted that $T_2 > \sqrt{\tau_R \tau_D}$ would hold true and a SF flash could occur. In the SF regime, it was predicted that a flash height would scale as N^2 in the pure SF regime and as N for the non-pure SF regime. Furthermore the SF regime predicted that a flash delay would be present and that it would be proportional to $1/N$. Coherent oscillations succeeding the initial flash were also expected.

A numerical approach was also reported. The motivation for this was to incorporate features, such as an optical cavity and a seed laser, of the experimental system, that were not originally included into the theoretical predictions. Using the calculated equations of motion in equation (48)-(49), the system was set to simulate collective emission and hint indications of a coherence. The result can be seen in figure 27 a. Here a flash occurs with predicted power of 140 nW and a delay time of ~ 1 μs. In figure 27 b, atomic coherence is shown to evolve at roughly the same time as the flash occurs. This hints at some level of coherence occurring in the flash.

Lastly, an experimental investigation was reported. Using a atom-cavity with cooled ^{88}Sr system, $C_N \gg 1$ was achieved allowing for a strong collective coupling. This fulfilled the inequality $NC_0\Gamma \gg \Gamma_{decoh}$, allowing for collective emission phenomena to occur. Initially inverting the atomic population allowed for collective emission, as presented in figure 31. The threshold number of cavity atoms found experimentally was 8.5×10^6 atoms which far surpassed the theoretically predicted threshold number of atoms. The flash height scales as

N, indicating that pure SF is not obtained. Also, when converting the flash intensity from millivolt to nanowatt, the intensity of a flash differs with a factor of 4 from the simulated prediction. This is possibly due to the saturation effects that a fraction of the atoms experience due to the intra-cavity field. This is likely due to the numerical simulations lack of incorporating spontaneous decay into the intra-cavity field mode. A flash delay was observed at $\tau_D \simeq 0.6\,\mu s$ after the initial pulse-laser was applied. This closely correspond to the expected time predicted in the numerical approach. The height and delay of the flash did however not seem to depend on the number of atoms, as predicted be the initial SF theory. However, the SF theory given by [**17**] takes neither a continuous seed field nor an optical cavity into account. The coherent oscillations predicted by theory and seen in the numerical simulation results of figure 27 a, are also observed in our experiment as seen in figure 31 - however not as outspoken.

The observed flash can not be determine as pure SR, SF or ASE. However, many of the features of SF are present, indicating the most likely classification of the observed collective emission. To further understand the observed collective emission a theoretical descriptions, including a optical cavity and a seed laser, must be given. Furthermore the numerical simulation must be developed to allow for spontaneous emission into the cavity mode, to ignite the collective emission process. Likewise the fraction of saturation atoms in the intracavity field most be determined more carefully.

The double pulse-laser experiment, obtained two flashes of similar intensity when compared to one another. This method can be used to obtain further knowledge of spectral purity of the emission flash. However, these preliminary results in figure 37 are affiliated with large uncertainties. In order to progress, more detailed measurements and a sequence of multiple pulses are needed.

6 PROSPECTS

In the previous section a discussion of the results from our experimental realization of collective spontaneous emission was given. By using an experimental set-up which performed measurements in a cyclic manner, a SF-like burst was observed. However, if a laser is to utilize the mHz linewidth in achieving stability beyond the current state-of-the-art laser stabilization techniques, any limitation on the fractional locking time of the measurement cycle, corresponding to the relation τ/T_c of the Allan deviation of equation (2), will result in a limitation on the stability of the laser frequency. In a cyclic measurement set-up where a single measurement is realized once every $\sim 700\,\mathrm{ms}$, the stabilization using a mHz linewidth can not be realized, as any drift in the free-running periods cause a large variance within these time-scales.

A possible way to resolve the spectral purity of a mHz linewidth is to achieve a quasi-continuous detection signal of the millisecond time-scale, as shown in section 5.1.3.2. However, the laser linewidth used for coherent excitation of the 2-level atoms, would limit the achievable linewidth of any quasi-continuous detection signal in our system. Furthermore, the constant number of atoms required to be the same in each measurement, is not maintained over the millisecond time-scale.

A Strontium beamline experiment is currently being constructed in the Cold atoms group at the Nils Bohr Institute, that seeks a continuous interrogation time. Such a beamline experiment would utilize a two dimensional MOT, resulting in a continuous stream of new atoms entering the cavity. Furthermore the beamline experiment will use an incoherent 3-level excitation scheme in order to diminish any limitations on the achievable linewidth of the continuous detection signal.

By utilizing an active light source as a alternative to a passive reference cavity, this dissertation is part of a proof-of-principle approach towards new techniques in the development of ultra-stable laser sources.

Part I

APPENDIX

A

APPENDIX A

Københavns Universitet
Det Natur- og Biovidenskabelige Fakultet
Att. Amalie Windeløv Hansen
Sektion International og Kandidatoptag
Tagensvej 16
2200 København N.

Siemensfonden
(Siemens A/S Fond)

Ballerup, den 22. januar 2016

Ansøgning til Siemensfonden – nr. 8. Studerende Stefan Mossor Rathmann, Niels Bohr Instituttet.

Siemensfonden har på sit møde den 21. januar 2016 behandlet alle indkomne ansøgninger.

Det glæder mig at kunne meddele, at Siemensfonden har besluttet at imødekomme din ansøgning med kr. 31.108,00.

Af praktiske grunde vil jeg gerne anmode om, at fakultet fremsender kontonummer til bankoverførsel af dette beløb. Dette kan eventuelt gøres per mail til Michael Laub: michael.laub@siemens.com

På Siemensfondens vegne
Michael Laub

Siemens A/S
Siemensfonden
Sekretariat:
John Finnich Pedersen
Borupvang 9
DK-2750 Ballerup
Telefon: 44 77 44 77
Direkte: 44 77 45 70

APPENDIX B

B

Derivation of the Relative Intensity of the Light Emitted by a Previously MOTed Cloud

Martin Ravn

June 15, 2016

We assume that the spatial distribution of the atoms, at time $t = 0$, is Gaussian in each coordinate,

$$p(x_i = X_i \mid t = 0) = \frac{1}{\sigma_x\sqrt{2\pi}} e^{-\frac{1}{2}\left(\frac{X_i}{\sigma_x}\right)^2}$$

Furthermore we assume that the velocity of the atoms is Maxwell-Boltzmann distributed, i.e. Gaussian in each component

$$p(v_i = V_i) = \frac{1}{\sigma_v\sqrt{2\pi}} e^{-\frac{1}{2}\left(\frac{V_i}{\sigma_v}\right)^2}$$

where $\sigma_v = \sqrt{\frac{kT}{m}}$, with k being Boltzmanns constant, T the temperature of the MOT cloud and m the mass of an atom.

We first need to determine the spatial distribution at later times. First, as all distributions mentioned so far are independent, we can consider the spatial distributions along the axes independent of one another, hence we need only consider motion in one dimension.

Assuming total knowledge of an initial position x_0 and initial velocity v, we see that

$$p(x = X \mid x_0, v, t) = \delta(X - (x_0 + vt)) = \frac{1}{t}\delta\left(v - \frac{X - x_0}{t}\right)$$

Hence, by the laws of probability, what we seek is given by

$$\begin{aligned}
p(x = X \mid t) &= \int_{-\infty}^{\infty}\int_{-\infty}^{\infty} p(x = X \mid X_0, V, t)\, p(x_0 = X_0)\, p(v = V)\, dV dX_0 \\
&= \frac{1}{\sigma_x\sigma_v 2\pi}\int_{-\infty}^{\infty}\int_{-\infty}^{\infty} \frac{1}{t}\delta\left(V - \frac{X - X_0}{t}\right) e^{-\frac{1}{2}\left(\frac{X_0}{\sigma_x}\right)^2} e^{-\frac{1}{2}\left(\frac{V}{\sigma_v}\right)^2} dV dX_0 \\
&= \frac{1}{\sigma_x\sigma_v t 2\pi}\int_{-\infty}^{\infty} e^{-\frac{1}{2}\left(\frac{X_0}{\sigma_x}\right)^2} e^{-\frac{1}{2}\left(\frac{X - X_0}{\sigma_v t}\right)^2} dX_0 \\
&= \frac{1}{\sigma_x\sigma_v t 2\pi}\int_{-\infty}^{\infty} e^{-\frac{1}{2}\left(\left(\frac{X_0}{\sigma_x}\right)^2 + \left(\frac{X - X_0}{\sigma_v t}\right)^2\right)} dX_0
\end{aligned}$$

By performing a larger amount of algebra on the exponent, we get

$$\begin{aligned}\left(\frac{X_0}{\sigma_x}\right)^2+\left(\frac{X-X_0}{\sigma_v t}\right)^2 &= \frac{X_0^2}{\sigma_x^2}+\frac{X^2+X_0^2-2XX_0}{(\sigma_v t)^2}=\frac{1}{(\sigma_v t)^2}\left(X^2+\left(1+\frac{(\sigma_v t)^2}{\sigma_x^2}\right)X_0^2-2XX_0\right)\\ &= \frac{1}{(\sigma_v t)^2}\left(X^2+\frac{1}{\sigma_x^2}\left(\sigma_x^2+(\sigma_v t)^2\right)X_0^2-2XX_0\right)\\ &= \frac{1}{(\sigma_v t)^2}\left(\left(1-\frac{\sigma_x^2}{\sigma_x^2+(\sigma_v t)^2}\right)X^2+\left(\frac{\sqrt{\sigma_x^2+(\sigma_v t)^2}}{\sigma_x}X_0-\frac{\sigma_x}{\sqrt{\sigma_x^2+(\sigma_v t)^2}}X\right)^2\right)\\ &= \frac{X^2}{\sigma_x^2+(\sigma_v t)^2}+\left(\frac{\sqrt{\sigma_x^2+(\sigma_v t)^2}}{\sigma_x\sigma_v t}X_0-\frac{\sigma_x}{\sigma_v t\sqrt{\sigma_x^2+(\sigma_v t)^2}}X\right)^2\end{aligned}$$

so

$$\begin{aligned}p(x=X\mid t) &= \frac{1}{\sigma_x\sigma_v t\sqrt{2\pi}}e^{-\frac{1}{2}\frac{X^2}{\sigma_x^2+(\sigma_v t)^2}}\int_{-\infty}^{\infty}\frac{1}{\sqrt{2\pi}}e^{-\frac{1}{2}\left(\frac{\sqrt{\sigma_x^2+(\sigma_v t)^2}}{\sigma_x\sigma_v t}X_0\right)^2}dX_0\\ &= \frac{1}{\sigma_x\sigma_v t\sqrt{2\pi}}e^{-\frac{1}{2}\frac{X^2}{\sigma_x^2+(\sigma_v t)^2}}\frac{\sigma_x\sigma_v t}{\sqrt{\sigma_x^2+(\sigma_v t)^2}}=\frac{1}{\sqrt{\sigma_x^2+(\sigma_v t)^2}\sqrt{2\pi}}e^{-\frac{1}{2}\frac{X^2}{\sigma_x^2+(\sigma_v t)^2}}\\ &= \frac{1}{\sigma(t)\sqrt{2\pi}}e^{-\frac{1}{2}\left(\frac{x}{\sigma(t)}\right)^2}\end{aligned}$$

where $\sigma(t)=\sqrt{\sigma_x^2+(\sigma_v t)^2}$(a Gaussian distribution was recognized for the integral). The spatial distribution thus continues to be Gaussian, but with a time-dependent standard deviation.

The lasers each have a gaussian intensity profile, of the form

$$I(x_1,x_2)=I_0e^{-\frac{1}{2}\frac{x_1^2+x_2^2}{\sigma_I^2}}$$

where I_0 is the peak intensity and σ_I is the standard deviation of the profile.

The three beams are orthogonal, so the total intensity is simply the sum of three of the above profiles along the three coordinate axes,

$$I_{total}(x_1,x_2,x_3)=I(x_1,x_2)+I(x_1,x_3)+I(x_2,x_3)$$

So the expected intensity, as a function of time, is (using symmetry at first)

$$\begin{aligned}\langle I(t)\rangle &= \int_{-\infty}^{\infty}\int_{-\infty}^{\infty}\int_{-\infty}^{\infty}I_{total}(X_1,X_2,X_3)\,p(x_1=X_1)\,p(x_2=X_2)\,p(x_3=X_3)\,dX_1dX_2dX_3\\ &= 3\int_{-\infty}^{\infty}\int_{-\infty}^{\infty}\int_{-\infty}^{\infty}I(X_1,X_2)\,p(x_1=X_1)\,p(x_2=X_2)\,p(x_3=X_3)\,dX_1dX_2dX_3\\ &= 3\int_{-\infty}^{\infty}\int_{-\infty}^{\infty}I(X_1,X_2)\,p(x_1=X_1)\,p(x_2=X_2)\,dX_1dX_2\\ &= \frac{3I_0}{\sigma(t)^2}\int_{-\infty}^{\infty}\int_{-\infty}^{\infty}\frac{1}{2\pi}e^{-\frac{1}{2}\frac{X_1^2+X_2^2}{\sigma_I^2}}e^{-\frac{1}{2}\left(\frac{X_1}{\sigma(t)}\right)^2}e^{-\frac{1}{2}\left(\frac{X_2}{\sigma(t)}\right)^2}dX_1dX_2\\ &= \frac{3I_0}{\sigma(t)^2}\left(\int_{-\infty}^{\infty}\frac{1}{\sqrt{2\pi}}e^{-\frac{1}{2}X^2\left(\frac{1}{\sigma_I^2}+\frac{1}{\sigma(t)^2}\right)}dX\right)^2=\frac{3I_0}{\sigma(t)^2}\left(\frac{\sigma_I\sigma(t)}{\sqrt{\sigma_I^2+\sigma(t)^2}}\right)^2\\ &= \frac{3I_0\sigma_I^2}{\sigma_I^2+\sigma(t)^2}=\frac{3I_0\sigma_I^2}{\sigma_I^2+\sigma_x^2+(\sigma_v t)^2}\end{aligned}$$

So the expected relative intensity is given by

$$\langle I(t)/I(0)\rangle = \frac{\sigma_I^2+\sigma_x^2}{\sigma_I^2+\sigma_x^2+(\sigma_v t)^2} = \frac{1}{1+\left(\frac{\sigma_v}{\sqrt{\sigma_I^2+\sigma_x^2}}t\right)^2} = \frac{1}{1+(at)^2}$$

Note that the shape of the curve only depends on the one parameter $a = \frac{\sigma_v}{\sqrt{\sigma_I^2+\sigma_x^2}}$. This is a shame as far as fitting goes, since it is then only possible to fit reliably to this parameter, making it impossible to determine several constants from a fit. To see this, note that holding holding a constant gives the equation

$$\sigma_I^2+\sigma_x^2 = \frac{1}{a^2}\sigma_v^2$$

which is the equation of a cone in the σ_I-σ_x-σ_v parameter space. There are therefore several different $(\sigma_I, \sigma_x, \sigma_v)$-tuples that gives the same shape.

If it is possible to determine σ_I, σ_x and a, however, the temperature is given by

$$T = \frac{m}{k}a^2\left(\sigma_I^2+\sigma_x^2\right)$$

C

APPENDIX C

NIELS BOHR INSTITUTE
UNIVERSITY OF COPENHAGEN

ECAMP12, Frankfurt, Germany, September 2016

Towards an Ultra-Narrow Linewith Laser Using Cold Strontium

M.H. Appel, S.M. Rathman, S.A. Schäffer,
B.T.R. Christensen, M.R. Henriksen and J.W. Thomsen

Niels Bohr Institute, University of Copenhagen, Blegdamsvej 17, 2100 Copenhagen, Denmark

Martin Hayhurst Appel
rdf414@alumni.ku.dk

Stefan Mossor Rathman
hzs110@alumni.ku.dk

Stefan Alaric Schäffer
schaffer@nbi.dk

Overview

Motivation:
Ultra stable frequency references such as the ones used in optical atomic clocks and for quantum metrology may be obtained by stabilizing a laser to an empty optical cavity. Such systems are currently limited by the thermal fluctuations in the cavity elements [1]. Here we present an active approach to ultrastable lasers; using a narrow atomic transition in a cold ^{88}Sr gas directly as a lasing transition. We enhance collective effects using a low finesse cavity in order to obtain superfluorescence (SF) in the system. This enhances the intensity of the laser while simultaneously causing a spectral narrowing of the emitted light [2]. Such a superfluorescent laser could improve laser stability beyond the state of the art.

Our work:
- Observation of superfluorescent-like behaviour in a finite-velocity ^{88}Sr gas at 5 mK.
- Theoretical simulations of the system agree well with experimental results.
- Preliminary results of quasi-continuous operation.
- Development of fully continuous systems under way.

General concept

The bad cavity regime
- $\Gamma << \kappa$. Atomic transition dominates spectral properties.

Superfluorescence
- 3π-pulse* excites atoms. Coupling via cavity field, atoms decay faster than Γ, creating a short burst.
- Resonant seed light stimulates the decay.
- Collective effects [2] important if $C_N\Gamma >> \Gamma_{decoherence}$ · $C_N = N \cdot C_0$, $\Gamma_{decoherence} \approx \Gamma_{doppler}$.

* A 3π-pulse is used for technical reasons.

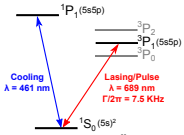

Fig. 1: Relevant level structure of ^{88}Sr showing the cooling transition and the lasing/pulse transition on which the SF-like burst occurs.

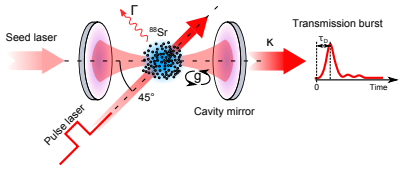

Fig. 2: Experimental setup for active lasing. ^{88}Sr atoms are trapped in a magneto optical trap (MOT) and cooled to T = 5 mK. Atoms may couple via the resonant cavity field enhancing collective effects. A seed laser tuned to the $^1S_0 \rightarrow {}^3P_1$ transition is constantly present and a second laser provides a pulse from the side, causing an atomic inversion and a subsequent burst after τ_D.

Superfluorescence-like burst

Principal experimental parameters
- Cavity finesse: F = 1500.
- Cavity linewidth: $\kappa/2\pi$ = 520 kHz.
- Atom number: N ≈ 2 ·10^7.
- Single atom cooperativity: $C_0 = \frac{4g^2}{\kappa\Gamma} = 5.5 \cdot 10^{-4}$.
- Temperature of atoms: T = 5 mK.
- Doppler broadening: $\Gamma_{Doppler}/2\pi$ = 1.1 MHz.

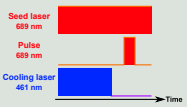

Fig. 3: Experimental procedure for measuring a flash showing the activation of the different lasers.

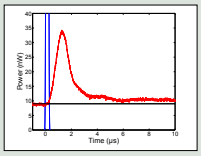

Fig. 4: Cavity transmission (red) showing a burst occurring τ_D = 1.2 μs after a 3π-pulse (blue) has been applied. The burst has a lifetime of ~ 1 μs which is much shorter than the natural atomic lifetime 1/Γ = 21 μs. Although the signal is averaged over 128 data series, ringing effects are visible. The non-zero start value is due to the seed field (black line) present in the cavity.

Single SF-burst
- Short burst, coherent ringing: SF-like behaviour [3].
- Good agreement with theoretical model (compare Fig.4 and Fig.6).
- $C_N\Gamma/\Gamma_{decoherence} \approx 75$. Theory suggests SF regime.
- No burst observed for zero seed field. (Similar experiments [4,5] report bursts for zero seed field).
- Possible unknown source of decoherence.

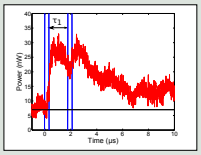

Fig. 5: Preliminary measurements of cavity transmission (red) showing two bursts. After the first pulse a second 3π-pulse was applied with a delay of τ_1= 1.7 μs, resulting in a second burst of similar intensity.

Quasi-continuous operation
- Preliminary results.
- Spectral properties may be measured from multiple, overlapping bursts.
- Theoretical [2] ultimate linewidth: $\Gamma_{min} = C_0\Gamma$.

Theoretical model and simulation

Theoretical model
- Jaynes Cummings Hamiltonian, N atoms, classical seed laser, pi-pulse:

$$\hat{H} = \hbar\omega_b\hat{a}^\dagger\hat{a} + \frac{1}{2}\hbar\omega_a\sum_{i=1}^{N}\hat{\sigma}_z^{(i)} + \sum_{i=1}^{N}\hbar g^{(i)}(\hat{a}^\dagger\hat{\sigma}_-^{(i)} + \hat{a}\hat{\sigma}_+^{(i)}) + \hat{H}_{seed} + \hat{H}_\pi$$

- Coupling strength $g^{(i)}$ depends on the i'th atom's position and velocity.
- Master equation:

$$\dot{\hat{\rho}} = \frac{-i}{\hbar}[\hat{H}, \hat{\rho}] + \mathcal{L}_\Gamma[\hat{\rho}] + \mathcal{L}_\kappa[\hat{\rho}]$$

Spontaneous emission; Cavity dissipation

- Optical Bloch equations found from $\dot{O} = \mathrm{Tr}\{\hat{O}\dot{\hat{\rho}}\}$.
- Approximate $\langle a\sigma_z^{(i)}\rangle \rightarrow \langle a\rangle\langle\sigma_z^{(i)}\rangle$ (neglects spontaneous emission into cavity mode).

Numerical methods
- Numerical integration of Bloch equations.
- 5·10^4 atom-groups are simulated.
- Constant Maxwell Boltzman distributed velocities.
- Spatial dimensions of cavity mode, 3π-pulse and atom cloud included.

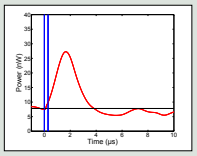

Fig. 6: Simulation of a transmission signal showing a burst (red) following a 3π-pulse (blue). The burst has a lifetime ~ 1 μs, much shorter than the natural atomic lifetime 1/Γ = 21 μs. Coherent ringing characteristic of superfluorescence is visible after t = 4 μs. The initial value of the transmission is non-zero due to the seed field (black line).

Prospects

Beamline experiment: Fully continuous SF laser.

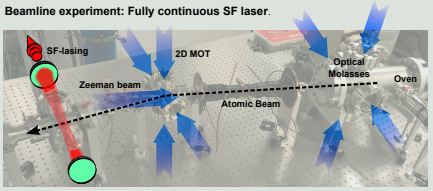

Fig. 7: Beamline experiment schematic. ^{88}Sr atoms are slowed with a Zeeman slower, cooled in a 2D MOT and deflected into the cavity region (red). The atoms undergo an excitation scheme while travelling to the cavity ensuring a continuous beam of excited atoms traversing the cavity mode. Increased cooperativity in the cavity allows for collective decay into the cavity mode, resulting in a superfluorescent lasing.

References

[1] G. D. Cole et al., *Tenfold Reduction of Brownian Noise in High-reflectivity Optical Coatings*, 2013 Nat. Phot. **7** 644.
[2] D. Meiser et al., *Prospects for a Millihertz-Linewidth Laser*, 2009 Phys. Rev. Lett. **102** 163601.
[3] M. Gross and S. Haroche, *Superradiance: The Theory of Collective Spontaneous Emission*, Physics Reports 93, No. 5 (1992) 301-396.
[4] A. Kumarakrishnan and X. L. Han, *Superfluorescence from optically trapped calcium atoms*, Phys. Rev. A, **58**:4153–4162.
[5] M. A. Norcia and J. K. Thompson, *Cold-Strontium Laser in the Superradiant Crossover Regime*, Phys. Rev. X **6**, 011025.

The authors would like to acknowledge support from the Danish Research Counsil and ESA Contract No. 4000108303/13/NL/PA-NPI272-2012.

BIBLIOGRAPHY

[1] Fritz, riehle: "Frequency standards - Basics and Applications", WILEY-VCH Verlag GmbH and Co. KGaA, 2004.

[2] Bureau International des Poids et Measures (2014). Bipm annual report on time activities. http://www.bipm.org/utils/en/pdf/time_ann_rep/Time_annual_report_2014.pdf. [Accessed March 30th 2016]

[3] Ushijima, I., Takamoto, M., Das, M., Ohkubo, T., and Katori, H. (2015). Cryogenic optical lattice clocks. Nature Photonics, 9(3):185–189.

[4] Thermal Noise Limit in Frequency Stabilization of Lasers with Rigid Cavities Kenji Numata, Amy Kemery, and Jordan Camp Laboratory for High Energy Astrophysics, Code 663, NASA/-Goddard Space Flight Center, Greenbelt, Maryland 20771 (Dated: October 9, 2004)

[5] Kessler, T., Hagemann, C., Grebing, C., Legero, T., Sterr, U., Riehle, F., Martin, M. J., Chen, L., and Ye, J. (2012a). A sub- 40-mhz-linewidth laser based on a silicon single-crystal optical cavity. Nature Photonics, 6(10):687–692.

[6] Meiser, D., Ye, J., Carlson, D. R., and Holland, M. J. (2009). Prospects for a millihertz-linewidth laser. Phys. Rev. Lett., 102:163601.

[7] Stefan Alaric Schaffer: Studies of Collective Effects In Atomic Strontium, M.Sc. thesis. Ultra cooled atoms, Niels Bohr institut, University of Copenhagen, 2015.

[8] Bjarke Takashi Røjle Christensen: Laser stabilization with laser cooled Strontium, PhD. thesis. Ultra cooled atoms, Niels Bohr institut, University of Copenhagen, 2016.

[9] Kuppens, S. J. M., van Exter, M. P., and Woerdman, J. P. (1994). Quantum-limited linewidth of a bad-cavity laser. Phys. Rev. Lett., 72:3815–3818.

[10] Christopher J. Foot: Atomic physics. Oxford master series in Atomic, Optical and Laser physics. Oxford university press (2005).

[11] Lecture notes on cooling techniques. Classical molasses and beam slowing. Page 3. Center for Ultracooled Atom, Michigan institute of Technology.

http://cua.mit.edu/8.422_S07/Notes%20on%20classical%20molasses%20and%20beam%20slowing.pdf

[12] H.J. Metcalf and P.van der Straten: Laser cooling and Trapping. Springer, 1999.

[13] L.M. Mortensen, M.R. Christiansen, C.R. Anker, and C.S. Brandstrup: Measuring the Temperature of ^{88}Sr Atoms Caught in a Magneto-Optical Trap. Ultra cooled atoms, Niels Bohr institut, University of Copenhagen, 2016.

[14] Dicke, R. H. Coherence in spontaneous radiation processes. Phys. Rev., 93:99–110. (1954).

[15] Bonifacio, R. and Lugiato, L. A. (1975). Cooperative radiation processes in two-level systems: Superfluorescence. Phys. Rev. A, 11:1507–1521.

[16] Superfluorescence from optically trapped calcium atoms. A. Kumarakrishnan. Department of Physics, New York University, New York, New York 10003 X. L. Han. Department of Physics, Butler University, Indianapolis, Indiana 46208 Received 27 January 1998!. PHYSICAL REVIEW A VOLUME 58, NUMBER 5 NOVEMBER 1998.

[17] Kumarakrishnan, A. and Han, X. L.: Superfluorescence from optically trapped calcium atoms. Phys. Rev. A, 58:4153–4162. (1998).

[18] Schuurmans, M.: Superfluorescence and amplified spontaneous emission in an inhomogeneously broadened medium. Optics Communications, 34(2):185 – 189. (1980)

[19] Martin H. Appel: Superradiance in a Strontium Cavity System: A Semi Classical Numerical Approach. Ultra cooled atoms, Niels Bohr institut, University of Copenhagen, 2016.

[20] M.R.Henriksen: Cavity Enhanced Spectrosocpy on Ultra Cold Atoms. M.Sc. Thesis: Niels Bohr Insitute, University of Copenhagen, 2014.

DECLARATION

Authors declaration.

Copenhagen, 14 October 2016

Stefan Mossor Rathmann